ANALYSIS OF TRIASSIC VOLCANIC ROCKS IN TWO PENDANTS, EASTERN SIERRA NEVADA, CALIFORNIA WITH IMPLICATIONS FOR CONTINENTAL ARC PALEOGEOGRAPHY AND VOLCANOLOGY

By Kelsey E. Brennan

A Thesis
Submitted in Partial Fulfillment
of the Requirements for the Degree of
Master of Science
in Geology

Northern Arizona University
December 2022

Approved:
Nancy R. Riggs, Ph.D., Chair
Andrew P. Barth, Ph.D.
Michael H. Ort, Ph.D.

ABSTRACT

ANALYSIS OF TRIASSIC VOLCANIC ROCKS IN TWO PENDANTS, EASTERN SIERRA NEVADA, CALIFORNIA WITH IMPLICATIONS FOR CONTINENTAL ARC PALEOGEOGRAPHY AND VOLCANOLOGY

KELSEY E. BRENNAN

The continental passive margin along the west coast of Laurentia transitioned from transpressional faulting to a subduction zone and continental magmatic arc in Pennsylvanian to Permian time, but the exact timing of initial arc magmatism, eruptive styles and sequences, and the depositional setting remain poorly understood. Several pendants in the Sierra Nevada in California preserve the transition from passive margin to active magmatic arc in early Triassic time. Mapping and facies analysis, whole-rock and zircon trace element geochemical data, and three new zircon U-Pb ages from pyroclastic rocks in the Ritter Range and Mount Morrison pendants provide insight into the timing and style of the initial stages of Triassic arc development at ~37°N.

A series of tuffs in the Agnew Meadows area in the Ritter Range pendant are poorly sorted deposits of juvenile and accidental lithic clasts and broken quartz and feldspar phenocrysts in a fine-grained groundmass and were emplaced by pyroclastic density currents. A pumice conglomerate unit within this sequence is composed of elongate pumice clasts in a volcanic ash matrix and is the result of the effusive emplacement of a subaqueous silicic dome in the Agnew Meadows area. Compositionally similar rocks crop out along strike in the Mount Morrison

pendant to the southeast; lithic clast and phenocryst sizes increase southward and the tuff of Skelton Lake becomes more chaotic in the farthest southeast corner of the pendant. The Red and White Spur area in the southwest corner of the Mount Morrison pendant exposes a thick unit containing caldera-wall megabreccia in fine-grained tuff of Skelton Lake. The tuff of San Joaquin Mountain in the Ritter Range pendant, the tuff of Skelton Lake at Skelton Lake, and the lithic-rich facies in the Red and White Spur area are compositionally similar, suggestive of cogenesis.

Previous studies of zircon in pyroclastic rocks in the Mount Morrison, Saddlebag Lake, and Ritter Range pendants yielded crystallization ages of 232 to 217 ± 2 Ma, which marks the earliest arc volcanism in this area. To determine eruptive sequences and constrain the relation between similar pyroclastic units across these pendants, new zircon U-Pb samples were collected and analyzed from two pyroclastic units in the Ritter Range and one in the Mount Morrison pendant. All three samples revealed identical ages within error centered at ca 220 ± 2 Ma, suggesting these units are coeval. Textural, stratigraphic, and whole-rock and zircon geochemical data collectively suggest these units are also cogenetic. Zircon geochemical signatures indicate contamination by continental crust in a convergent-margin setting.

Primary volcanic textures suggest subaqueous silicic dome carapace pumice and pyroclastic deposits in the Ritter Range pendant, and thick (>1 km) intra-caldera and caldera-wall breccia in the Mount Morrison pendant, indicating a caldera with a diameter of at least 13 km centered in the southeastern portion of this pendant. The earliest volcanic activity related to the Late

Triassic arc involved large silicic systems of calderas and domes, which likely erupted subaqueously, producing vesicular pumiceous clasts that floated in the water column before settling into pyroclastic material from coeval eruptions. Studies of these volcanic sections provide insight into juvenile volcanic arc evolution, paleogeography, and volcanism in an induced-subduction initiation setting.

TABLE OF CONTENTS

LIST OF TABLES

LIST OF FIGURES

1. INTRODUCTION

The eastern Sierra Nevada in California (Fig. 1) hosts Paleozoic-Mesozoic pendants that record the development of the Sierran arc as it was building on the western margin of Laurentia. Extrusive igneous units within these pendants are recognized as the surface manifestation of the first major episode of Sierran arc magmatism at this latitude and overlie Paleozoic passive-margin sediments and rocks related to the Antler Orogeny (Schweickert and Lahren, 1999; Bateman, 1992; Barth et al., 2011; 2012; 2018). Volcanism in early Triassic time included eruption of a series of ignimbrites deposited in a marine setting, possibly from subaqueous calderas (Fiske and Tobisch, 1978, 1994; Schweickert and Lahren, 1999; Barth et al., 2018). Within the Ritter Range pendant, beds of limestone, carbonate-cemented tuffs, and calc-silicate rocks lend support to the hypothesis that the early stages of arc construction were in a subaqueous environment (Fiske and Tobisch, 1978; Barth et al., 2018). Preliminary geochronology, geochemistry, and mapping presented by Barth et al. (2018) and Field (2018), and continued in this study, focus on units in the Agnew Meadows region of the Ritter Range pendant, and the Skelton Lake and Red and White Spur areas of the Mount Morrison pendant. These studies demonstrate the presence of several ignimbrite units and a cryptic unit that contains elongate pumice clasts in a dark matrix. Units in the nearby pendants (Saddlebag Lake and Mount Morrison) are similar in age, geochemistry, and mineralogy to units in the Agnew Meadows area (Barth et al., 2018; Field, 2018), leading to the suggestion that these units from separate pendants are cogenetic. Though ages, geochemistry, and preliminary textural data have been gathered, the eruptive sequence of volcanic units in Agnew Meadows has not been established. Determining the eruption style and sequence of these units and the relation to similar rocks in the Mount Morrison pendant provide an opportunity to determine the volcanic source and the paleography of this area. Studies of these volcanic sections are important to understanding juvenile volcanic arc evolution, paleogeography, and volcanism in the Triassic Sierran arc.

This study tests the hypothesis that the volcanic facies of Agnew Meadows (Figs. 1, 2) record the deposition of subaqueous rhyolitic eruptive products during Late Triassic time. Early-arc paleogeography and volcanic setting were determined using geologic mapping and detailed volcanic facies analysis of the Agnew Meadows region and geochemical and geochronological data from Agnew Meadows and Red and White Spur (Figs. 1 and 3). A key unit in the Agnew Meadows succession is a “pumice conglomerate,” a clast-supported conglomerate characterized by light-colored, rounded blocks 5-30 cm long in a dark, aphanitic matrix. Interpreting the conglomerate’s characteristics and composition, especially in relation to nearby units, is instrumental in confirming the sequence of eruptive activity, relation to other pendant facies and location of a source caldera and testing the hypothesis of a subaqueous depositional environment at the time. Facies analysis was conducted, and samples collected from several units within Agnew Meadows (Fig. 2) and the area near Red and White Spur (Fig. 3). Zircon ages, textures, and mineralogy from Field (2018) and Barth et al. (2018) indicate an ignimbrite unit (tuff of Agnew Meadows) in this area is similar in stratigraphic placement, age, and texture to the tuff of Skelton Lake near its namesake in the Mount Morrison pendant. Field (2018) interpreted the tuff section near Red and White Spur to be caldera-margin deposits. The comparison of petrographic and geochemical data between the Agnew Meadows area and the

Red and White Spur area are used to interpret each area in the context of the caldera, investigating both location and how it erupted. This investigation provides important clues about the Triassic paleogeography of the volcanic arc rocks now exposed at ~37.5°N.

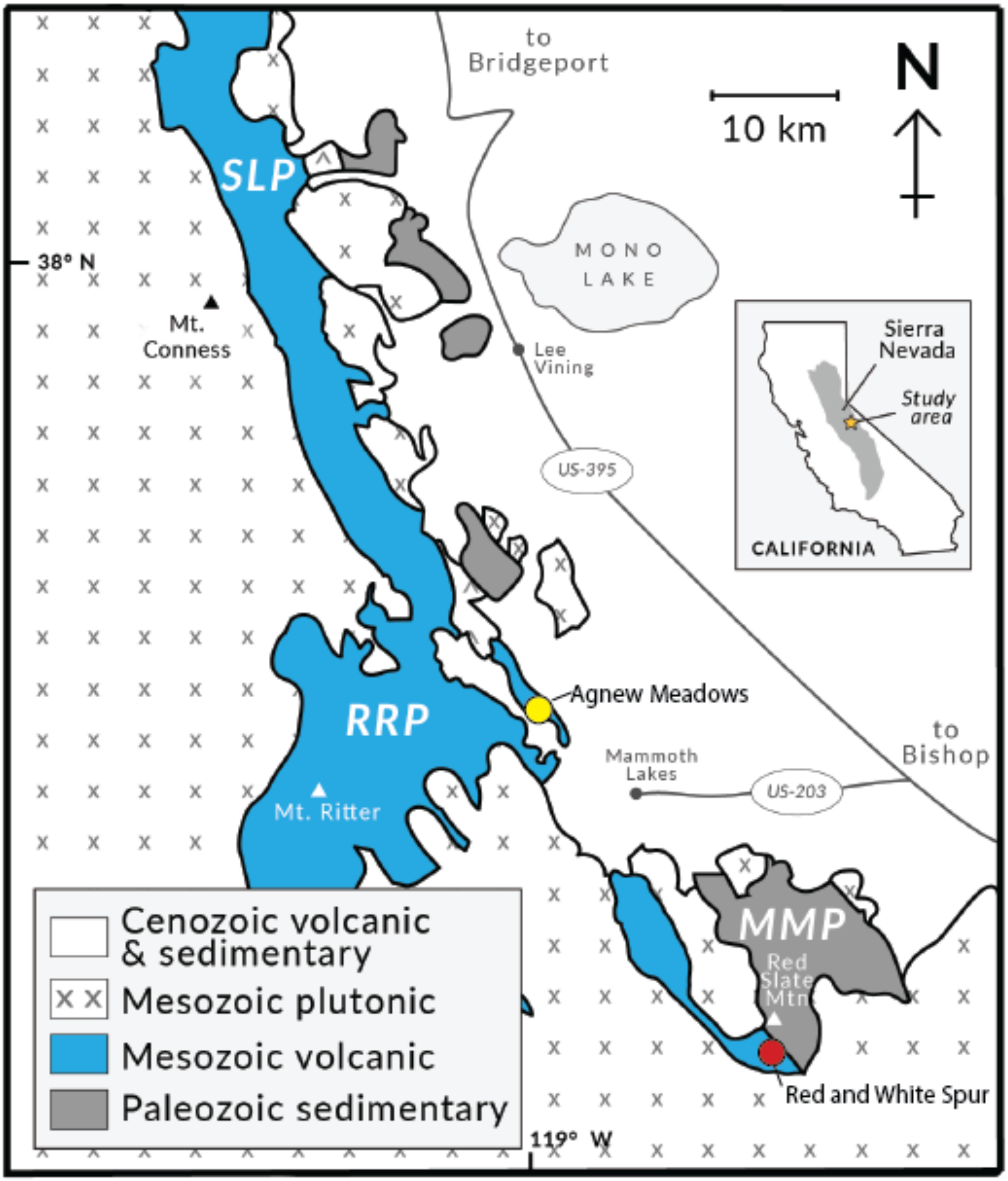

Figure 1: Map of the eastern Sierra Nevada modified from Field (2018) showing major rock types and ages in the Ritter Range (RRP), Mount Morrison (MMP), and Saddlebag Lake pendant (SLP). The two locations visited in this study are indicated by the circles labeled Agnew Meadows and Red and White Spur.

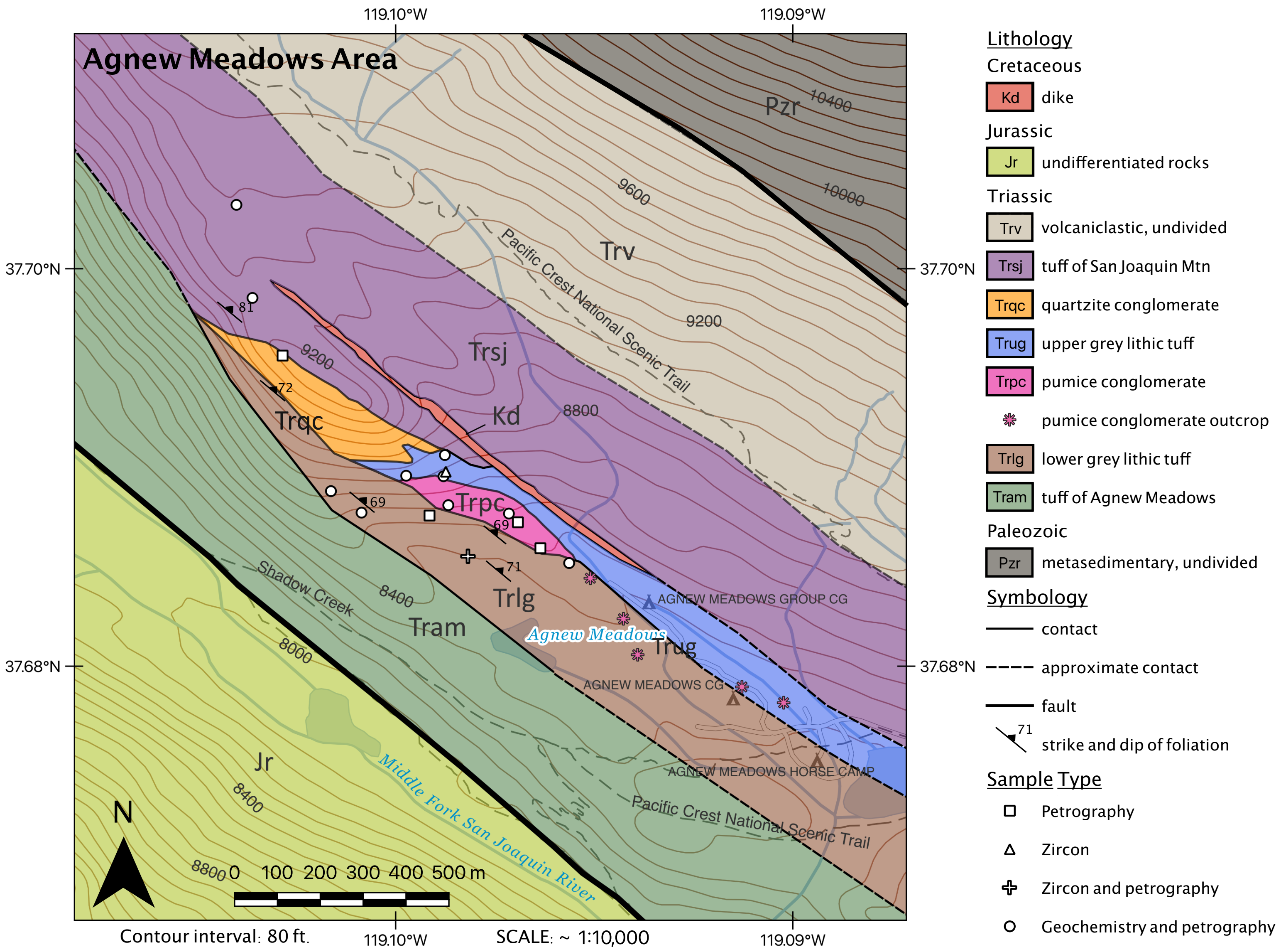

Figure 2: Geologic map of the Agnew Meadows area in the Ritter Range pendant, eastern Sierra Nevada.

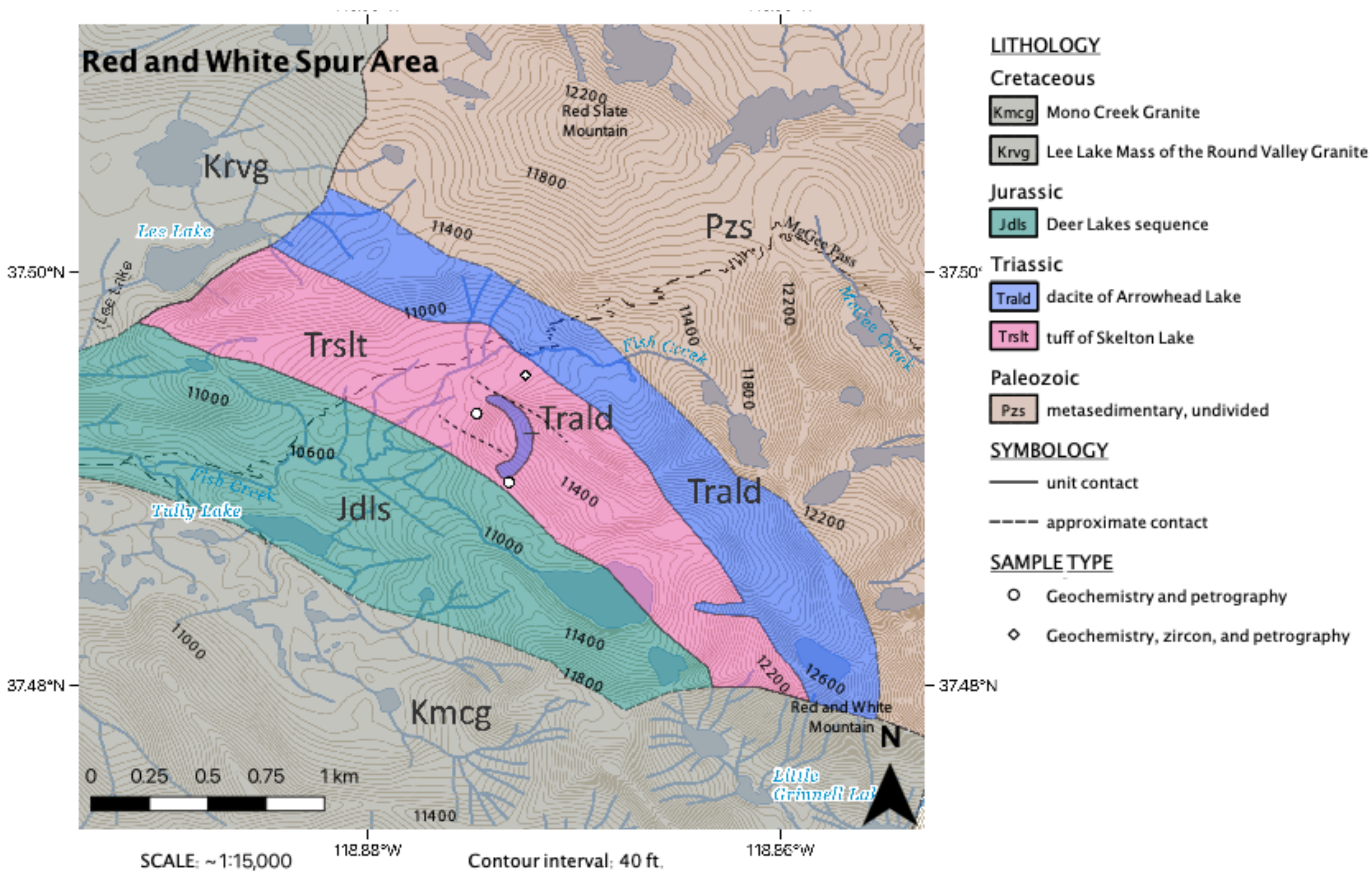

Figure 3: Geologic map of the Red and White Spur Area in the Mount Morrison Pendant. Dashed lines between sample points differentiate facies of the tuff of Skelton Lake in this area.

2. BACKGROUND

2.1 PRE-ARC GEOLOGIC HISTORY

Neoproterozoic rifting initially created the western margin of Laurentia and, by ca. 560 Ma, a southwest-trending continental shelf was established (Stevens et al., 1997). The passive margin gradually subsided, resulting in sedimentation through Late Devonian time (Stevens et al., 1997). During the Devonian Antler Orogeny, the Roberts Mountain allochthon was thrust onto the Laurentian margin (Morgan and Rankin, 1972), and the Golconda allochthon was emplaced during a subsequent thrust event in the Permian-Triassic Sonoma orogeny, resulting in an unconformity (Russel and Nokleberg, 1977; Saleeby, 2011). The southwest-trending passive margin was truncated in late Paleozoic time by the California-Coahuila fault, which caused a shift to an oblique convergent boundary and initiated a new subduction zone (Dickinson, 1977; Walker, 1988; Saleeby, 2011). This transition from a passive to convergent margin is recorded in the roof pendants (Ritter Range, Mount Morrison, and Saddlebag Lake) of the eastern Sierra Nevada as an unconformity dividing Paleozoic shelf, slope, deep-sea, and mafic volcanic rocks from Mesozoic arc volcanic rocks (Figure 1; Nokleberg and Kistler, 1980; Schweickert and Lahren, 2006; Cao et al., 2015). These pendants are separated in modern geography by the Mesozoic Sierra Nevada Batholith (Schweickert and Cowan, 1975; Nokleberg and Kistler, 1980; Barth et al., 2012, 2018). As the plate boundary shifted, transpressive fold-and-thrust deformation occurred on a regional scale, as well as the early stages of arc plutonism and the gradual thickening of the overriding plate, which increased buoyancy and caused regional uplift (Stevens and Stone, 1988, 2005; Saleeby and Dunne, 2015; Levy et al., 2021). The arc magma evolved as it was emplaced into thicker and more geochemically evolved continental crust (Barth et al., 2013). The initial magmas produced by subduction were sourced from depleted and/or enriched mantle and intruded and incorporated continental basement. The inception of this arc and its evolution are recorded in both plutonic and volcanic rocks in the Sierra Nevada in California and indicate that volcanism began no later than ca. 235 Ma at ~37.5° N (Barth et al., 2018).

Structural, stratigraphic, and geochronological studies indicate that the majority of Mesozoic arc volcanism along the plate boundary occurred over three separate time periods of high-volume magmatism (pulses), separated by two lulls, time periods of significantly lower eruptive volume (Fiske and Tobisch, 1978, 1994; Sorenson, 1998; Schweickert and Lahren, 2006; de Silva et al., 2015; Barth et al., 2018). The first phase began in the Early Triassic period with volcanic activity that resulted in submarine deposition of crystal-rich dacitic and rhyolitic volcanic material in the Mount Morrison, Ritter Range, and Saddlebag Lake pendants at approximately 232 to 217 Ma (Barth et al., 2018). Thick volcanic successions are present in all three pendants and indicate that Late Triassic volcanism was voluminous in the east-central Sierra Nevada and peaked at ca. 220-210 Ma. Geochronological evidence and trace element geochemistry indicate Late Triassic plutonism and volcanism are coeval and likely cogenetic, making the pendants and early batholith rocks compositionally and chronologically related (Barth et al., 2012). Late Triassic and Late Jurassic/Early Cretaceous shortening and tilting marked the second phase of the boundary’s Mesozoic volcanic history (Ducea, 2001; Barth et al., 2018). This second high-flux pulse overlapped with Cordillera-wide transgression, which caused marine rocks to be emplaced in the Sierra Nevada (Fiske and Tobisch, 1978; Sorensen et al., 1998; Barth et al., 2018). Subsequent subaerial volcanic activity and deposition in Cretaceous time marked the third and final phase (Ducea, 2001; Jones and Rougvie, 2004; Barth et al., 2018). Pluton input also peaked during this time, resulting in hornfels- to greenschist-grade contact metamorphism of the earlier volcanic rocks (Hanson et al., 1993; Sorensen et al., 1998; Barth et al., 2018). Geochronology and geochemical similarities between pendant volcanic deposits and plutons help establish an arc tempo with magma fluxes marking specific stages of arc formation. Thus, ages and geochemical characteristics of volcanic material constrain timing of arc inception and the evolution of a long-lived volcanic arc (Barth et al., 2018).

2.2 LATE TRIASSIC PENDANTS

Three pendants are exposed on the eastern side of the present-day Sierra Nevada crest: Mount Morrison, Ritter Range, and Saddlebag Lake (Fig. 1). These three pendants contain units relevant to understanding the transition from Paleozoic passive margin to an active magmatic arc overlying a subduction zone.

2.2.1 Ritter Range Pendant - Agnew Meadows Area

The Ritter Range pendant (Fig. 1) is the largest of the Mesozoic eastern Sierra Nevada pendants, consisting of a volcanic-rock sequence approximately 15 km thick that ranges in age from Triassic to Cretaceous, making it the most continuous record of arc volcanism from that time (Fiske and Tobisch, 1978; Schweickert and Lahren, 2006). The lower section makes up the majority of the pendant and is composed of an ~11-km-thick sequence of metamorphosed Late

Triassic ignimbrites, fallout tuffs, lava flows, breccias, hypabyssal intrusions, and limestone lenses (Fiske and Tobisch, 1978). This entire sequence was emplaced in a marine setting of low topographic relief, inferred from the presence of pelecypod *Weyla* and ammonite fossils in limestone interbeds in many locations and hyaloclastic textures in others (Rinehart and Ross, 1964; Fiske and Tobisch, 1978).

The basal succession in the Ritter Range pendant contains two Late Triassic large-volume ignimbrites, with many smaller ignimbrite units <1 to 350 m in thickness (Fiske and Tobisch, 1978; Sorensen et al., 1998). One of the oldest units, the tuff of Agnew Meadows (220 ± 2 Ma) represents some of the earliest volcanic activity of the Sierran arc in this pendant (Barth et al., 2015; 2018). The increased strength of welding to the southeast within the Mount Morrison pendant volcanic rocks implies a source vent in that direction (Rinehart and Ross, 1964). The tuffs in the Agnew Meadows area in the Ritter Range pendant are deformed and weakly regionally metamorphosed, but primary igneous textures are often well preserved, including subhedral quartz phenocrysts exhibiting deep embayments (Tobisch et al., 1977; Barth et al., 2018). Strain markers in these units suggest average elongations of 30-50% perpendicular to foliation, and all units experienced metamorphism in albite epidote hornfels to hornblende hornfels facies (Tobisch et al., 1977; Hanson et al., 1993). Whole-rock geochemical data from tuff samples from the basal section of Ritter Range pendant show the tuffs are arc-type, phenocryst-rich dacites and rhyolites based on abundances of fluid-mobile high-field-strength elements (Barth et al., 2018). These samples are generally enriched in the most incompatible trace elements (Barth et al., 2018). Zircon from the Triassic sections of these pendants exhibits trace element patterns in agreement with those expected for convergent-margin settings: high Sc/Yb relative to U/Yb (Barth et al., 2018).

2.2.2 Mount Morrison Pendant – Skelton Lake Area and Red and White Spur Area

The Mount Morrison pendant lies to the southeast of the Ritter Range pendant, and Triassic rocks account for more than half of the volcanic material in this pendant (Fig. 1, 3). The Skelton assemblage is the major Mesozoic volcanic sequence in this pendant (Fig. 1, 3; Rinehart and Ross, 1964; Barth et al., 2018; Field, 2018). According to Jones and Rougvie (2004), the Skelton assemblage was emplaced in a shoreline-marine depositional environment, with evidence for subaqueous emplacement conditions including deposits of juvenile rhyolitic lava in a pelagic mud matrix (Rinehart and Ross, 1964). Field (2018) determined the tuff of Skelton Lake is at least 13 km long and has a maximum thickness of 1.2 km in the northern section of the pendant.

Red and White Mountain lies in the southernmost spur of the Mount Morrison pendant (Fig. 4). The area includes outcrops of the tightly folded Paleozoic continental-margin sedimentary rocks unconformably overlain by Late Triassic volcanic rocks (Rinehart and Ross, 1964). The Late Triassic section contains the Arrowhead Lake dacite suite and the pendant's dominant ignimbrite, the tuff of Skelton Lake (216.5 ± 1 Ma) (Field, 2018; Barth et al., 2018). This ~300-m-thick section of the tuff of Skelton Lake is lithic rich and commonly intruded by the Arrowhead Lake dacite (Field, 2018). These rocks near Red and White Mountain lie along strike and share many characteristics with the volcanic sequences in the eastern Ritter Range and Saddlebag Lake pendants, leading Huber and Rinehart (1965) to tentatively correlate the stratigraphic sections despite the connection being obscured by the Neogene Mammoth Mountain volcanic complex. Field (2018) carried out an initial investigation of Triassic volcanic rocks near Red and White Mountain, and these preliminary results suggested that the volcanic rock sequence is similar to the tuff of Skelton Lake to the north, and the abundance of lithic fragments and size of particles decreases from south to north.

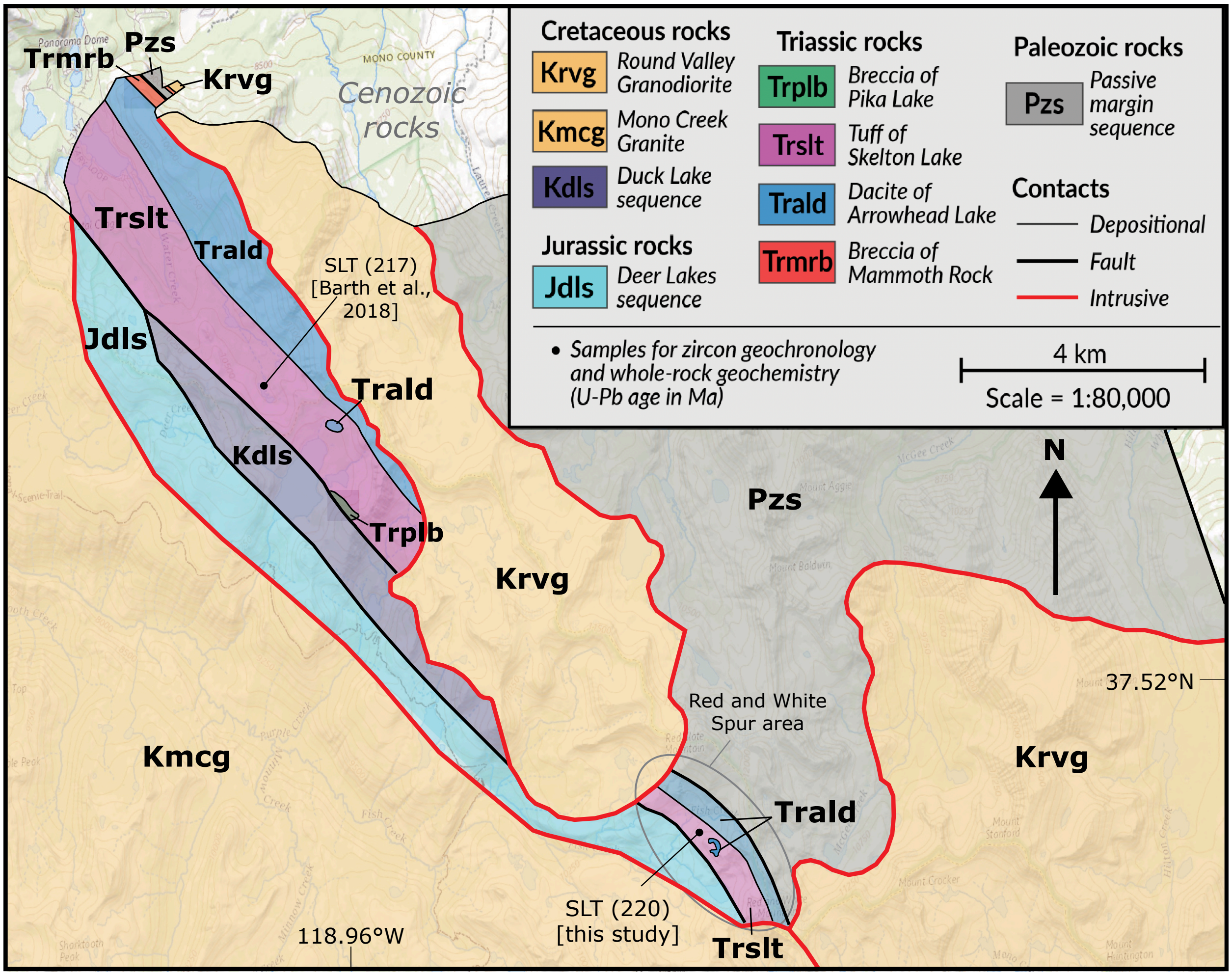

Figure 4: Geologic map of the Mount Morrison pendant (modified from Field, 2018). SLT denotes the two sampling locations of the tuff of Skelton Lake with zircon U-Pb ages in Ma shown in parentheses. The Red and White Spur area is shown in detail in Figure 3.

2.3 CALDERA FACIES

Determining the location of caldera structures and deposits is complicated in the Triassic volcanic rocks of the Ritter Range and Mount Morrison pendants by both the separation of the pendants and the complex erosion and deformation of the rocks. Facies analysis of ignimbrites and surrounding units provides information about the proximity to a source caldera. Lipman (1984) recognized key caldera features that can be recognized even in older, deformed areas, including the identification of intra- and extra-caldera ignimbrites. The main characteristics involved in separating these ignimbrite facies of calderas are relative thickness, phenocryst and clast sizes and types, and textures indicative of significant welding. Ignimbrite thickness is greatest within the caldera collapse area, with thickness outside the collapsed area thinning with increasing distance (Curtis, 1968; Druitt and Sparks, 1984; Walker, 1984; Heiken et al., 1990; Cole et al., 2005). Prior to caldera collapse, the entire area is blanketed in ignimbrite, but during and after the main collapse, thick sequences of ignimbrites are emplaced inside the now-lower-elevation caldera (Williams, 1941; Smith, 1979; Walker, 1984; Heiken et al., 1990; Cole et al., 2005; Sruoga et al., 2013). Intra-caldera facies are commonly the most strongly welded and thickest ignimbrites (100 m to > 1 km), and roof blocks are preserved in many cases (Bailey et al., 1976; Heiken et al., 1990; Cole et al., 2005; Sruoga et al., 2013). Breccia derived from the physical margins of the caldera itself, where the walls of the caldera collapse inward and the breccia from the wall rock is mixed with and preserved in thick sequences of syn-eruptive ignimbrites, provides the best evidence for the location of the caldera margin (Lipman, 1984; Sruoga et al., 2013). Field (2018) suggested that the breccia facies of the tuff of Skelton Lake at Red and White Mountain represents a caldera-margin breccia, providing further evidence that the caldera is within the southeastern section of the Mount Morrison pendant.

2.4 SUBAQUEOUS RHYOLITIC VOLCANISM

Subaqueous rhyolitic eruptions can be effusive, explosive, or a hybrid of the two (Fiske and Matsuda, 1964; Downey and Lentz, 2006). The eruption type is largely dictated by the amount of water overlying the vent itself, but also by the initial volatile content of the magma. The increased pressure from water (as compared to air) allows for later, more abrupt exsolution of volatiles as the magma approaches the sea floor, allowing magma with high volatile content to erupt either explosively or effusively at great water depths (Stix, 1991). The explosive eruptions result in plumes and deposits similar to those in subaerial eruptions: jet-driven eruptions create hot, clast-filled plumes that carry fine material up and away from the vent, and the denser material either falls out or is carried as subaqueous pyroclastic density currents (PDCs) (Fiske and Matsuda, 1964). These PDCs travel like subaerial PDCs, but often show signs of fast cooling and lack fine material due to elutriation (Fiske and Matsuda, 1964; Stix, 1991; Cas and Giordano, 2014).

Subaqueous effusive eruptions are possible at all water depths, and these effusive eruptions can occur as lava flows and dome growth but can also occur by the quench detachment of highly vesicular magma as it approaches the top of the conduit (Downey and Lentz, 2006; Rotella et al., 2013). The vesicular pieces are quenched on the margins while the interior continues to vesiculate, creating equant and large interior vesicles. Clasts from the subaqueous Kermadec arc (Barker et al., 2012; Rotella et al., 2013; Mitchell et al., 2019; Murch et al., 2020) show a bimodal density distribution, with low-density clasts having a foamy appearance, while high-density clasts are sub-angular and blocky with stretched vesicles. The disintegration of pumice is delayed due to insulating steam sheaths and thick bubble walls that prevent early pore-pressure-driven disintegration (Kokelaar, 1986). Due to decreasing hydrostatic pressure, pumice clasts continue to internally vesiculate as they rise through the water column, forming interior textures of homogenous, >90% vesicularity and exterior rims of stretched vesicles (Rotella et al., 2013). When water finally enters through cooling joints and inflation cracks, the clasts disintegrate, and water saturation eventually causes them to sink. These eruptions create pumice clasts that can be deposited either close to their parent dome/lava or far from their vent. This eruptive style reflects intermediate eruption rates with magma vesicular enough to be buoyant upon reaching the top of the conduit and facilitates clast dispersal over significant distances (~25 km from caldera rim) as recorded at Macauley volcano (Rotella et al., 2013).

3. METHODS

This study involved mapping at ~1:12,000 scale, stratigraphy and facies analysis, petrography, whole-rock and zircon geochemistry, and zircon U-Pb geochronology. Field work was completed during August of 2021 and laboratory work followed in the fall of 2021 and spring of 2022. The objective was to provide a detailed description of Triassic volcanic rocks to compare them to units in the Mount Morrison pendant to the south, including the tuff of Skelton Lake and volcanic rocks in the Red and White Spur area near Red and White Mountain (Figs. 5, 6, 7; Table 1). Facies analysis, petrography, geochemical characteristics, and zircon geochronology allow an interpretation of the Triassic paleogeography of the early Sierra Nevadan volcanic arc.

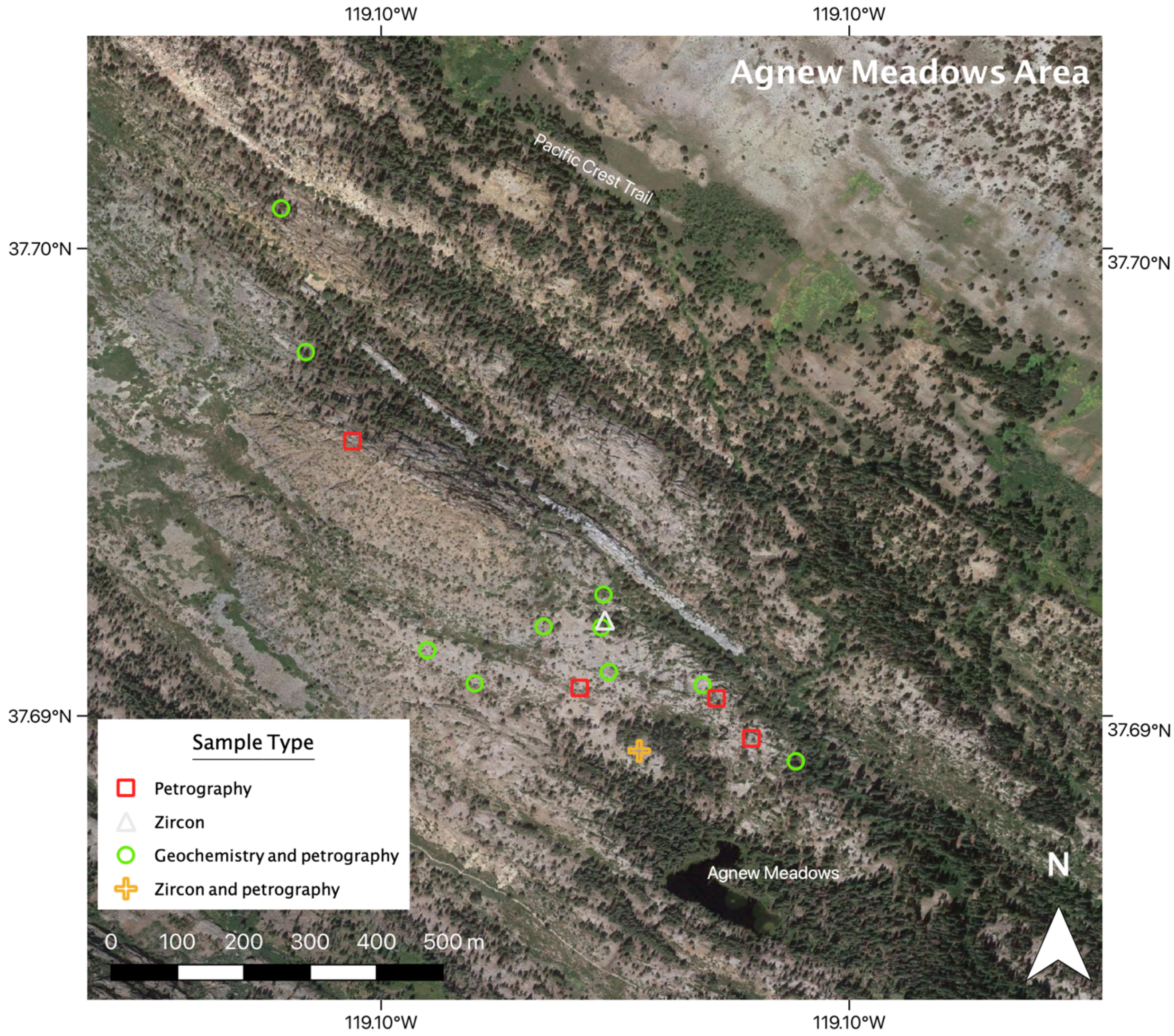

Figure 5: Sample locations in Agnew Meadows Area in the Ritter Range Pendant. Location coordinates and sample numbers are provided in Table 1.

Figure 6: Sample location (green circle) for the tuff of Skelton Lake near Skelton Lake in the Mount Morrison pendant. Two samples were collected at this location: the tuff of Skelton Lake and a dark mafic clast in the tuff. Both samples were analyzed for whole-rock geochemistry and petrography. Location coordinates and sample numbers are provided in Table 1.

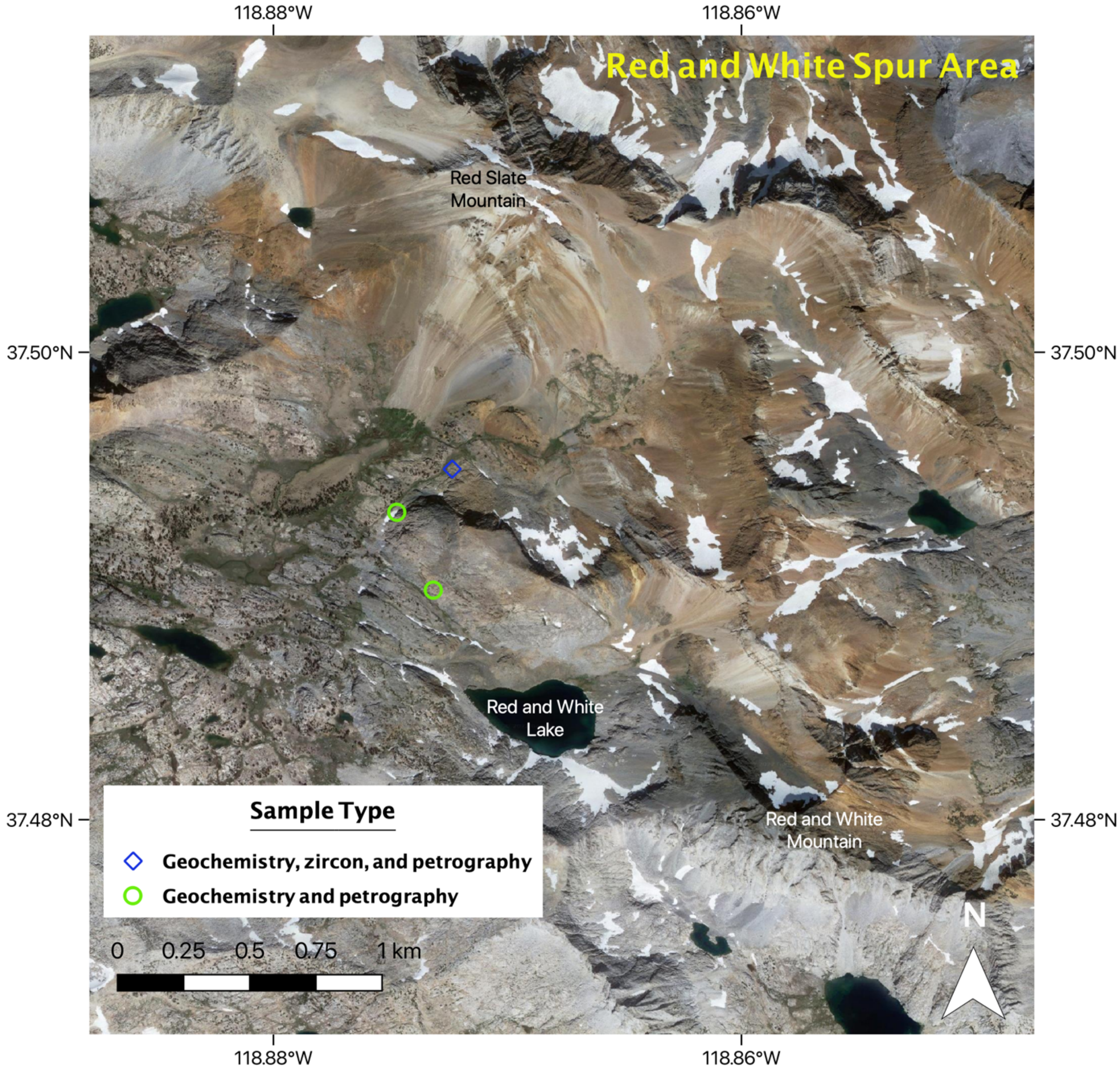

Figure 7: Sample locations in the Red and White Spur area in the Mount Morrison pendant. Two samples (green circles) were collected for whole-rock geochemistry and petrography, and one sample (blue diamond) was collected for whole-rock geochemical, zircon, and petrographic analyses. Location coordinates and sample numbers are provided in Table 1.

Bulk-rock samples were collected for zircon geochronology and geochemistry from two volcanic units in the Agnew Meadows area in the Ritter Range pendant and one sample from a volcanic unit in the Red and White Spur area in the Mount Morrison pendant (Figs. 5, 7; Table A).

Preparation for geochronology analysis, including rock crushing, mineral separation, and zircon grain extraction, was completed using standard methods (Gehrels, 2000) at Northern Arizona University. Zircon samples were analyzed for U-Pb geochronology and trace element geochemistry using laser ablation-inductively coupled plasma-mass spectrometry at the laser ablation split-stream laboratory at the University of California, Santa Barbara Petrochronology Lab in 2021. This laboratory utilizes a Nu Plasma high-resolution multi-collector-inductively coupled plasma-mass spectrometer (HR MC-ICP-MS) and a Nu AttoM single-collector ICP-MS (Nu Instruments Ltd, Wrexham, UK) as well as an Analyte 193 excimer ArF laser-ablation system with a HeLex sample cell (Photon Machines, San Diego, California) using a 24-µm beam. U-Pb age analyses were normalized against primary reference standards GJ-1 (ca 600 Ma; Jackson et al., 2004) and 91500 (ca 1062.4 Ma; (Wiedenbeck et al., 2004), with secondary standard Plešovice (337.13 Ma; Sláma et al., 2008). Trace element analyses were normalized against Mali, 91500 (Wiedenbeck et al., 2004), and NIST612 reference standards, and all results agree within 1-2% error of the standard ages or values. Data were reduced using Iolite 4 software in Igor Pro 9, and error was assessed according to Kylander-Clark et al. (2013). All age uncertainties are 2σ. Discordance for grains of Phanerozoic age was evaluated on U-Pb ages by comparing ^{206}Pb/^{238}U and ^{207}Pb/^{235}U for individual zircon grains, and grains > 10% normally discordant or > 5% reversely discordant were not used in interpretations and are indicated by “discordant” in the data table. For each sample, the weighted mean age of the youngest population of zircon grains with the mean square weighted deviate (MSWD) value closest to 1 was taken as the best estimate of crystallization age (cf Lodes et al., 2020; Dobbs et al., 2021). MSWD plots, Tera-Wasserburg concordia, and Wetherill concordia diagrams were created using the IsoPlotR Graphical User Interface (GUI) created by Vermeesch (2018). The TuffZirc analysis in IsoPlot (Ludwig, 2003), an analysis that determines an age based on an assumption of cogenesis of crystals, was compared to the IsoPlotR results. Zircon geochemical data obtained include Pb, Fe, Si, P, Ca, U, Th, Zr, Ti, V, Y, Nb, La, Ce, Pr, Nd, Sm, Eu, Gd, Tb, Dy, Ho, Er, Tm, Yb, Lu, Hf, and Ta. Zircon trace element and U-Pb geochemical data are available in Appendix B.

Whole-rock geochemical analysis was performed to obtain information on major element geochemistry for 12 samples from the Agnew Meadows area, one sample from the Skelton Lake area, and three from the Red and White Mountain Spur (Figs. 5, 6, 7; Table A). Bulk-rock samples were cut down to 30 gm pieces at Northern Arizona University and sent to Michigan State University, where the samples were crushed in steel and tungsten carbide jaw crushers and ground in a tungsten carbide mixer mill. Fused glass disks were analyzed using X-ray fluorescence (XRF) with a Bruker S4 PIONEER 4 kW wavelength dispersive X-ray fluorescence spectrometer (WDXRF) for major element oxides. A duplicate analysis of one sample was performed for standardization, and reference standards BHVO, RGM-2, and Jb-1a were used. The following major element oxides were measured: SiO_2, TiO_2, AlO_2, Fe_2O_3, MnO, MgO, CaO, Na_2O, K_2O, and P_2O_5. Whole-rock major element data are provided in Appendix C. Data reduction was performed using Bruker's SPECTRAplus software using fundamental parameters. For XRF analysis, precision is better than 1% for most major elements. Whole-rock trace element analysis was not performed on these samples due to laboratory issues.

SAMPLE INFORMATION			ANALYSES		
Rock Unit	Sample ID	Latitude, Longitude	Whole-rock Geochemistry	Zircon U-Pb and Geochemistry	Petrography
AGNEW MEADOWS AREA					
Lower grey tuff	KB 080521-1	37.688554, -119.102402	x		x
Lower grey tuff	KB 081221-2	37.689529, -119.101222		x	x
Lower grey tuff	KB 080521-3	37.688477, -119.100605			x
Lower grey tuff	KB 080721-1A	37.689122, -119.103211	x		
Clast in Lower grey tuff	KB-080721-1B	37.689122, -119.103211			x
Grey tuff SE of pumice conglomerate	KB 080821-1	37.687222, -119.096912			x
Grey tuff SE of pumice conglomerate	KB 080821-2	37.687222, -119.096912	x		x
Lithic tuff NW of pumice conglomerate	KB 081221-1	37.687400-119.099588	x		x
Pumice conglomerate	KB 080821-3	37.687614, -119.097672			x
Pumice conglomerate	KB 080521-2B	37.688751, -119.100107			x
Matrix of pumice conglomerate	KB 080521-2A	37.688751, -119.100107	x		x
Pumice conglomerate clast	KB 080921-2	37.688529, -119.098505	x		x
Pumice clast with inclusion	KB 080921-1	37.688300, -119.098268			x
Upper grey tuff	KB 081121-1	37.689636, -119.100174		x	
Upper grey tuff	KB 080321-1	37.690075, -119.100199	x		x
Upper grey tuff	KB 080921-3	37.689515, -119.100235	x		x
Tuff of San Joaquin Mtn	KB 081021-1	37.696687, -119.105710	x		x
"Lithic tuff" from Barth (pers. comm., 2021)	KB 081021-2	37.694228, -119.105286	x		x
Clastic unit N of Agnew Meadows	KB 081021-3	37.692704, -119.104490			x
SKELTON LAKE AREA					
Tuff of Skelton Lake	KB 080621-1	37.576771, -118.976392	x		x
Inclusion in tuff of Skelton Lake	KB 080621-2	37.576771, -118.976392	x		x
RED AND WHITE SPUR AREA					
Coarse lithic-rich facies	KB 081521-1	37.495000, -118.872360	x	x	x
Fine lithic-rich facies	KB 081521-2	37.493150, -118.874730	x		x
"Breccia" facies	KB 081521-3	37.489820, -118.873170	x		x

Table A: Sample names, locations, and analyses performed.

4. FACIES DESCRIPTIONS

Sample locations for the Agnew Meadows area are shown in Fig. 4, Skelton Lake area in Fig. 5, and Red and White Spur area in Fig. 6. Coordinates for each sample location are provided in Table 1. There are no definitive sedimentological facing indicators. Complete hand sample and thin section descriptions are in Appendix A.

4.1 AGNEW MEADOWS AREA

4.1.1 Tuff of Agnew Meadows

The lowermost unit in the Agnew Meadows area is a lithic-rich tuff at least 150 m thick (unit Tram in Fig. 2) with weak foliation defined by 5-15% elongate pumice pieces and lithic fragments 3-15 cm long of varying lithology (Fig. 8). This unit contains 15% sedimentary lithic clasts ranging in size from 3-20 cm, 5% quartzite clasts (5-15 cm), and rare (1%) giant elongate quartzite clasts (1 m) in an orange, weathered, fine- to medium-grained groundmass. The fine-grained groundmass encloses 15% subhedral to anhedral quartz and feldspar phenocrysts (2 mm-1 cm). In thin section, the tuff is 3-10% subhedral to anhedral quartz phenocrysts (1-5 mm) and 5-7% subhedral feldspar phenocrysts with sericite alteration (2 mm-1 cm).

Figure 8: The tuff of Agnew Meadows showing fine-grained lithic fragments and pumice that define a slight foliation (arrow points to grey lithic). Ruler is 15 cm long.

4.1.2 Lower grey lithic tuff

The lower grey lithic tuff overlies the tuff of Agnew Meadows (Fig. 2) and is approximately 50 m thick with abundant (15-60%) elongate lithic fragments (2 mm-3 cm) and 2% grey and tan pumice pieces (2 cm) that define a weak foliation (Figs. 9). This unit contains 3-10% quartz phenocrysts (1-2 mm) in an aphanitic groundmass that has a sugary, altered appearance. Abundant sericite alteration is apparent in thin section (Fig. 10) and makes up 25-85% of the rock. Phenocrysts in thin section include 2-4% subhedral to anhedral quartz (1-2 mm), 1% embayed, anhedral quartz (0.5mm), 0.5% subhedral to anhedral plagioclase (0.5 mm), 1% anhedral K-spar with partial sericite alteration (1 mm), and ≤1% subhedral oxide minerals.

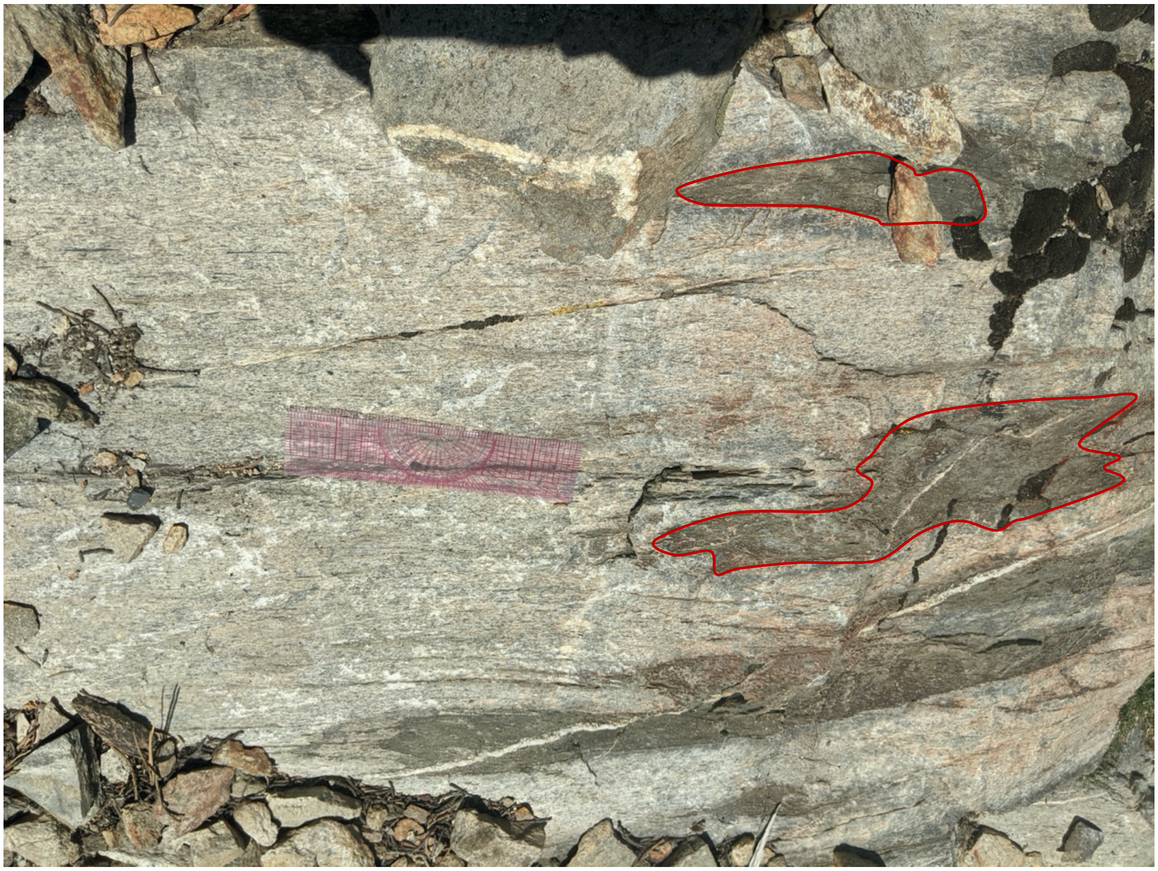

Figure 9: Lower grey lithic tuff with elongate grey clasts (outlined in red) in a light grey groundmass. Ruler is 15 cm long.

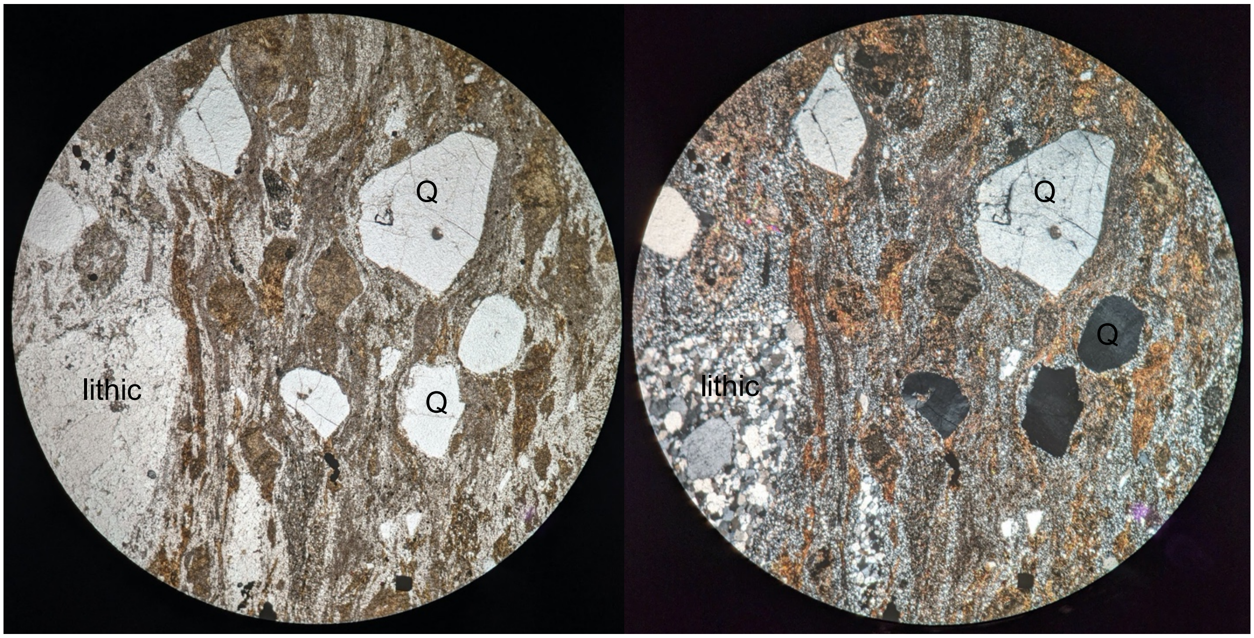

Figure 10: Lower grey lithic tuff (Sample KB 080521-1). A quartzite lithic fragment (lithic) and quartz phenocrysts (Q) are surrounded by a groundmass of quartz and feldspar crystals. Image on left is in plane-polarized light, right image is in cross-polarized light. 4x magnification.

A grey clast in the lower grey lithic tuff is dark grey with a mm-scale diffuse, flame-like boundary with the host tuff. The clast contains 5% equant to elongate quartz phenocrysts (< 1 mm) in an aphanitic groundmass. The boundary between the clast and the surrounding lower grey lithic tuff is ~5 mm thick and grades from the grey clast to a white boundary zone, to the medium grey lower grey lithic tuff. The clast is less resistant than the overall rock, such that the phenocrysts in the clast are more resistant to weathering compared to the rest of the clast. In thin section, the fine-grained groundmass of the clast is composed of 85% quartz and micas. Phenocrysts include 2% subhedral quartz (1 mm), 3% subhedral quartz (0.5 mm), 0.5% subhedral quartz (2 mm), and 1% anhedral K-spar with sericite alteration (1 mm) as well as 6%

elongate pumice pieces (2 mm) that have altered to mica and define a slight foliation around the phenocrysts (Fig. 11).

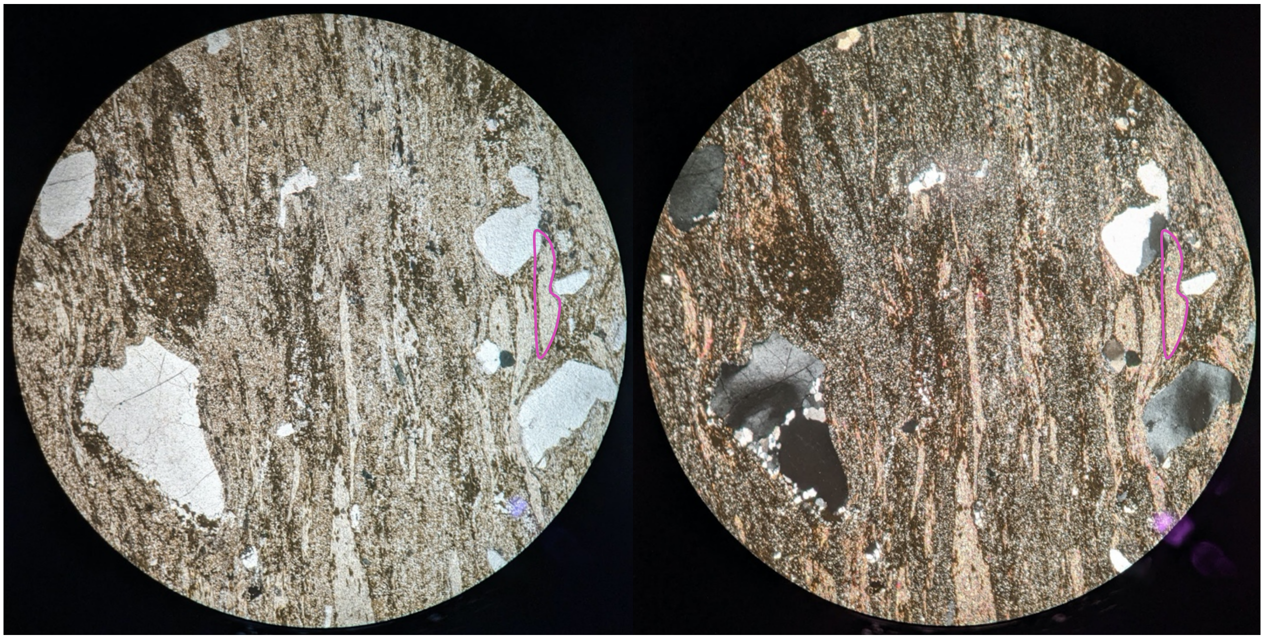

Figure 11: Thin section of the clast in lower grey lithic tuff (Sample KB 080721-1B). Note light brown pumice pieces of mica replacement (outlined in pink) bent around larger quartz phenocrysts. Image on left is in plane-polarized light, right image is in cross-polarized light. 4x magnification.

4.1.3 Pumice conglomerate

The pumice conglomerate is the main focus of this study, and much more detailed field and lab analysis was carried out for this unit. The pumice conglomerate overlies the lower grey lithic tuff and is 0.75 km along strike and ~40 km-thick (Fig. 2) with large (15 cm-1 m long) tan elongate pumice clasts that define a foliation and are surrounded by a grey-brown matrix (Fig. 12). Outcrops of pumice conglomerate also lie along strike within the upper grey lithic tuff and the lower grey lithic tuff to the southeast of the main pumice conglomerate deposit (Fig. 2). The small (2 m x 5 m) outcrops are matrix supported but are otherwise texturally and compositionally similar to the main deposit to the northeast. The matrix in all parts of the conglomerate is 5% quartz phenocrysts (1 mm) in a grey, sugary groundmass. In thin section, the pumice clasts have 5% quartz phenocrysts (0.1-1 mm), 2% K-spar with sericite alteration (0.1 mm), and 5% elongate pumiceous pieces in a fine-grained groundmass (Fig. 13). The groundmass is microcrystalline and is composed of 85% quartz and feldspar (<1 mm). The matrix of the conglomerate is dark grey-brown and thin section shows a fine-grained groundmass with quartz and feldspar crystals and sericite and epidote alteration. Phenocrysts include 4% subhedral to anhedral quartz (0.5 -2 mm) and ≤ 1% anhedral K-spar with sericite alteration (0.5 mm). The matrix also contains 10% fiamme (0.5-2 mm) that have altered to mica and are deformed around phenocrysts (Fig. 14). Approximately 3% of the tan pumice clasts contain a concentric dark interior (Fig. 15; ~5% of the clast). In thin section (Fig. 16), the composition of the dark interior is difficult to identify, but altered mafic minerals, mica, and sericite and epidote alteration make up 90% of the material. The contact between the dark interior and the rest of the pumice clast is sharp. A small fraction (5%) of the pumice clasts make contact or appear to be fused together at either the ends or the edges of individual clasts. No more than three clasts are connected in any area. The concentration of pumice clasts is laterally discontinuous, with the interior of the unit having a higher concentration of larger pumice clasts than the stratigraphic edges, top, and bottom. The clast density at the stratigraphic and lateral edges of this unit is <25% with average clast length ~10 cm, and at the stratigraphic and lateral middle, the clast density is >50% with average clast length ~25 cm.

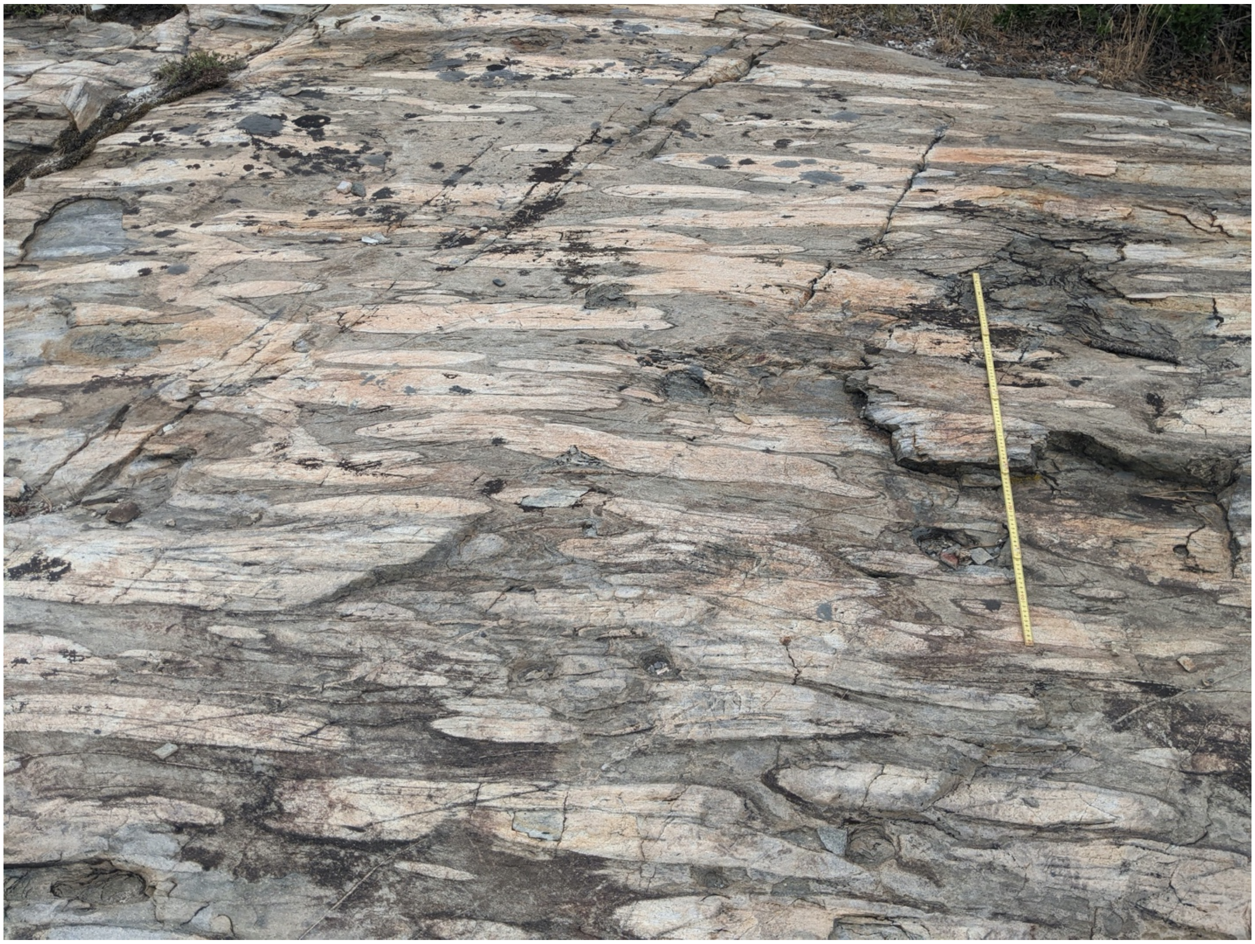

Figure 12: Pumice conglomerate outcrop in an area with high concentration of pumice clasts. Ruler is 1 m long.

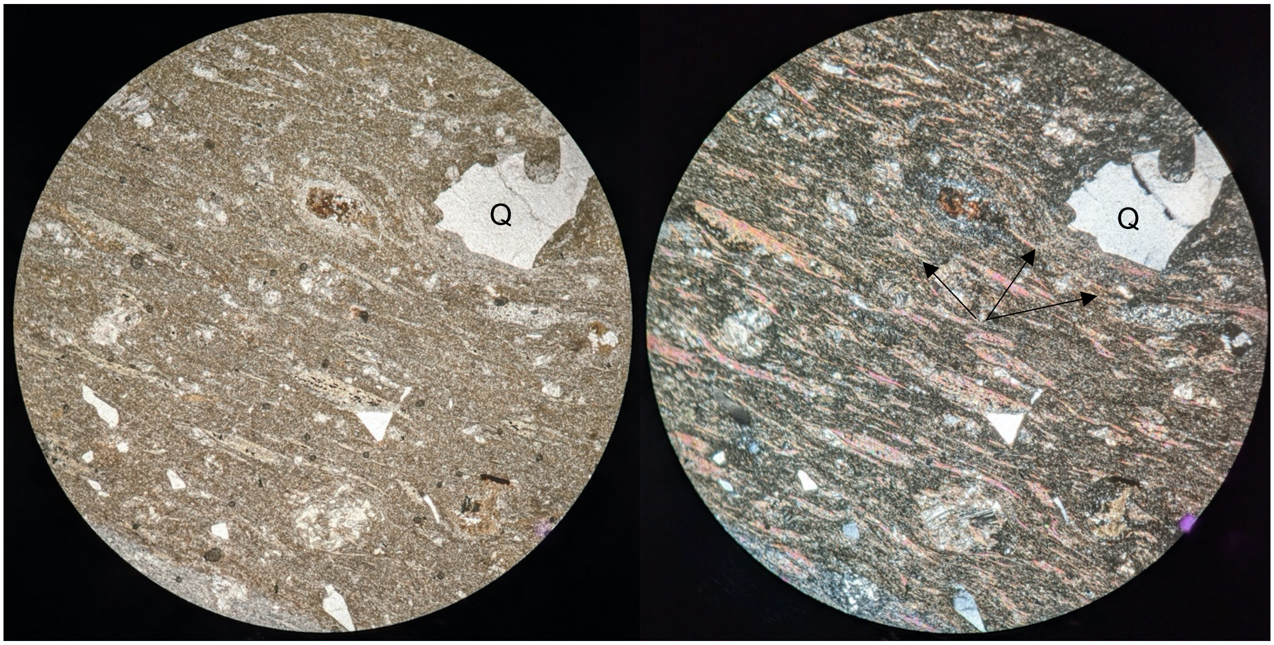

Figure 13: Pumice clast in pumice conglomerate. A broken quartz crystal (Q) in the top right is surrounded by bent fiamme (arrows). Left image is plane-polarized light and right image is cross-polarized light. 4x magnification. Sample KB 080921-2.

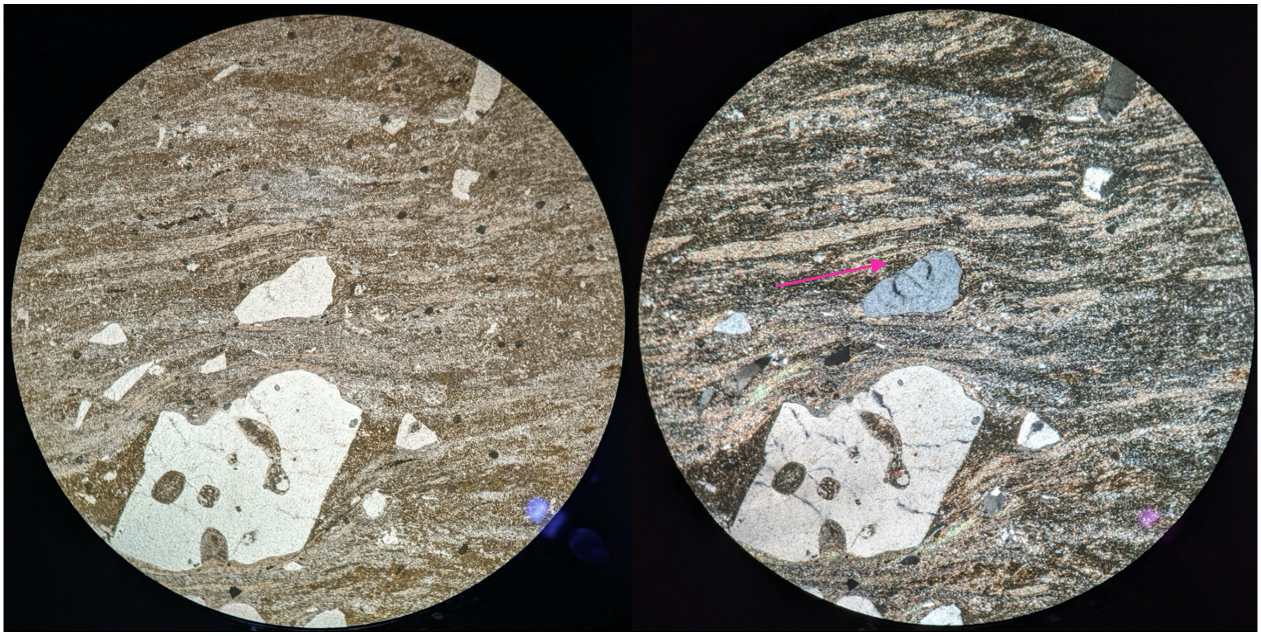

Figure 14: Pumice conglomerate matrix showing fiamme bent around quartz phenocrysts. Image on the left is in plane-polarized light, right image is cross-polarized light. 4x magnification. Sample KB 080521-2A.

Figure 15: Pumice in pumice conglomerate showing dark interiors (below ruler). Ruler is 15 cm long.

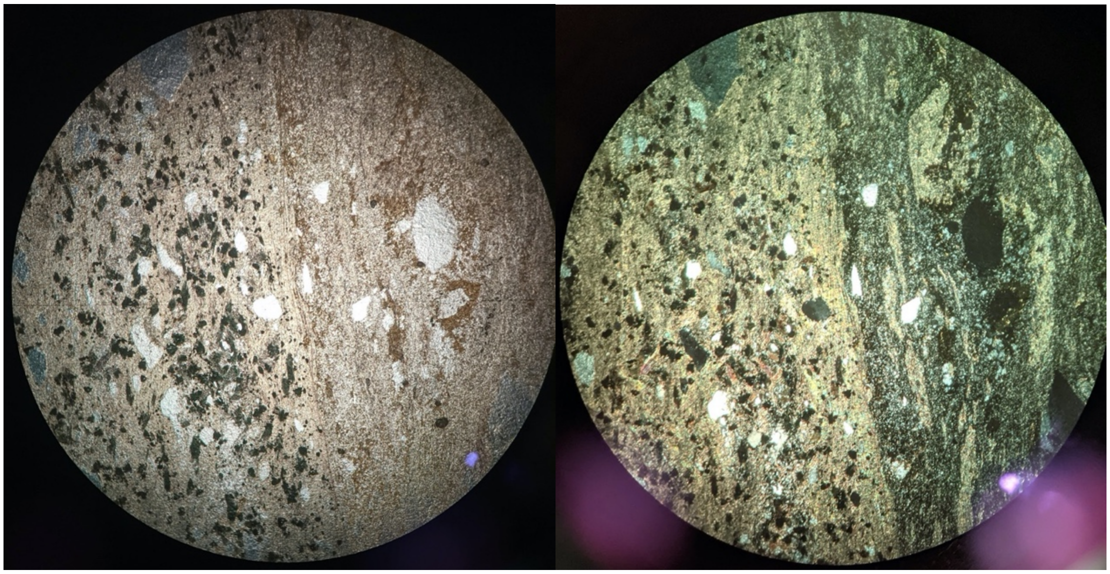

Figure 16: Dark interior of pumice clast in the pumice conglomerate. The dark interior is on the left in both images (L:PPL, R:XPL; 4x magnification). The contact is sharp and most of the interior is altered mafic material and mica. Sample KB 080821-1.

4.1.4 Upper grey lithic tuff

The upper grey lithic tuff (Fig. 2) overlies and surrounds the pumice conglomerate and is a thin (10 m) unit that contains grey pumice pieces in a fine- to medium-grained groundmass (Fig. 17). The contact between this tuff and the pumice conglomerate is irregular and gradational (Fig. 18). This tuff contains rare lenses of very dark grey, aphanitic material and mm-scale layers with quartz and feldspar phenocrysts or abundant (30%) tan, elongate pumice clasts. Lithic fragments are primarily quartzite (<0.25 mm). Phenocrysts include 5% equant, subhedral quartz (1-2 mm) and 6% equant, subhedral feldspar (1-3 mm). Analysis of thin sections reveals that the groundmass is 85% microcrystalline quartz and feldspar crystals with epidote and sericite alteration (Fig. 19). Phenocrysts include 3-6% subhedral to anhedral quartz (1-2 mm), 1-3% anhedral, fractured K-spar with sericite alteration (1-2 mm), 1% anhedral plagioclase (0.5-0.75 mm), and 1% fractured K-spar glomerocrysts (4 mm). This unit also contains 6% ribbons of biotite (1-2 mm), 5% fine-grained quartzite fragments (2-5 mm long), and 5% pumiceous fragments (2.5 mm) deformed around phenocrysts.

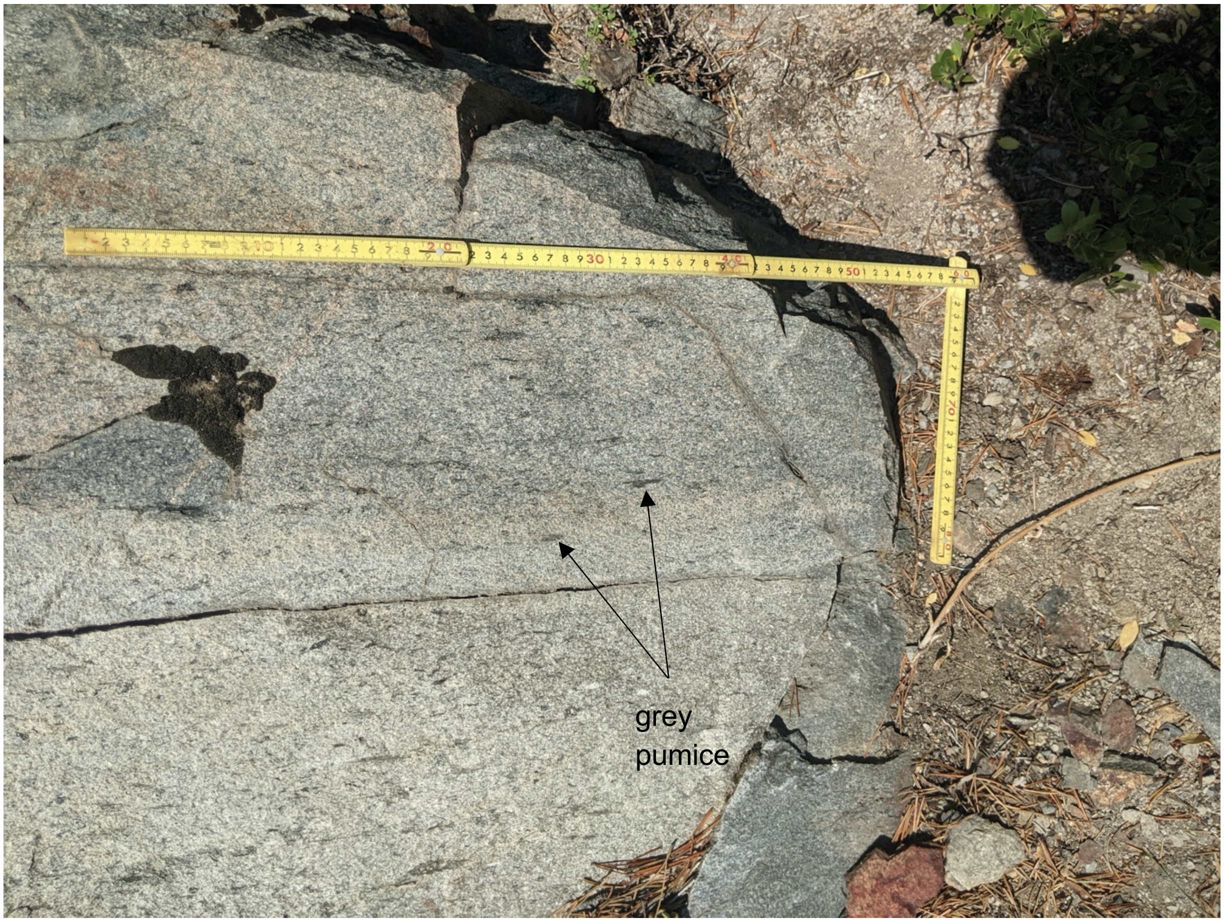

Figure 17: Upper grey lithic tuff, showing foliation defined by small, dark grey pumiceous pieces in the grey groundmass. Black ruler increments are 1 cm.

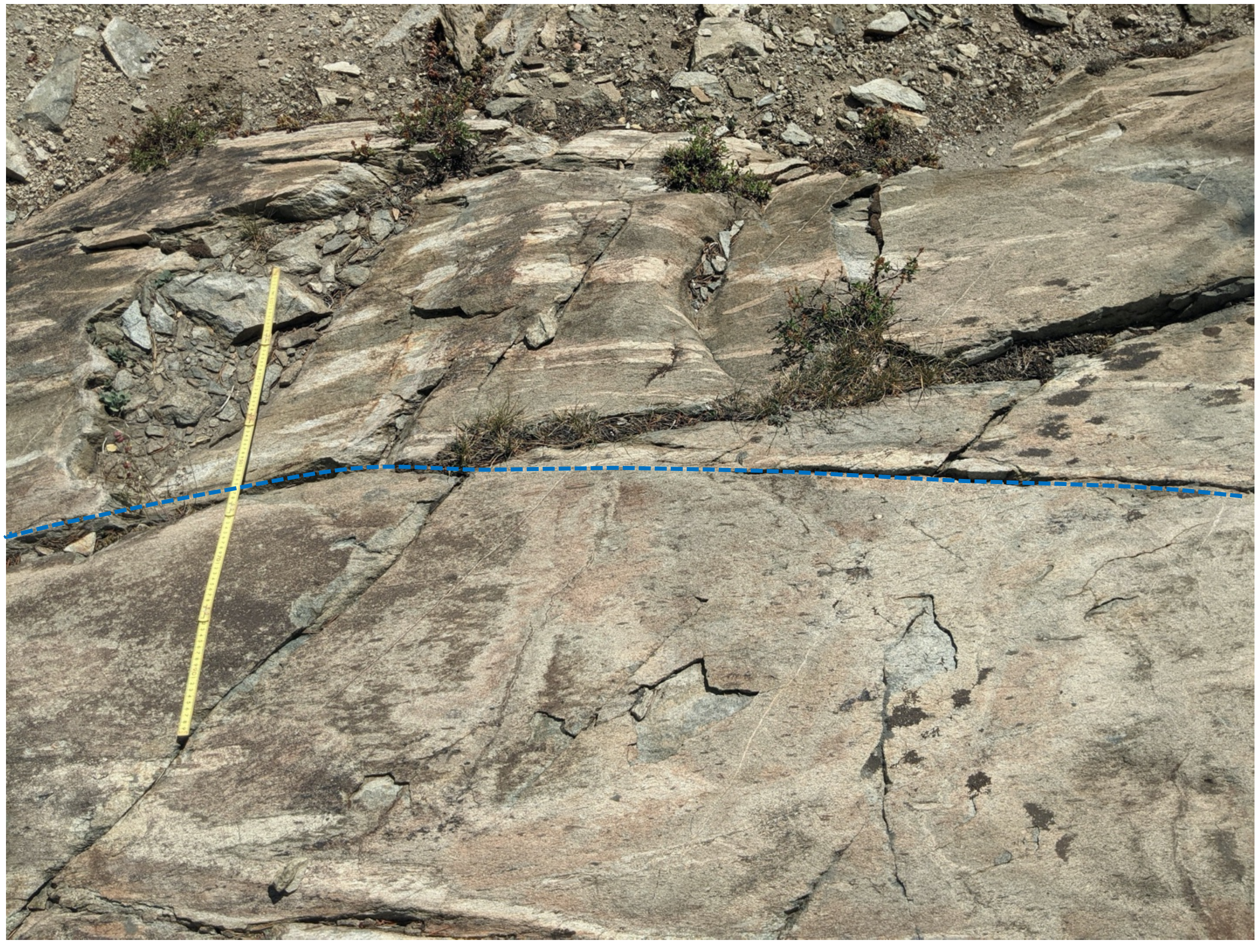

Figure 18: Contact (blue dashed line) between pumice conglomerate (top) and upper grey lithic tuff (bottom). Note how sparse the clasts are at the contact. Ruler is 1 m long.

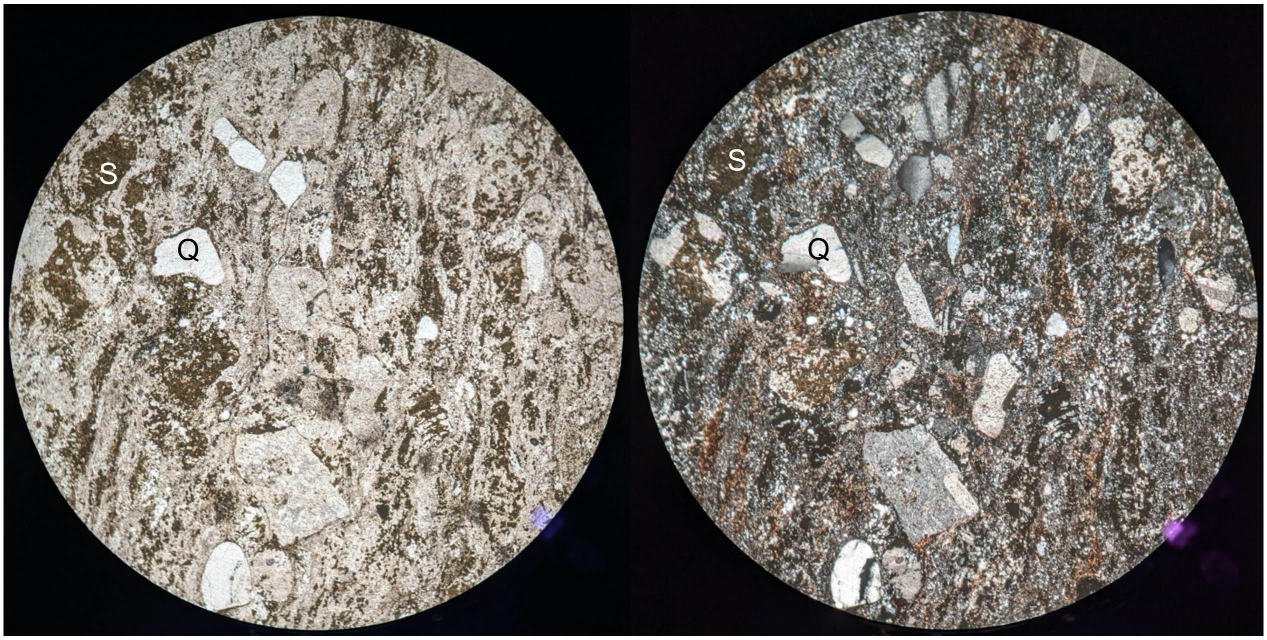

Figure 19: Upper grey lithic tuff. Note the quartz (Q) phenocrysts and sericite alteration (S). Left image is in plane-polarized light, right image is cross-polarized light. 4x magnification. Sample KB 080921-3.

4.1.5 Tuff southeast of pumice conglomerate

A dark grey tuff approximately 10 m thick crops out southeast of the pumice conglomerate (Fig. 2) and contains abundant grey pumice pieces and rare lithic fragments in an aphanitic groundmass. This unit is 7% quartz phenocrysts (1-2 mm), 1% K-spar phenocrysts (2 mm), and 20% elongate dark grey pumiceous pieces (1-3 cm) that define a weak foliation and are bent around subhedral quartz phenocrysts. In thin section (Fig. 20), the groundmass (80%) is microcrystalline and composed of quartz, feldspars, and micas with epidote and sericite alteration. Phenocrysts include 2% subhedral quartz (3 mm), 2% euhedral quartz (1 mm), 2% magnetite (0.5 mm), 4% anhedral K-spar with sericite alteration (1-2 mm), and 6% altered mafic minerals (≤ 1 mm).

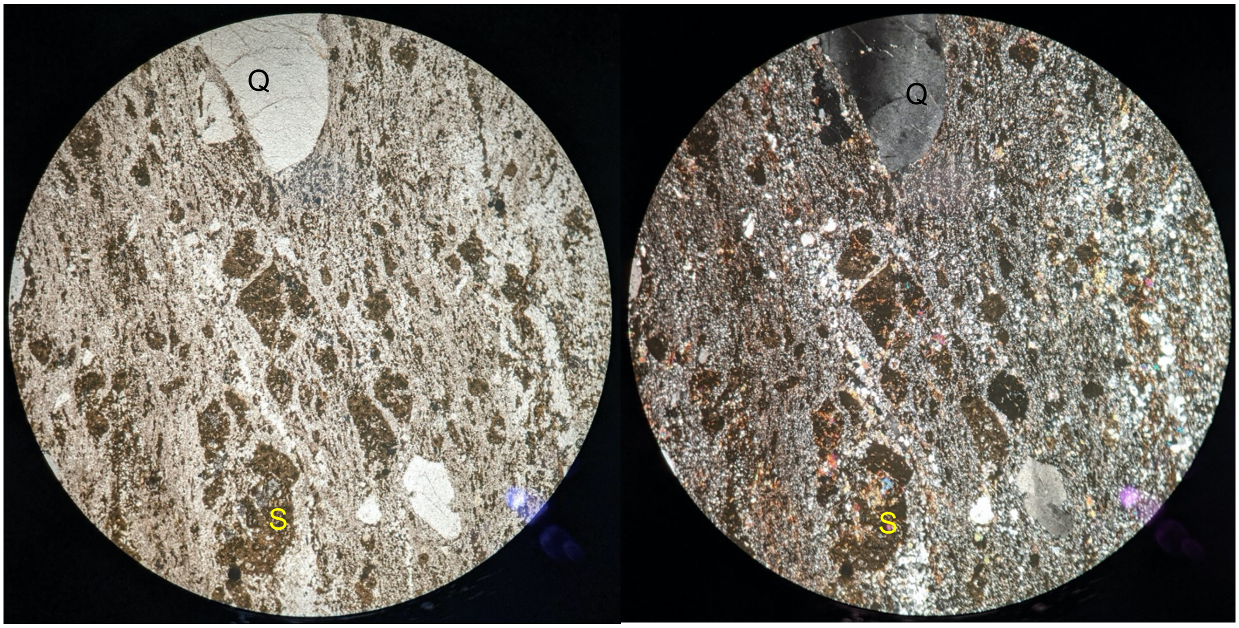

Figure 20: Tuff southeast of pumice conglomerate. Quartz (Q) and sericitized K-felspar (S) phenocrysts are surrounded by a fine-grained groundmass of quartz and sericitized feldpsars. L: PPL, R: XPL, 4x magnification. Sample KB 080821-1.

4.1.6 Tuff of San Joaquin Mountain

The tuff of San Joaquin Mountain (described previously by Barth et al., 2018) overlies the upper grey lithic tuff (Fig. 2). This unit is a ~40 m-thick, lithic tuff containing tiny (1-3 mm) wispy grey elongate pumice, rare dark grey elongate lithic fragments (1-3 cm), and quartz and feldspar phenocrysts in a medium-grained dark grey groundmass (Fig. 21). Foliation is defined by the wispy pumice. In thin section (Fig. 22), the fine-grained groundmass (80% of the rock) is equal proportions quartz and feldspar crystals with epidote and sericite alteration. Phenocrysts include 5% subhedral to anhedral, fractured quartz (2-3 mm), 3% subhedral plagioclase (2-3 mm), and 2% subhedral K-spar (1-2 mm) with sericite alteration. This unit also contains 3%

quartzite lithic fragments (2 mm) and 7% epidote- and mica-altered pumice fragments (2-4 mm long) bent around phenocrysts.

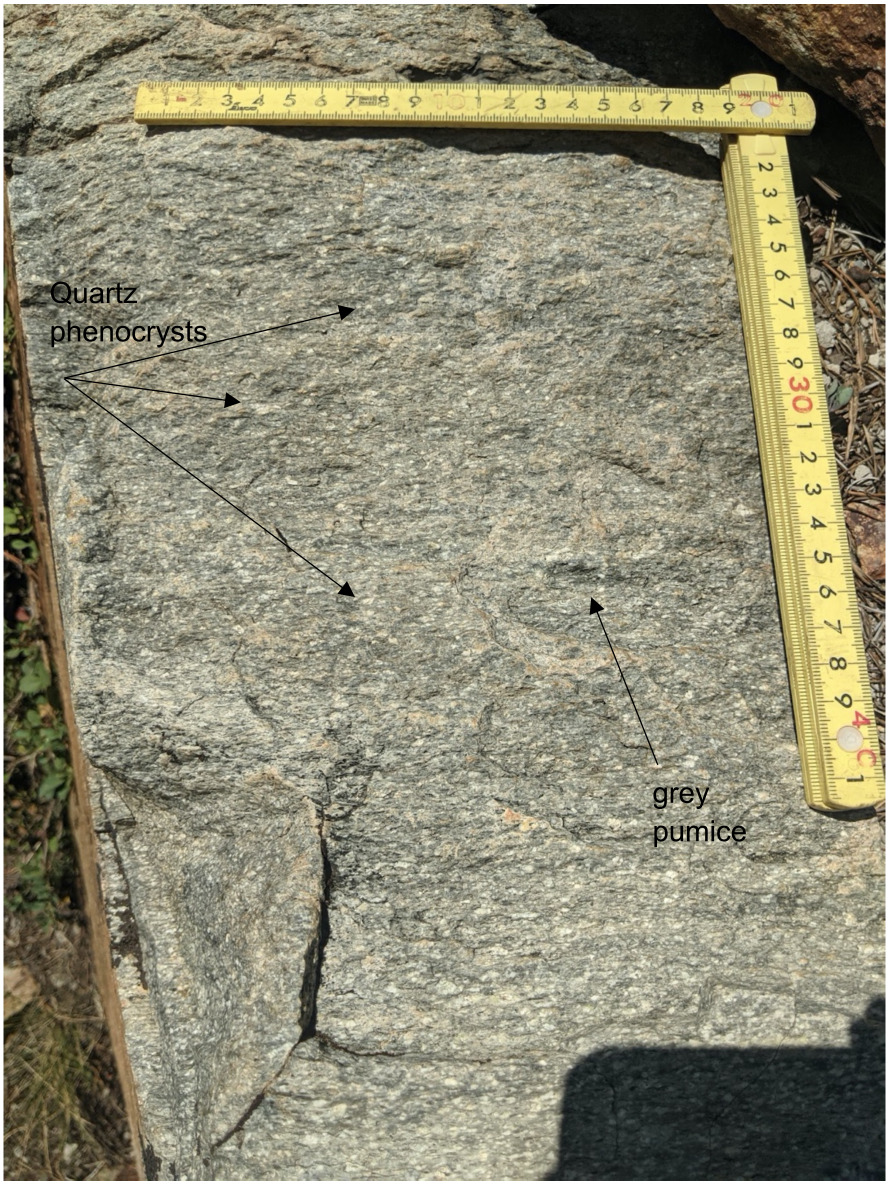

Figure 21: Tuff of San Joaquin Mtn. Note the sub-centimeter quartz phenocrysts. Black ruler increments are 1 cm.

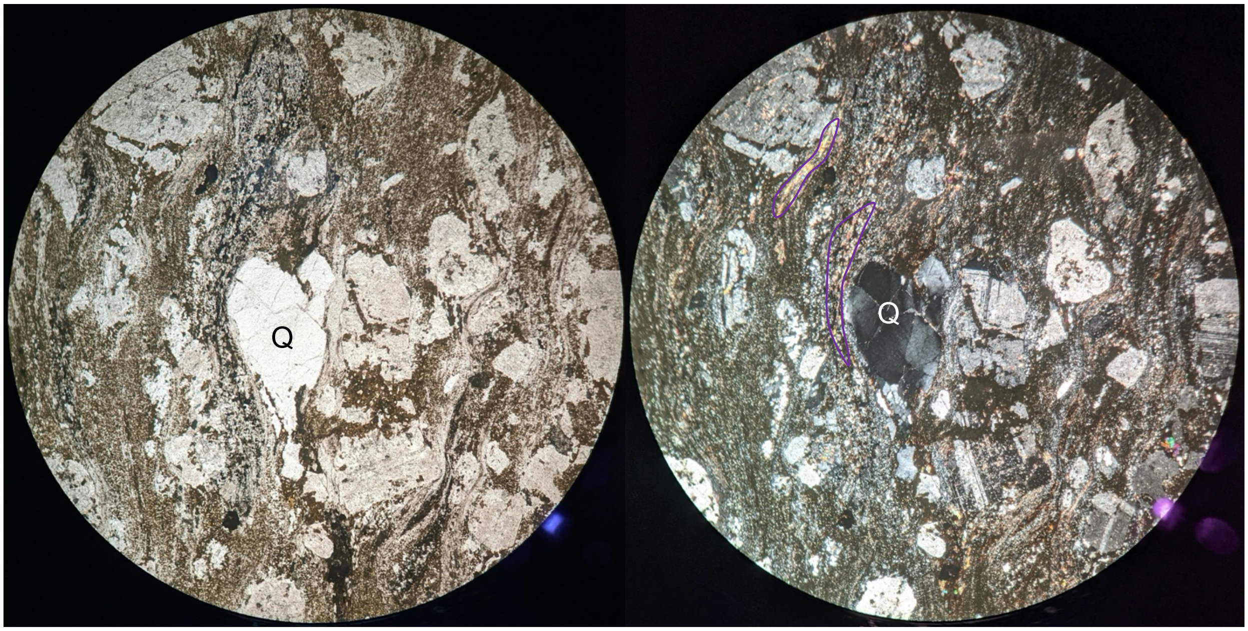

Figure 22: tuff of San Joaquin Mtn. Note the fiamme (purple outline) bent around the quartz phenocrysts (Q). Left image is in plane-polarized light, right is cross-polarized light. 4x magnification. Sample KB 081021-1.

4.1.7 Quartzite conglomerate

The quartzite conglomerate is a thin (15 m), laterally discontinuous unit that overlies the upper grey lithic tuff (Fig. 2). This unit is poorly sorted, matrix supported, and ungraded with abundant quartzite lithic fragments likely derived from the Paleozoic Palmetto Formation and undifferentiated Paleozoic metasedimentary clasts ranging in size from 0.5 cm to 25 cm in an orange, weathered matrix (Figs. 23, 24). Some clasts are preferentially weathered leaving only voids. In thin section, the microcrystalline matrix is 85% of the rock and contains broken quartz and K-spar with sericite alteration. Phenocrysts include 2% subhedral quartz (1 mm) and 1% K-spar with sericite alteration (0.5 mm). This rock also contains 7% quartzite lithic clasts (2mm-1.5 cm), 2% clasts composed of calcite (3 mm), and 3% pumice pieces (2-3 mm) wrapped around lithic clasts and phenocrysts.

Figure 23: Quartzite conglomerate with a variety of clast types, shapes, and sizes, with many void spaces. Dark oval shapes are voids. Ruler is 1 m long in photo.

Figure 24: Quartzite conglomerate with a variety of clast types, shapes, and sizes, with many void spaces. Dark oval shapes are voids and the large white clast is quartzite. Black ruler increments are 1 cm.

4.2 SKELTON LAKE AREA

4.2.1 Tuff of Skelton Lake

The tuff of Skelton Lake (Fig. 4) is a thick, laterally continuous dark grey, porphyritic tuff containing abundant quartz and feldspar phenocrysts, dark grey lithic fragments, and grey pumice pieces in a medium-grained grey groundmass (Fig. 25). Pumice pieces are elongate and have irregular boundaries with the groundmass. Other clasts are very dark grey, irregularly shaped, and not as elongate as pumice pieces and volcanic clasts. These lithic clasts range in size from 3-10 cm and are quartzite (1%) and undifferentiated Paleozoic (?) grey metasedimentary rocks (5%). Subhedral quartz and feldspar phenocrysts (25%, 1-2 mm, Fig. 26) are surrounded by a cryptocrystalline groundmass.

Figure 25: Tuff of Skelton Lake at Skelton Lake. Ruler increments are 1 cm. The clast pictured in the middle is a black ellipsoidal clast that contains abundant glomerocrysts of quartz and feldspar crystals.

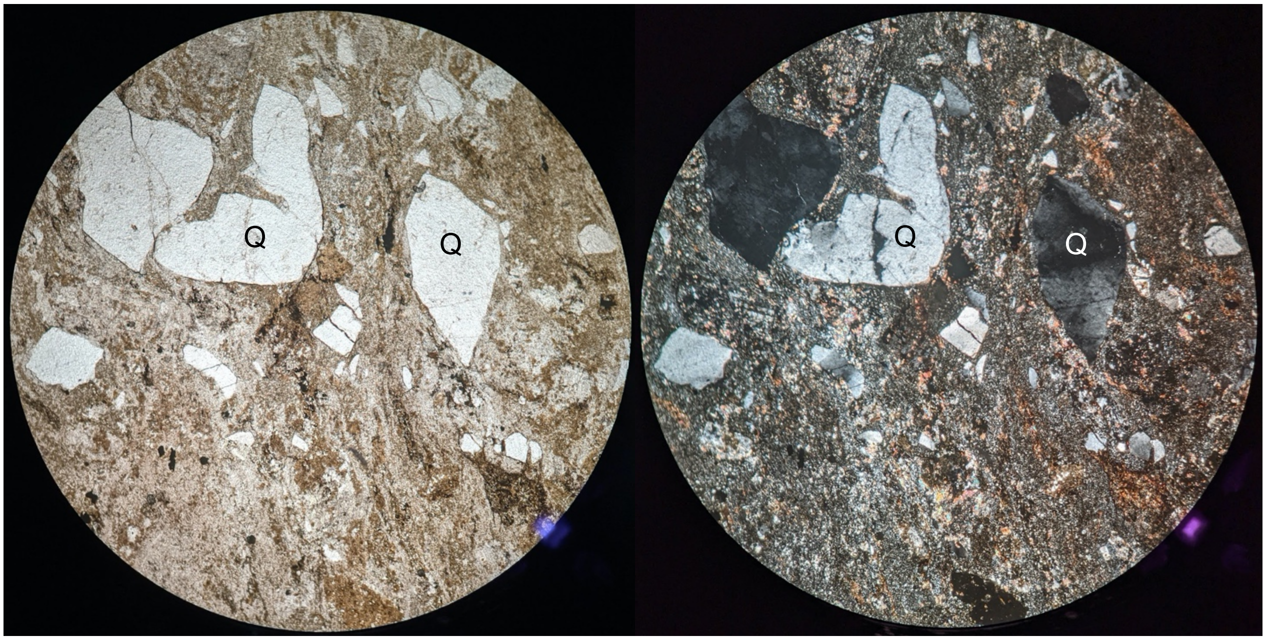

Figure 26: Tuff of Skelton Lake at Skelton Lake. Note the large quartz phenocrysts (Q) in a fine-grained groundmass. Left image is in plane-polarized light, right is cross-polarized light. 4x magnification. Sample KB 080621-1.

The tuff of Skelton Lake also contains rare dark grey to black volcanic ellipsoidal clasts that contain abundant glomerocrysts (Fig. 25) of equal parts quartz and feldspars (0.5-2 mm crystals in clusters measuring ~2 cm) in an aphanitic black groundmass. The groundmass in these clasts is mostly too small and altered to identify, but in thin section is ~7% amphibole (0.5-2 mm, Fig. 27). The volcanic clasts are 5 to 25 cm long and have sharp boundaries with the groundmass.

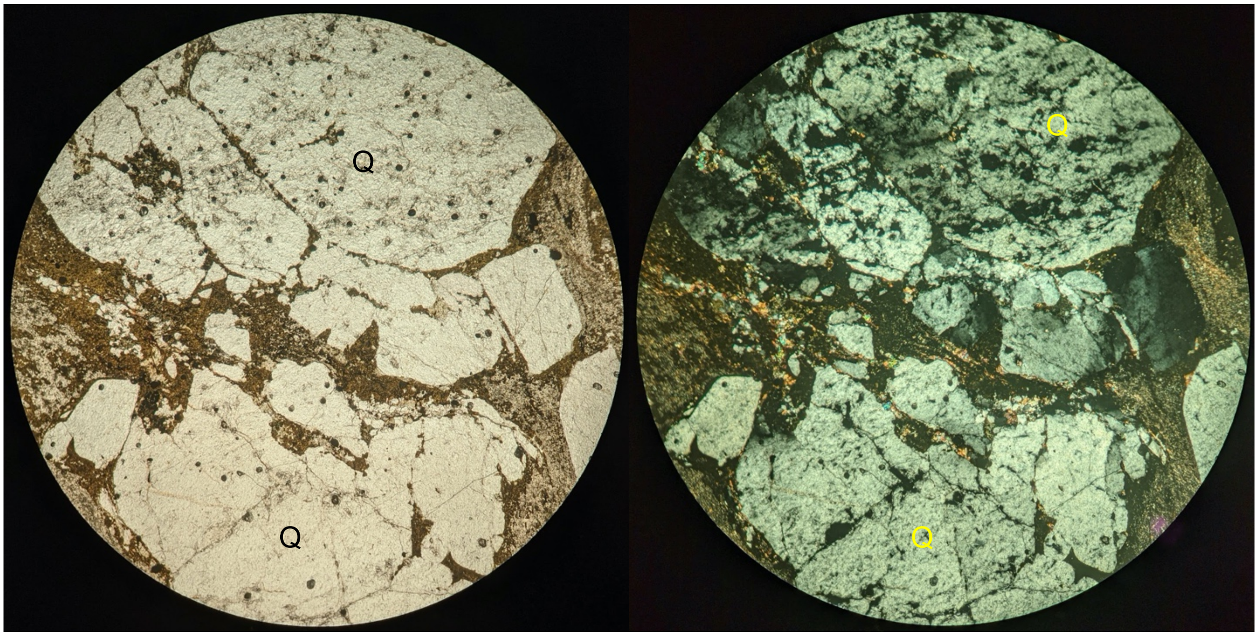

Figure 27: Glomerocryst in a clast in the tuff of Skelton Lake at Skelton Lake. Note the large quartz crystals surrounded by unidentifiable groundmass. Left image is in plane-polarized light, right is cross-polarized light. 4x magnification. Sample KB 080621-2.

4.3 RED AND WHITE SPUR AREA

4.3.1 Coarse lithic-rich tuff

The coarse lithic-rich tuff in the Red and White Spur Area is the thickest unit (100 m) in the area and overlies a fine-grained lithic tuff (Fig. 3). The lithic-rich tuff is a non-foliated grey tuff containing abundant (15%) irregularly shaped or elongate, aphanitic grey lithic fragments (1-15 cm long) and 15% elongate or irregularly shaped grey vesicular pumice pieces (3-7 cm) in a fine-grained light grey groundmass (Figs. 28 and 29). Approximately 35% of the pumice pieces are grey with 7% white phenocrysts (1-2 mm). The groundmass of the tuff is 10% quartz phenocrysts (1-3 mm) and 7% feldspar phenocrysts (1-2 mm) in a light grey aphanitic groundmass. In thin section (Fig. 30), the fine-grained groundmass is quartz and feldspars with epidote and sericite alteration throughout and makes up 90% of the rock. Phenocrysts include 5% subhedral, fractured quartz (2-4 mm), 2% subhedral K-spar with sericite alteration (2-3 mm), and 3% subhedral hornblende (1 mm).

Figure 28: Lithic-rich tuff at Red and White Spur. Ruler increments are 1 cm. Clasts are a mix of rock types, including aphanitic grey sedimentary clasts and grey vesicular pumice.

Figure 29: Sedimentary lithic clasts and a large vesicular dark grey pumice in the coarse-grained lithic-rich tuff at Red and White Spur. Black ruler increments are 1 cm.

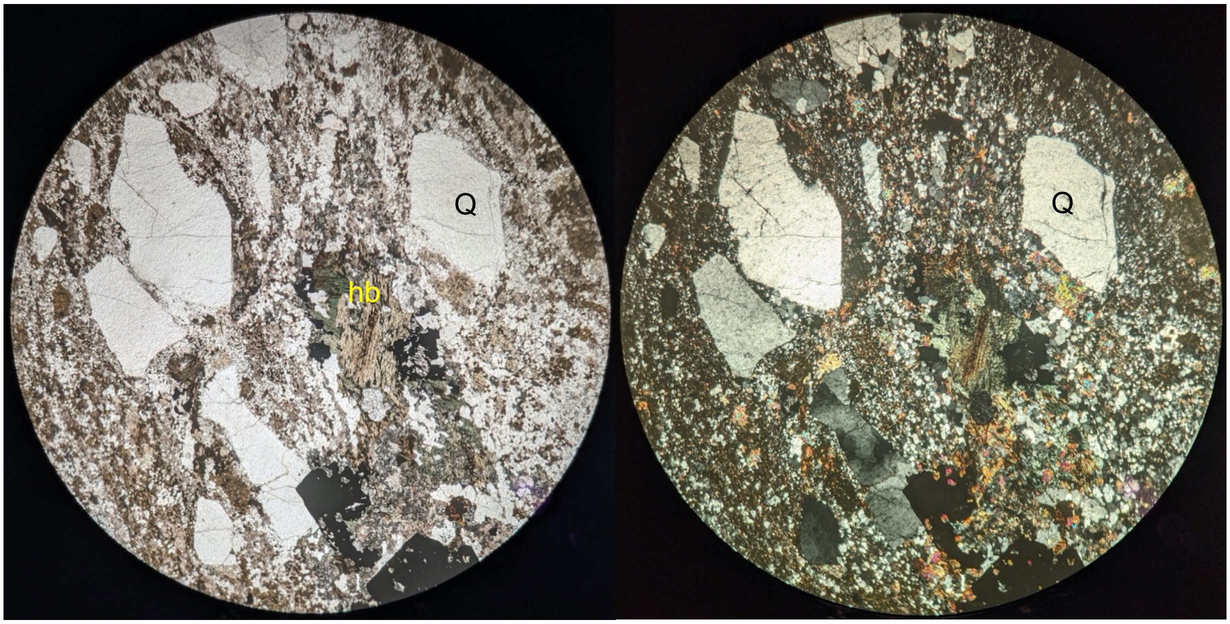

Figure 30: Lithic tuff in Red and White Spur area. Note the quartz (Q) and hornblende (hb) phenocrysts surrounded by a medium-grained groundmass of quartz and feldspar crystals. Left image is in plane-polarized light, right is cross-polarized light. 4x magnification. Sample KB 081521-1.

4.3.2 Fine-grained lithic tuff

The fine-grained lithic tuff is a thin (25 m) fine-grained grey tuff in the Red and White Area with irregularly shaped, aphanitic grey lithic fragments (1-7 cm) and elongate grey pumice pieces (1-2 cm) in an aphanitic, light grey groundmass (Fig. 3, 31). The clasts are smaller and lower abundance, and the matrix is finer grained than the lithic-rich tuff at Red and White Spur, but this unit contains similar proportions of lithic clasts and pumice fragments. Most lithic fragments are vesicular with <5% quartz phenocrysts (1 mm) and the matrix has 15% quartz (1-3 mm) and 15% feldspars (1-3 mm). In thin section (Fig. 32), the groundmass (90% of the rock) is fine to medium grained with quartz, plagioclase and K-feldspars, and biotite with epidote and sericite alteration throughout. Phenocrysts throughout include 5% subhedral, fractured quartz

(2-5 mm), 4% subhedral K-spar (1-2 mm), and 1% plagioclase (1 mm). This unit also contains 1% altered mafic crystals (3-5 mm).

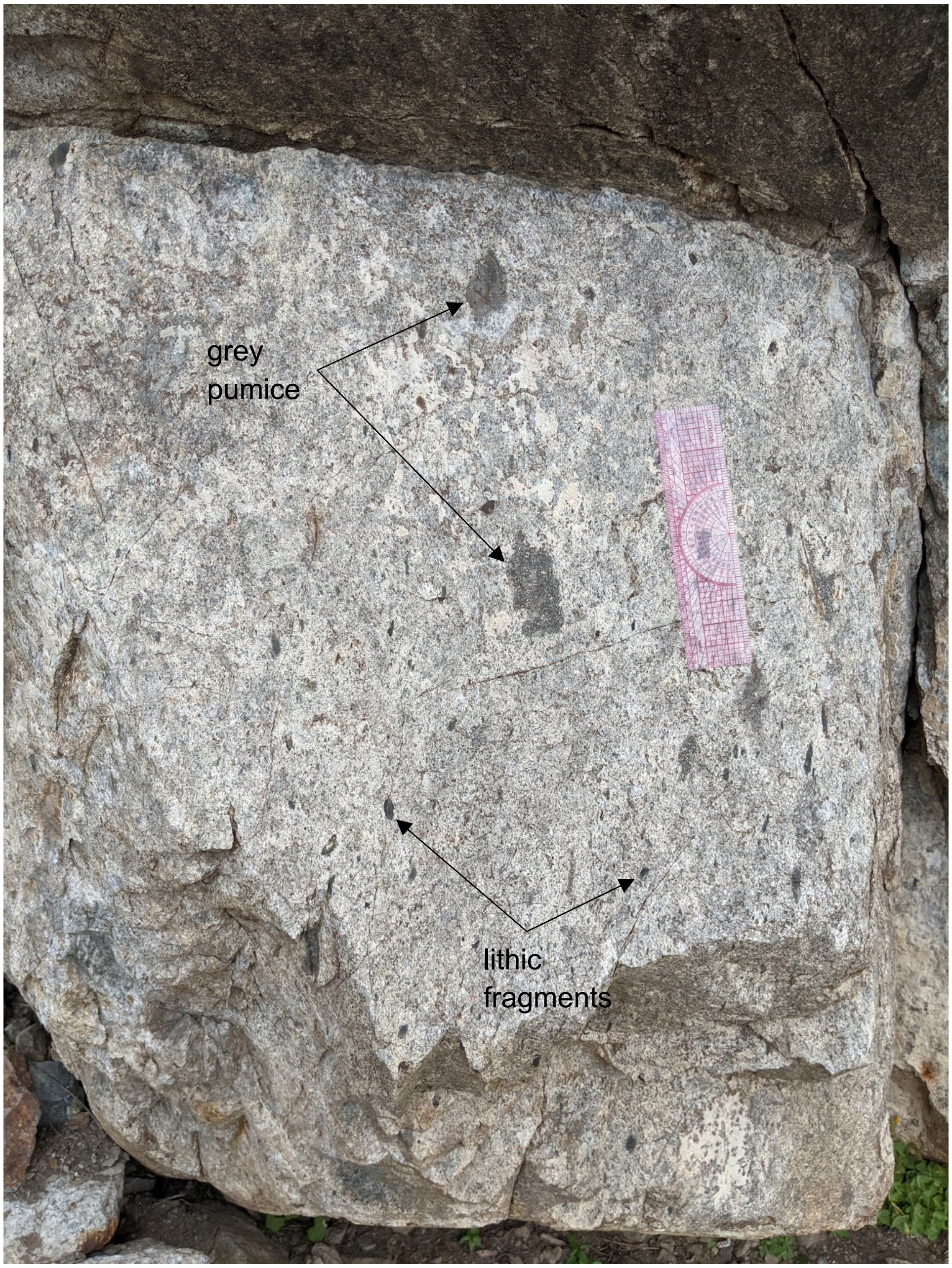

Figure 31: Finer-grained lithic tuff at Red and White Spur. Note the presence of grey lithic fragments and pumice clasts that are smaller than those in the coarse-grained lithic tuff nearby. Ruler is 15 cm long.

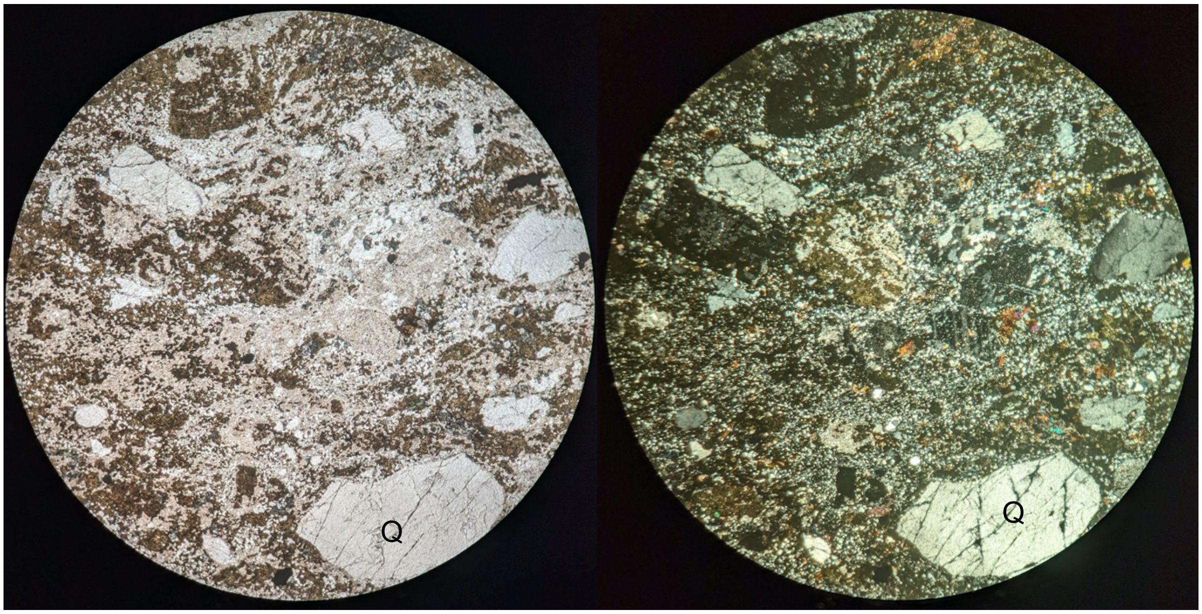

Figure 32: Finer-grained lithic tuff at Red and White Spur area. Note the quartz phenocrysts (Q) surrounded by a fine- to medium-grained groundmass of quartz crystals. Left image is in plane-polarized light, right is cross-polarized light. 4x magnification. Sample KB 081521-2.

4.3.3 Fine-grained facies of the tuff of Skelton Lake

The fine-grained facies at Red and White Spur (Fig. 3) is a laterally discontinuous, light grey, non-foliated tuffaceous volcanic rock with 10% quartz phenocrysts (0.5-4 mm) in a light grey, aphanitic groundmass. In thin section (Fig. 33), the fine- to medium-grained groundmass (90% of the rock) is composed of quartz, feldspar, and biotite with epidote and sericite alteration throughout. Phenocrysts include 8% subhedral to anhedral quartz (2-5 mm), 2% subhedral plagioclase (1-2 mm), and 0.5% subhedral K-spar with sericite alteration (1 mm). This unit also includes rare glomerocrysts containing 95% quartz (1 mm) and 5% biotite (1 mm).

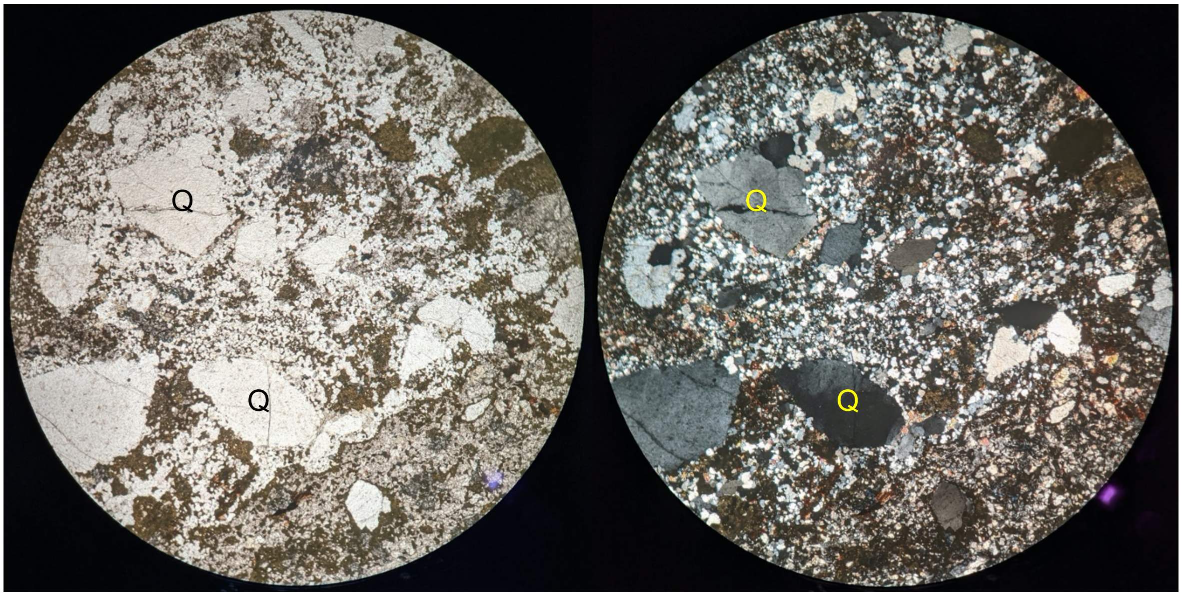

Figure 33: Fine-grained facies at Red and White Spur area. Note the quartz phenocrysts (Q) surrounded by a medium-grained groundmass of quartz and feldspar crystals. Left image is in plane-polarized light, right is cross-polarized light. 4x magnification. Sample KB 081521-3.

5. GEOCHRONOLOGY

Zircon crystals were extracted from samples from two units in the Agnew Meadows area of the Ritter Range pendant and one unit in the Red and White Spur in the Mount Morrison pendant (Table A) for U-Pb age analysis. Zircon crystallization ages are representative of individual rock units, and all samples returned a range of ages greater than the total analytical error. This may mean that radiogenic lead loss may have occurred, and/or that antecrysts and xenocrysts are included in the analyses. Ages are compared using IsoplotR (Vermeesch, 2018) and TuffZirc (Ludwig, 2003) statistical analyses, and returned statistically identical ages. All zircon U-Pb data are provided in Appendix B.

5.1 ROCKS IN AGNEW MEADOWS, RITTER RANGE PENDANT

Volcaniclastic units in the Agnew Meadows area of the Ritter Range pendant are Triassic in age. Barth et al. (2018) reported several ages for units in this area, including for the tuff of Agnew Meadows (220 ± 2 Ma) and the tuff of San Joaquin Mountain (218 ± 2 Ma). Two additional samples from this area were analyzed: lower grey lithic tuff and upper grey lithic tuff (Figs. 2, 5). Both samples contained abundant zircon crystals.

The oldest volcaniclastic unit (220 ± 2 Ma) in the Agnew Meadows sequence is the previously analyzed tuff of Agnew Meadows (Barth et al., 2018). The overlying lower grey lithic tuff (Figs. 2, 5; KB 081221-2) yielded 57 concordant zircons with a range of crystallization ages from 204 to 236 Ma. The youngest and most coherent population (n=52) has a weighted mean age of 221 ± 2 Ma with an MSWD of 1 (Figure 34, Appendix B).

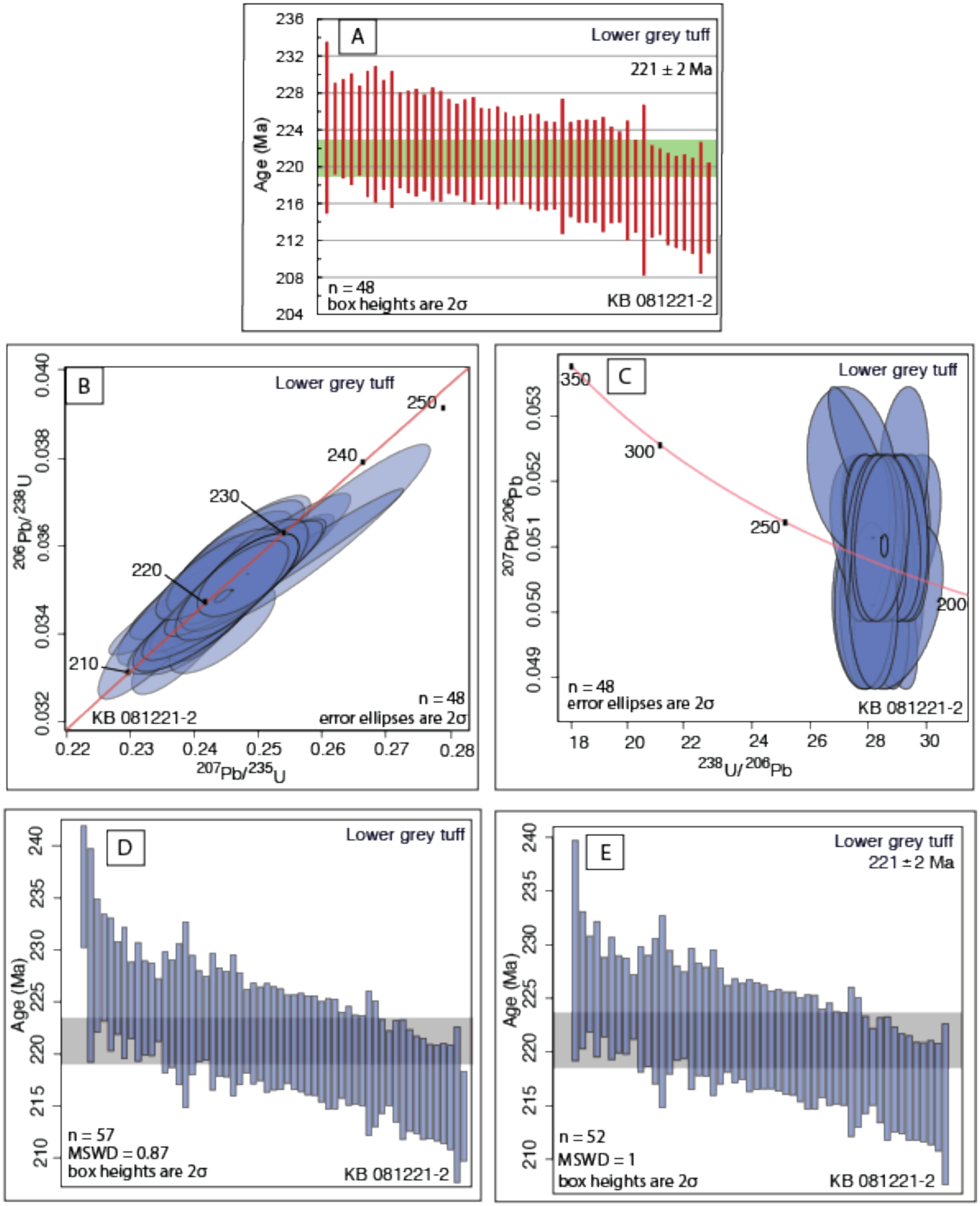

Figure 34: Zircon U-Pb data for lower grey lithic tuff in Agnew Meadows (Sample KB 081221-2). A) TuffZirc age using Isoplot, B) Wetherill concordia diagram, C) Tera-Wasserburg concordia diagram, D) weighted average for all crystals, and E) weighted average age for the most coherent population of zircon crystals. TuffZirc age using Isoplot and IsoplotR ages are in agreement and indicate a crystallization age for the zircon crystals in this unit of 221 ± 2 Ma.

The upper grey lithic tuff (KB 081121-1), which overlies the pumice conglomerate of Agnew Meadows (Figs. 2, 5), yielded 75 concordant zircon grains with a crystallization age range from 209 to 234 Ma. The youngest and most coherent population (n=43) has a weighted mean age of 219 ± 2 Ma and an MSWD of 1 (Figure 35, Appendix B).

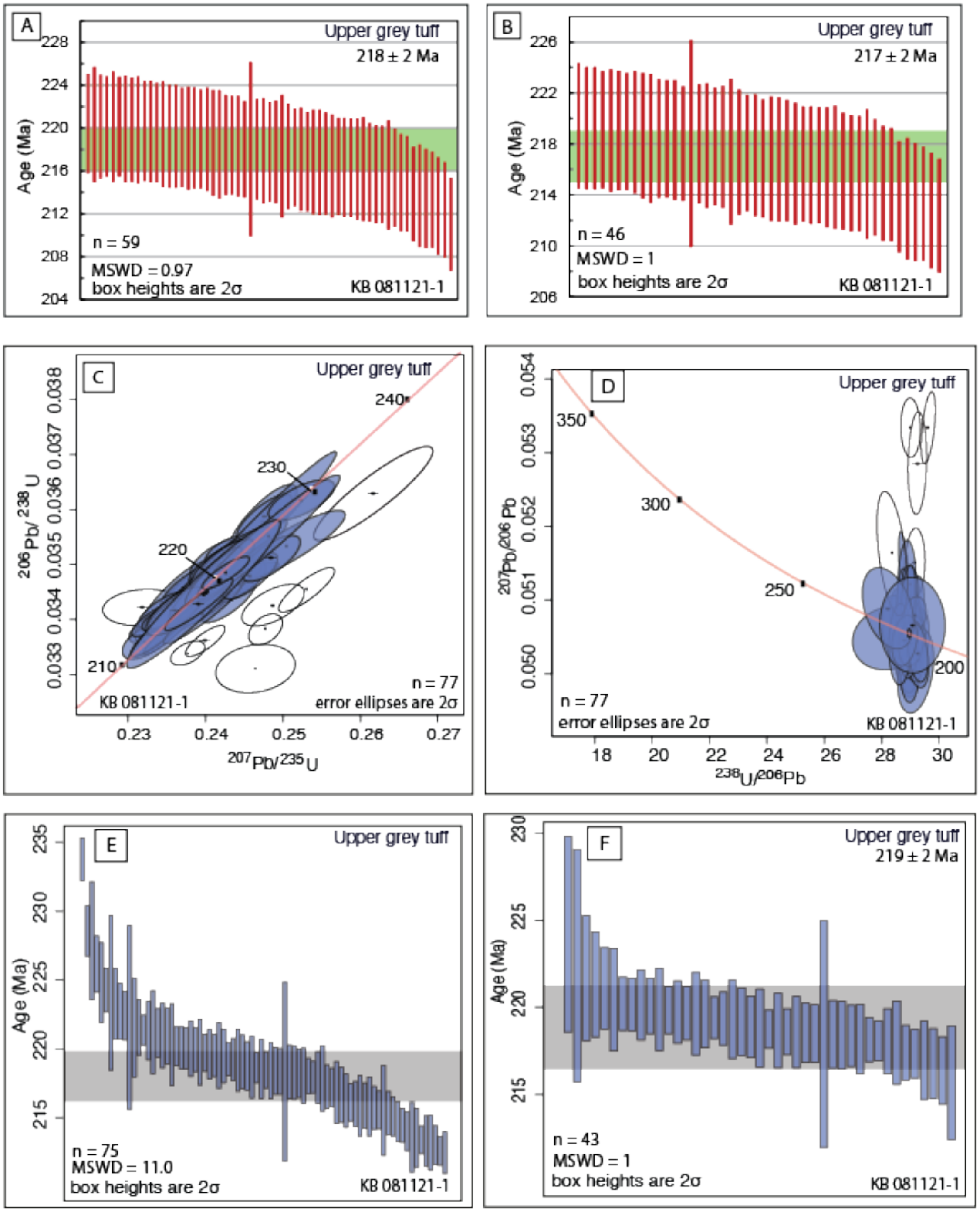

Figure 35: Zircon U-Pb age data for upper grey lithic tuff in Agnew Meadows (KB 081121-1). A) and B) ages using TuffZirc, which returns an age of 217 ± 2 Ma using the most coherent group of zircon crystals shown in B). C) Wetherill concordia, D) Tera-Wasserburg concordia, E) mean standard ages for all zircon crystals, and F) mean standard ages for the most coherent population of zircon crystals, which yields a mean standard age of 219 ± 2 Ma. C-F created using IsoplotR and closed symbols indicate data were included in age calculations, while open symbols indicate data excluded from calculations due to discordance.

5.2 ROCKS IN RED AND WHITE SPUR, MOUNT MORRISON PENDANT

The tuff of Skelton Lake at its namesake in the Mount Morrison pendant is reported by Barth et al. (2018) as 217 ± 2 Ma. A unit at Red and White Spur farther south in the pendant (Figs. 4, 6) was interpreted by Field (2018) to be similar in composition and stratigraphic position to the tuff of Skelton Lake at Skelton Lake. Zircon crystal U-Pb analysis for rocks in this unit at Red and White Spur (KB 081521-1) yielded 52 zircon crystals with a range crystallization ages from 210 to 236 Ma. The most coherent group of zircon crystals from this sample (n=38), with an MSWD of 1, returns a weighted mean age of 220 ± 2 Ma (Figure 36, Appendix B). This is within error of the ages of the tuff of Skelton Lake at Skelton Lake, the tuff of Agnew Meadows, and the tuff of San Joaquin Mountain.

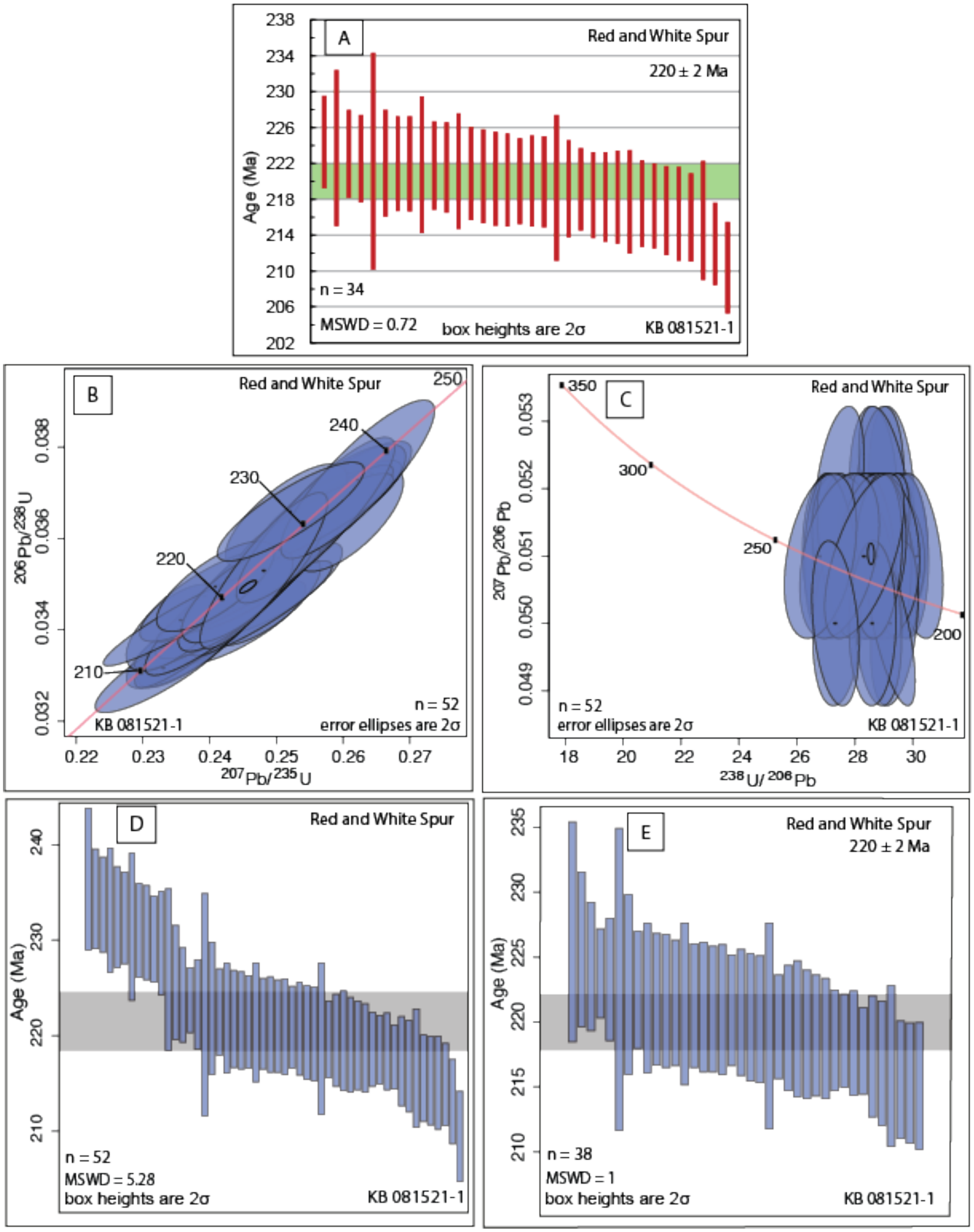

B: $^{206}Pb/^{238}U$ (y-axis); $^{207}Pb/^{235}U$ (x-axis)

C: $^{207}Pb/^{206}Pb$ (y-axis); $^{238}U/^{206}Pb$ (x-axis)

Figure 36: Zircon crystal U-Pb age analyses from the coarse lithic-rich facies at Red and White Spur (KB 081521-1) in the Mount Morrison pendant. A) TuffZirc weighted mean age for the most coherent group of zircon crystals, B) Wetherill concordia, C) Tera-Wasserburg concordia, D) age spectrum for all zircon crystals, and E) age spectrum for the most coherent group of zircon crystals, which yields a weighted mean age of 220 ± 2 Ma (MSWD = 1), in agreement with the TuffZirc age (220 ± 2 Ma) determined using Isoplot (A). B)-E) created using IsoplotR.

Summary of zircon crystallization ages by unit and location:

	LOCATIONS		
AGE (± 2 Ma)	**AGNEW MEADOWS**	**SKELTON LAKE**	**RED AND WHITE SPUR**
218-217	Tuff of San Joaquin Mtn Upper grey lithic tuff	Tuff of Skelton Lake	
221-220	Tuff of Agnew Meadows Lower grey lithic tuff		Lithic-rich facies

6. GEOCHEMISTRY

Whole-rock geochemical analysis provides insights into magmatic conditions and tectonic settings during early volcanic arc genesis and later arc magmatism. Fifteen samples were collected and analyzed for whole-rock geochemistry: ten samples from the volcaniclastic rocks in the Agnew Meadows area (Figs. 2, 5; Table A; Appendix C), two samples from the tuff of Skelton Lake in the Skelton Lake area (Fig. 5, 6; Table A; Appendix C), and three samples from the volcaniclastic rocks in the Red and White Spur area (Figs. 3, 4, 7; Table A; Appendix C). Owing to laboratory issues, whole-rock trace element data are not yet available for these samples. Zircon from three additional samples were analyzed for trace element geochemical data to supplement these whole-rock data and constrain relative crustal thickness and tectonomagmatic setting (Figs. 3, 5, 7; Table A; Appendix B). Zircon trace element data provide the basis for an interpretation of the tectonic and magmatic processes of the young volcanic arc during Triassic time.

6.1 WHOLE-ROCK GEOCHEMISTRY

6.1.1 Major Element Geochemistry

Total alkali (Na_2O + K_2O) vs silica (TAS) diagrams allow easy discrimination of volcanic rock composition (Le Bas et al., 1986). All rocks in this study area have a narrow range of SiO_2 weight (wt.) % (63-78), with most above 70 wt. % SiO_2. Widespread sericite, epidote, and mica mineralization indicates the samples were altered by fluid-rock interaction caused by regional metamorphism, metasomatism, and/or hydrothermal activity, resulting in abnormally high concentrations of potassium, calcium, and phosphorous. Fluid-rock interactions may have been the mechanism for SiO_2 mobilization and/or high alkali concentrations, making these high-silica rhyolite (Barth et al., 2018). The rocks in this area, with the exception of one clast from the tuff of Skelton Lake, have a subalkaline composition (Fig. 37).

The eight volcaniclastic rock samples from the Agnew Meadows area display an SiO_2 range between 64 and 78 wt. % and from 5.5 to 8.3 wt. % total alkali (Fig. 37). Sample KB 080921-2 is a pumice clast from the pumice conglomerate and has the highest SiO_2 value of 78 wt. % and a total alkali value of 7.0 wt. %, while the matrix in the pumice conglomerate has 70 wt. % SiO_2 and 6.7 wt. % total alkali. The pumice clast is classified as rhyolite and the pumice breccia matrix is on the line between dacite and rhyolite (Fig. 37). Sample KB 080521-1 from the lower grey lithic tuff is a grey pumice clast that has the lowest silica content in the area at 64 wt. % SiO_2 and has 6.6 wt. % total alkali, classifying it as dacite. All other samples in the Agnew Meadows area, including the upper and lower grey lithic tuffs and the tuff of San Joaquin Mountain, are rhyolites and display a SiO_2 range between 72 and 78 wt. % and a total alkali range between 5.5 and 8.1 wt. % (Fig. 37, Appendix D). Additional data from Barth et al. (2018) are included for the tuff of Agnew Meadows and the tuff of San Joaquin Mountain to compare to the data from this study and to investigate petrogenetic similarity. These two units are the top and bottom of the sequence, respectively, and so provide additional data in the area for comparison. These data are all similar to the values obtained in this study.

Two samples were collected from the tuff of Skelton Lake in the Skelton Lake area: one of the volcaniclastic matrix (KB 080621-1) and one of a mafic volcanic clast (KB 080621-2) in the tuff. The volcaniclastic matrix is rhyolitic with 75 wt. % SiO_2 and 7.48 wt. % total alkali, and the clast has 63 wt. % SiO_2 and 9.4 wt. % total alkali and is trachydacite (Fig. 37). Additional data for the tuff are included from Barth et al. (2018) for comparison and have similar SiO_2 wt. % (71-76) with slightly lower total alkali values (3.4-6.6 wt. %) and are all rhyolite (Fig. 37).

Three samples were collected in the Red and White Spur area: the coarse-grained lithic-rich facies (KB 081521-1), the fine-grained lithic-rich facies (KB 081521-2), and the fine-grained tuff facies (KB 081521-3). These three samples range from 73 to 77 wt. % SiO_2 and from 3.9 to 6.8 wt. % total alkali and are all rhyolite (Fig. 37).

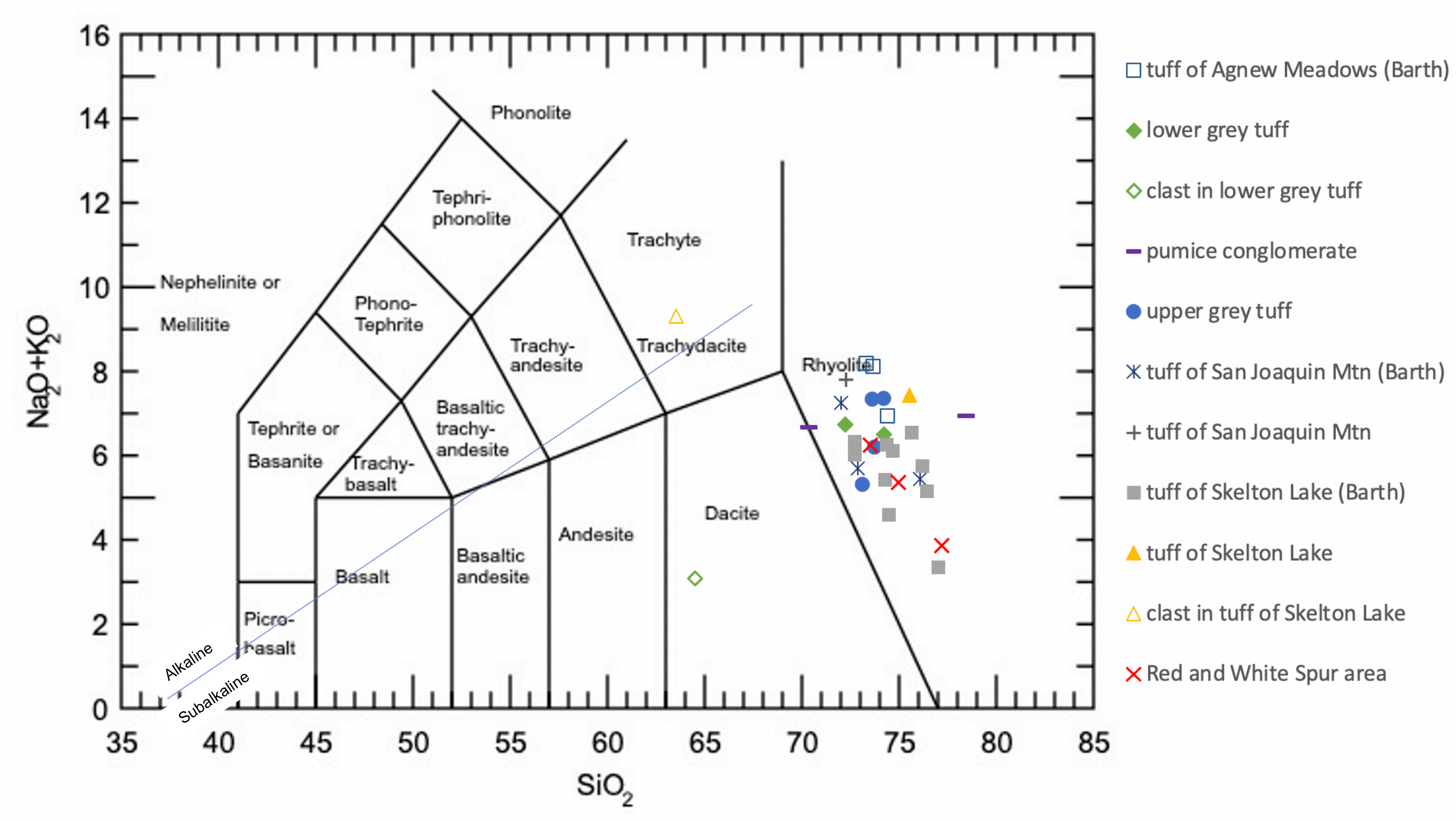

Figure 37: Total-alkali silica diagram (modified from Le Bas et al., 1986) for rocks from the Agnew Meadows area and the Skelton Lake area from this study and from Barth et al. (2018), and the Red and White Spur area from this study. The blue line separates alkaline (above) and sub-alkaline (below) compositions.

Harker diagrams (Fig. 38) plot weight % SiO_2 against various major oxides and are used to understand and interpret a variety of magma systems and processes including fractional crystallization, partial melting, crustal contamination, and magma mixing. These diagrams show graphical trends of the evolution of magma systems and multiple batches of geochemically similar magma from a system. Crystallization processes produce a lower Mg # [(Mg/(Mg + Fe)*100] in derivative liquids compared to parental sources (Kelemen et al., 2014). Primitive magmas have Mg #s >60 while evolved magmas, presumably derived from the parental primitive melt, have Mg#'s < 60 (Kelemen et al., 2014). Data are included from Barth et al. (2018) for the tuff of San Joaquin Mountain, the tuff of Skelton Lake, and the tuff of Agnew Meadows for comparison with data from this study and to expand the scope of units included to assess the petrogenetic link. Evolved arc magmas can form by the fractionation of primitive basalt and andesite, resulting in relatively high silica and alkali contents (Kelemen et al., 2014). The Mg# values for the rocks in this study range from 11.29 to 38.74 (Fig. 39), suggesting they may have been the result of fractionation of a relatively primitive basaltic to andesitic arc magma.

If the volcanic rocks from the two pendants in this study are associated with a common magma system, they should show a negative correlation between silica and aluminum, iron, calcium, manganese, and magnesium, and a positive correlation for sodium and potassium at silica values above 60 wt % (Harker, 1909). Phosphorous should show a negative correlation. No trends are evident in the data presented here for calcium, sodium, potassium, or phosphorous (Figs. 38), while moderate negative correlation trends are evident in titanium, aluminum, iron, manganese, and magnesium (Fig. 38). Sericite and epidote mineralization were likely the result of metamorphism and/or hydrothermal activity and increased the concentrations of potassium, aluminum, calcium, and sodium in these rocks.

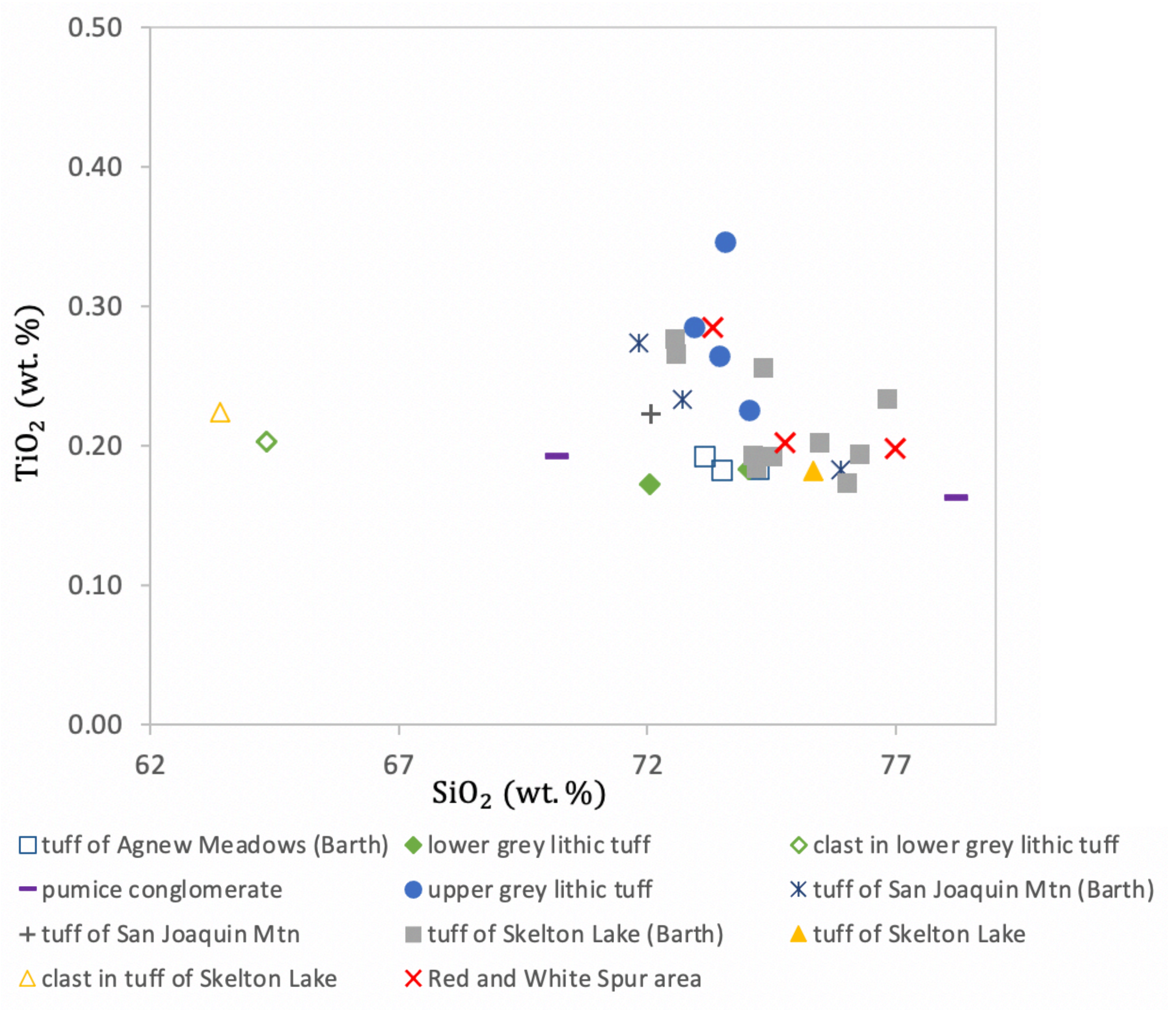

Figure 38: Harker variation diagrams for rocks from Agnew Meadows, Skelton Lake, and Red and White Spur area. Data from Barth et al. (2018) are included for comparison and additional detail. A very weak negative trend is evident in the titanium plot.

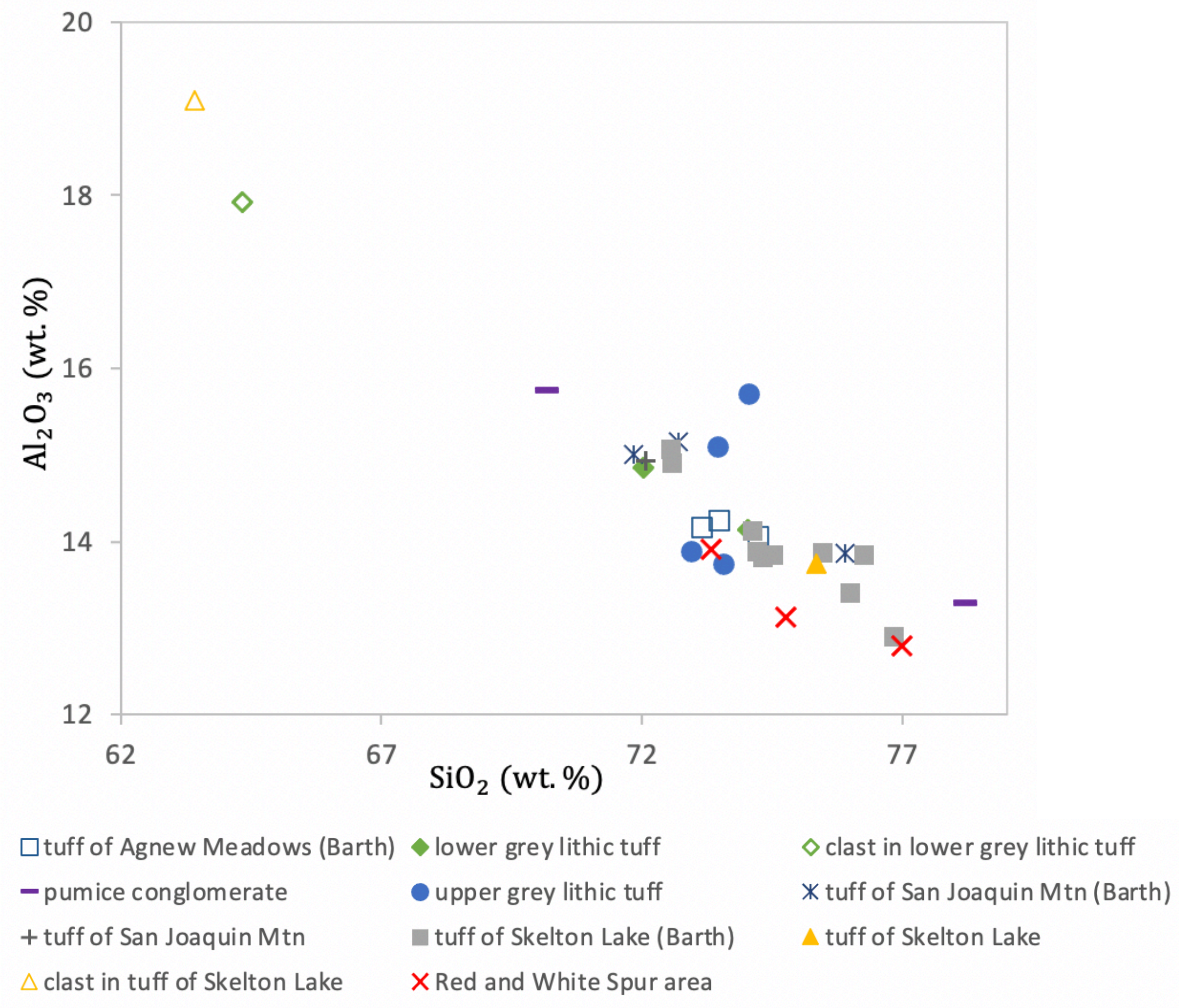

Figure 38, cont.: Harker variation diagram for Al_2O_3. A moderate negative trend is evident in this plot.

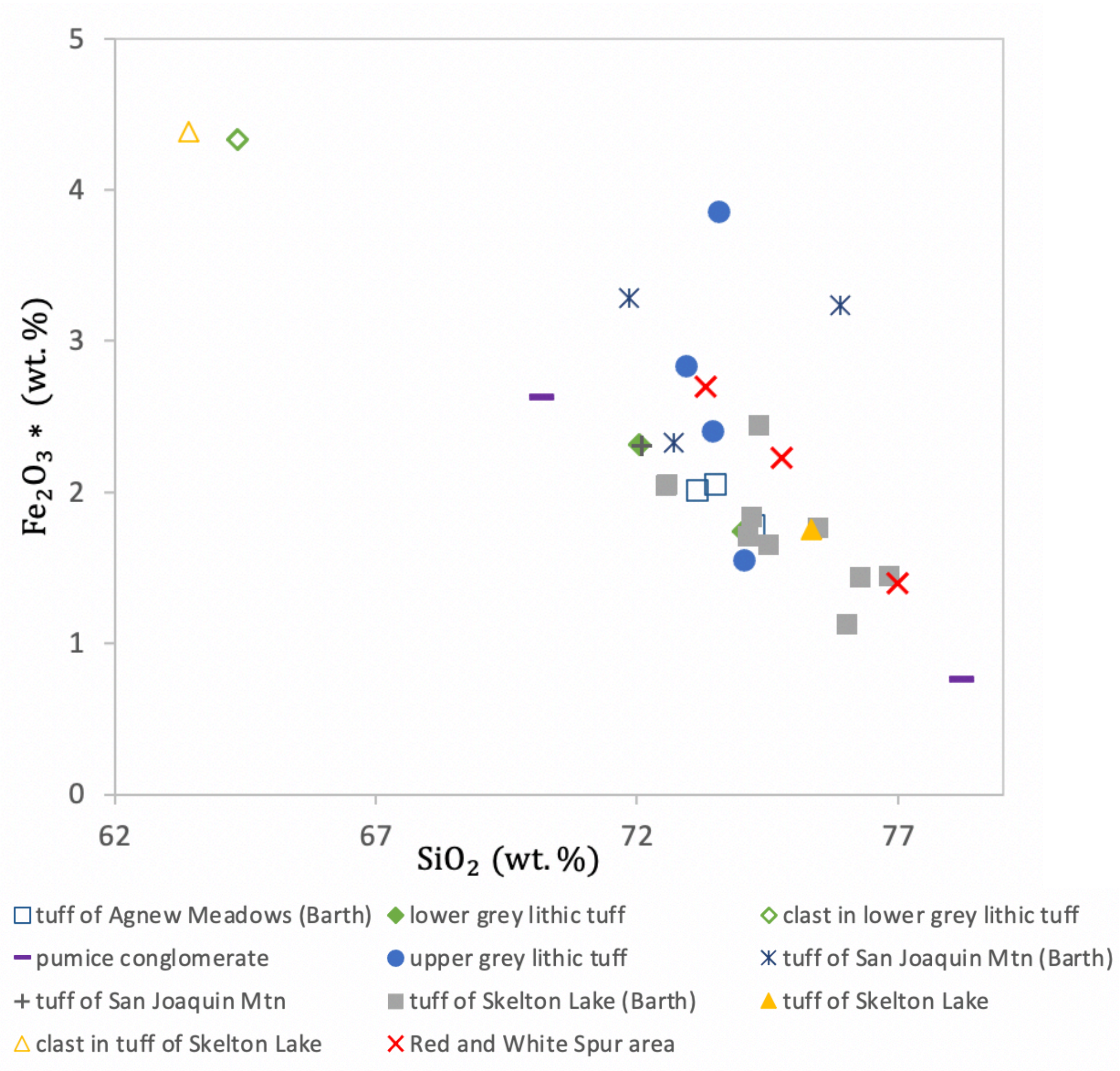

Figure 38, cont: Harker variation diagram for Fe_2O_3. Note a strong negative correlation in this plot, as is expected for regionally similar petrogenesis.

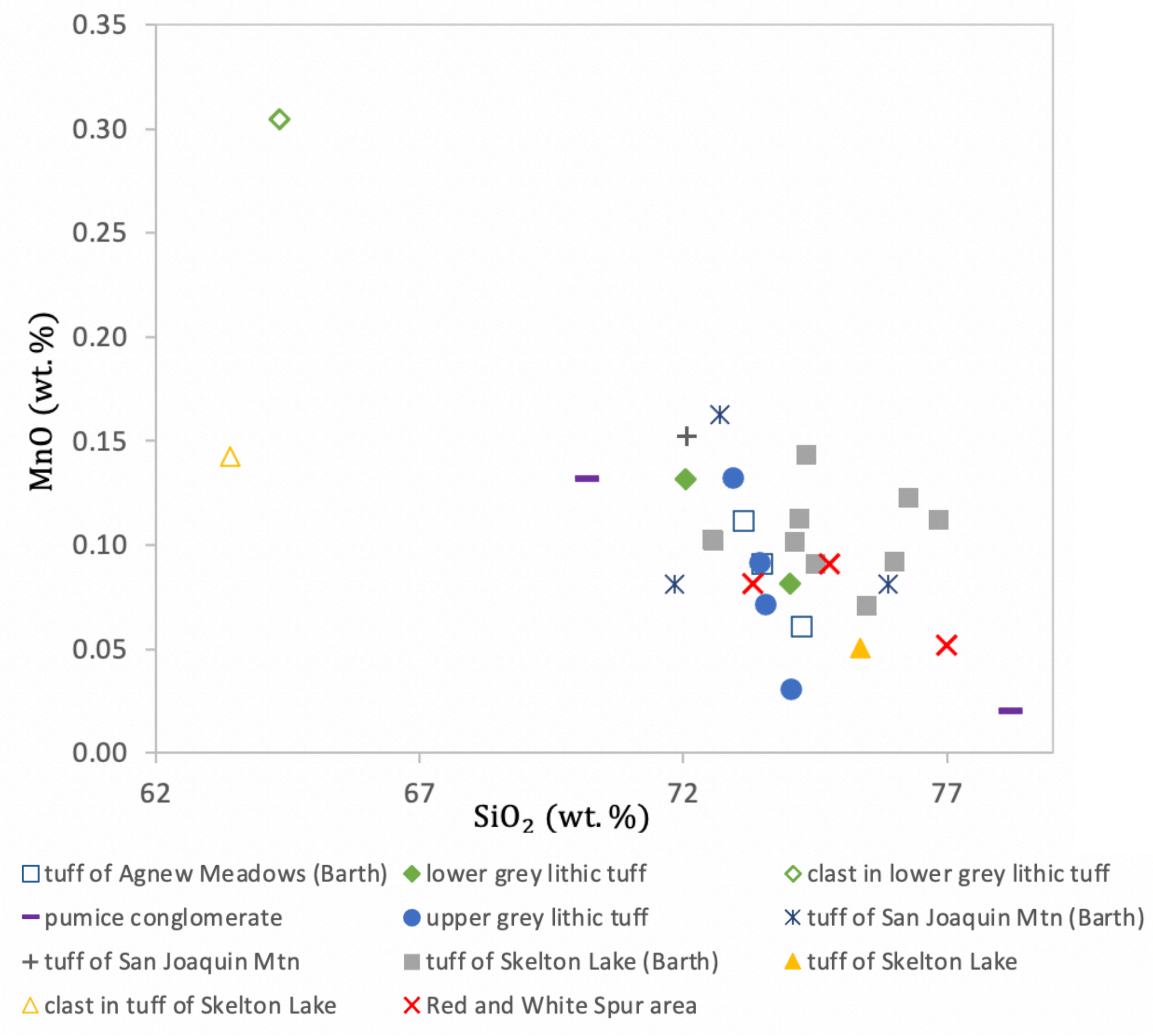

Figure 38, cont.: Harker variation diagram for MnO. Only a slight negative trend is apparent in this plot, as expected for regionally similar petrogenesis.

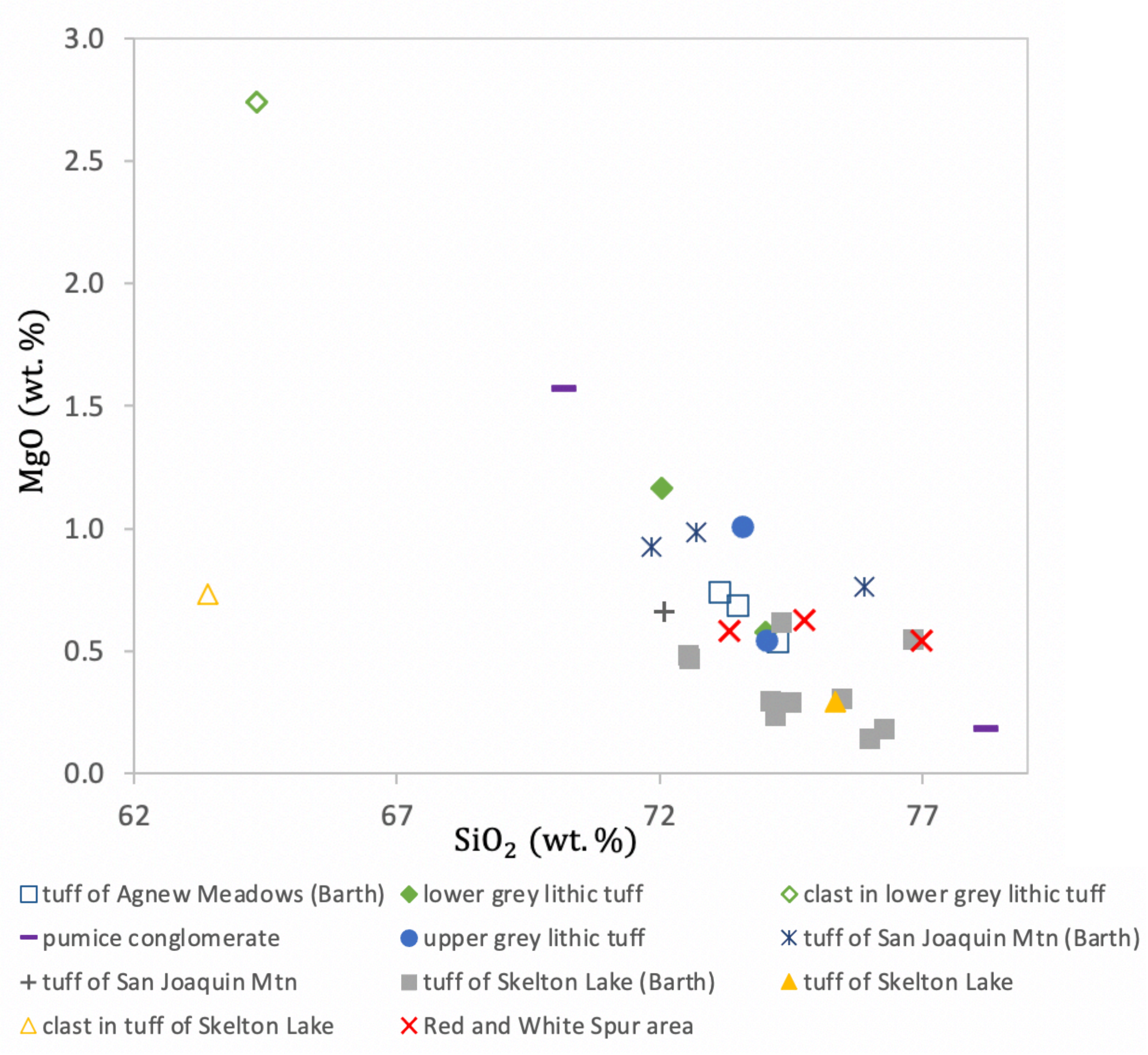

Figure 38, cont.: Harker variation diagram for MgO. A negative trend is evident in these data, as expected for regionally similar petrogenesis.

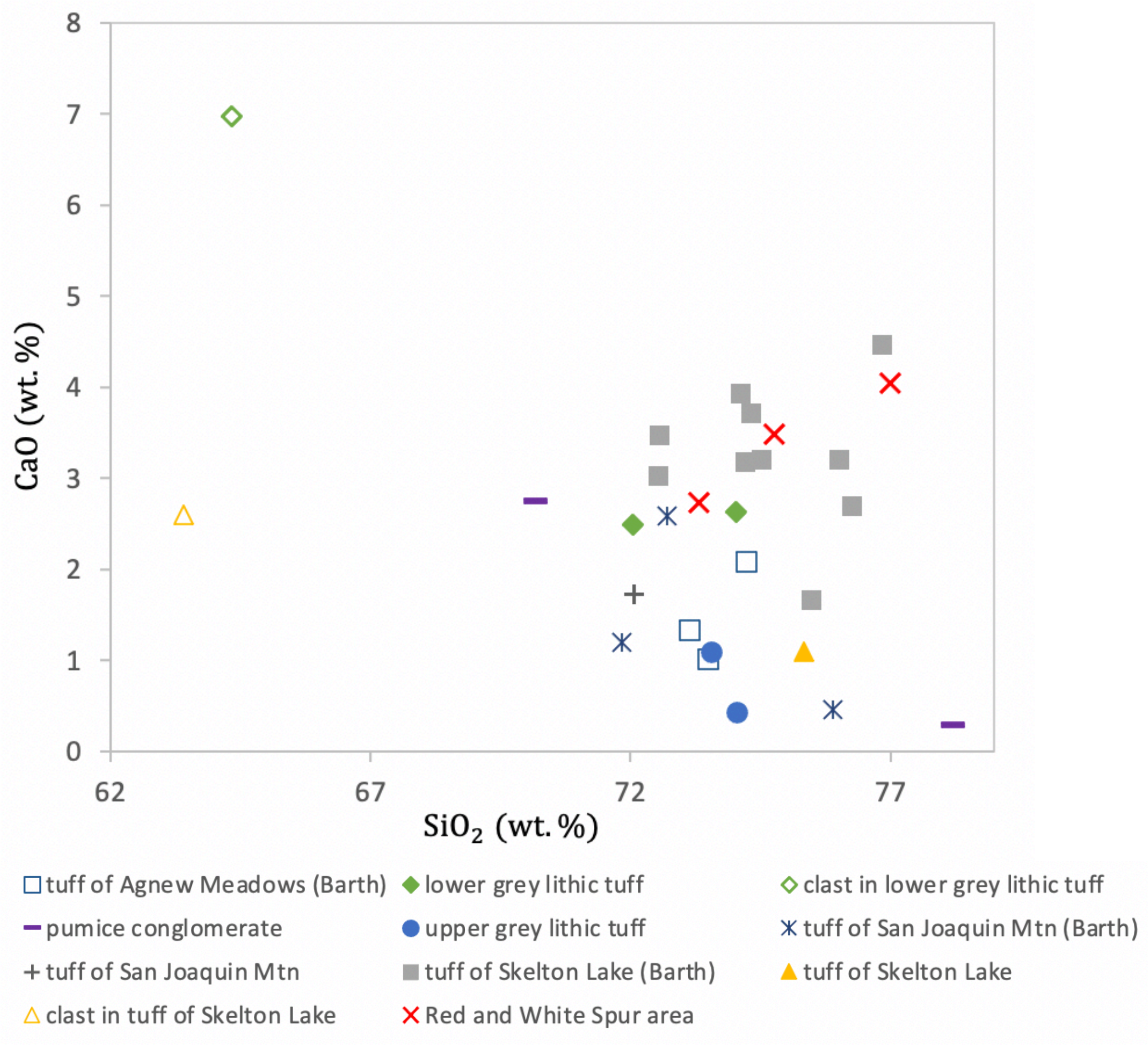

Figure 38, cont.: Harker variation diagram for CaO. A slight positive trend is evident in the data from Red and White Spur samples and the tuff of Skelton Lake, but not in any other areas.

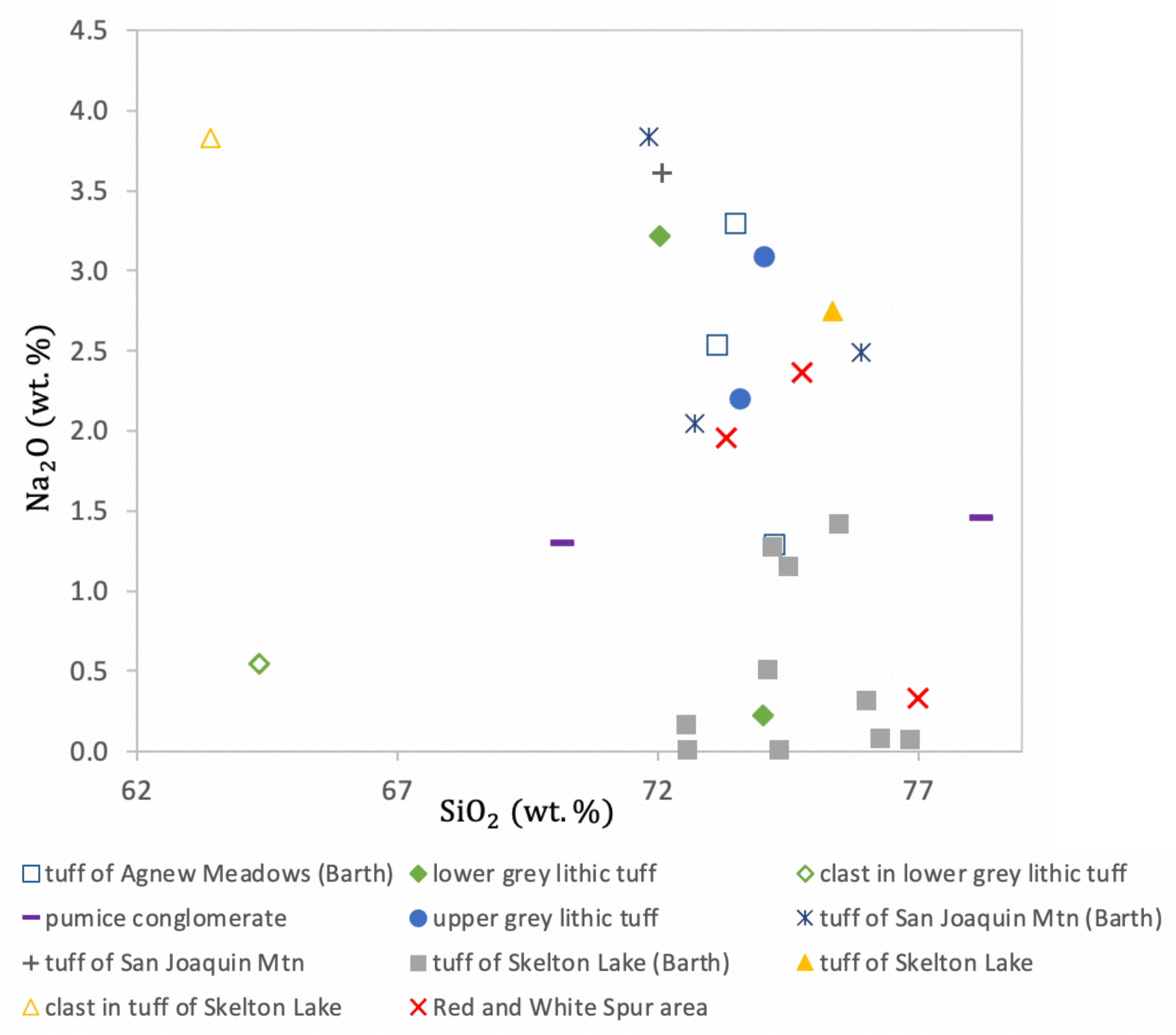

Figure 38, cont.: Harker variation diagram for Na_2O. There is no correlation, which would be expected for regionally similar petrogenesis.

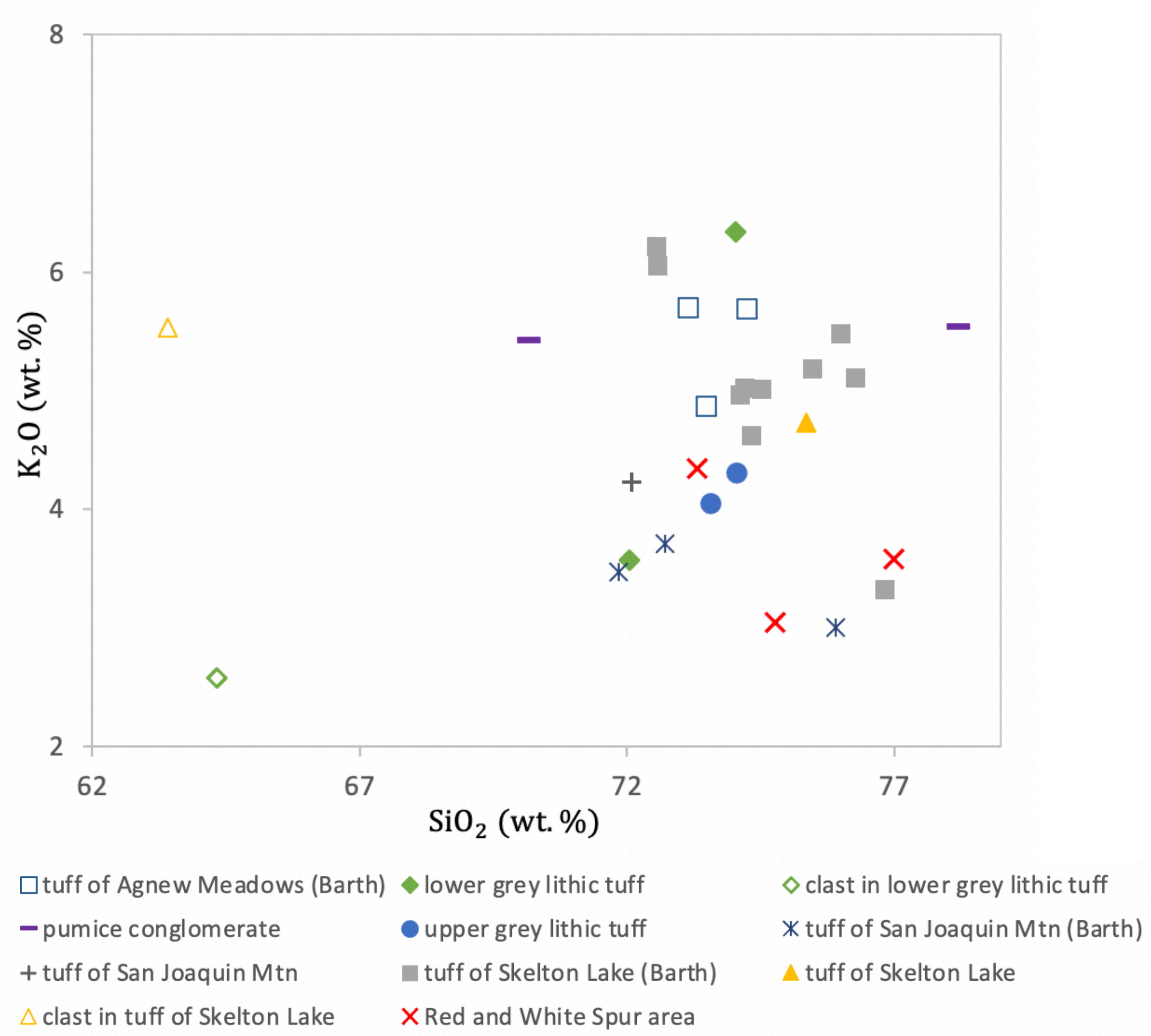

Figure 38, cont.: Harker variation diagram for K_2O. There is no obvious positive correlation, as would be expected for regional petrogenetic similarity. The scatter could be due to metamorphism and/or hydrothermal activity causing increased fluid-rock interaction and mineral alteration.

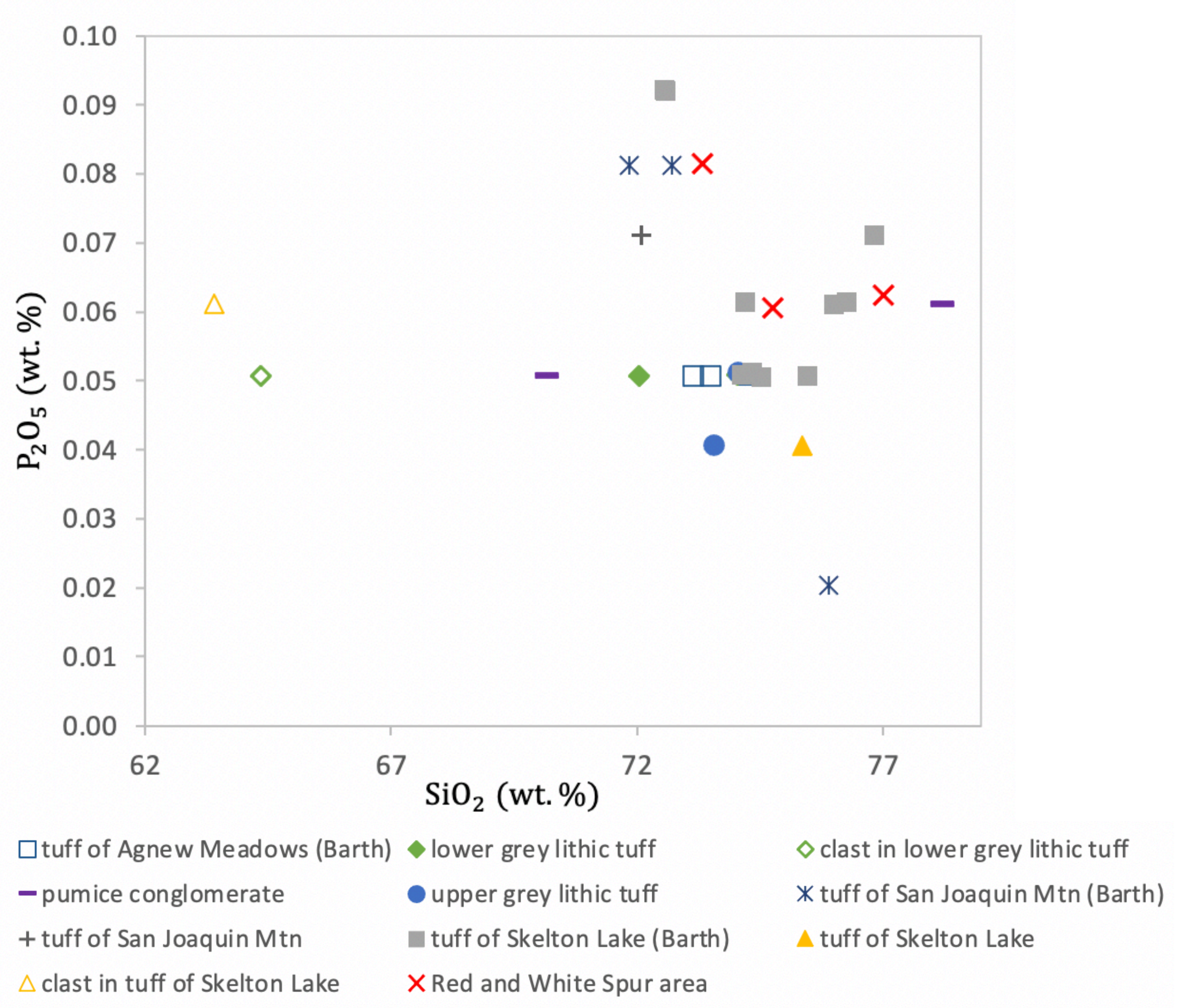

Figure 38, cont.: Harker variation diagram for P_2O_5. The data do not show the expected slight negative trend, as would be expected for petrogenetic similarity. The scatter could be due to metamorphism and/or hydrothermal activity. The scatter could be due to metamorphism and/or hydrothermal activity causing increased fluid-rock interaction and mineral alteration.

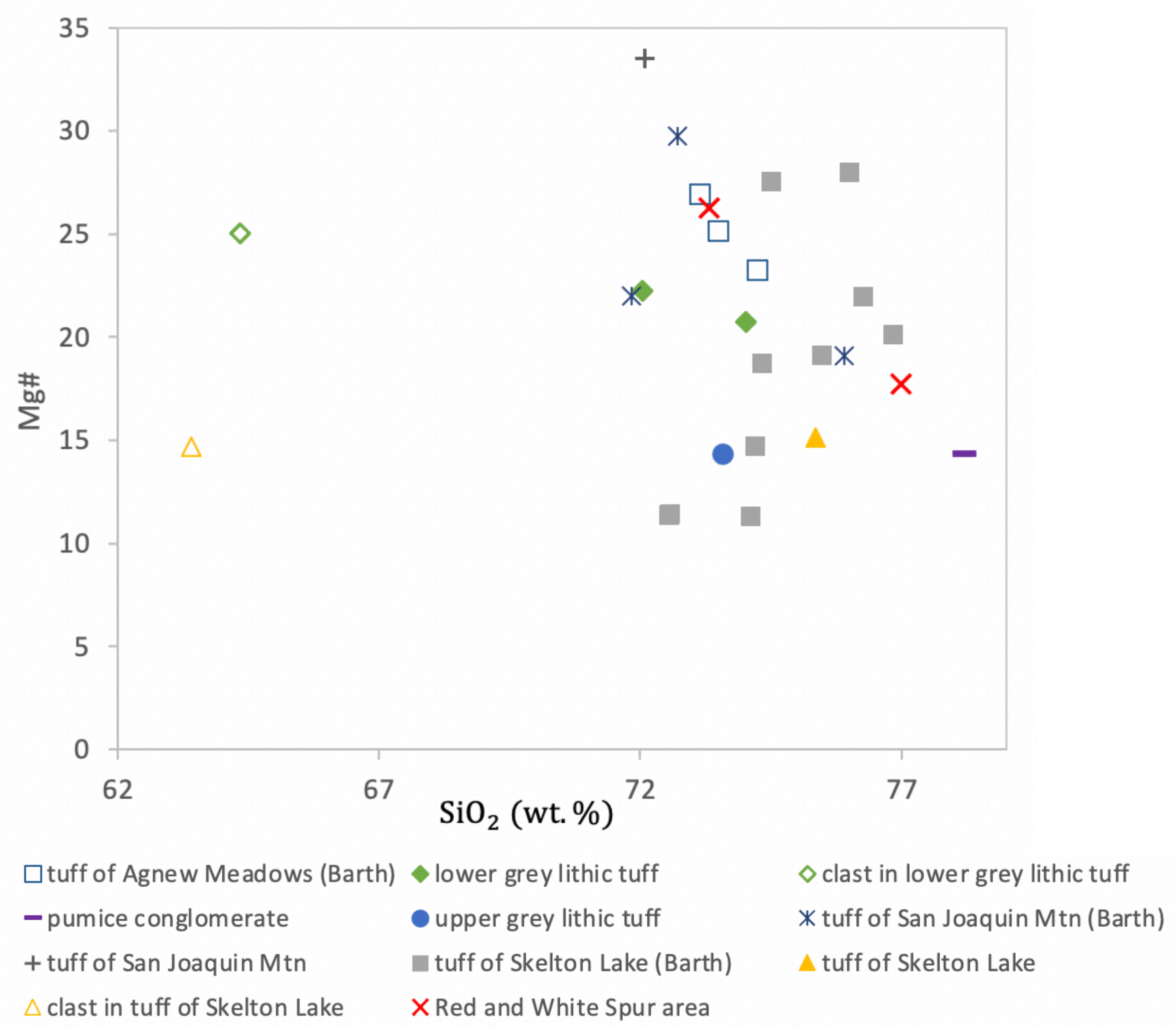

Figure 39: Variation diagram for Mg# as a function of silica concentration. The Mg# is less than 35 for all rocks, and the data do not show any trends. Mg#'s less than 40 are suggestive of a magma evolved from a more primitive andesitic parental melt (Kelemen et al., 2014).

6.2 ZIRCON GEOCHEMISTRY

Trace element geochemical analysis of zircon from magmatic rocks in conjunction with whole-rock geochemistry can offer insight into tectonomagmatic setting and magmatic source rocks. Zircon resists recrystallization during hydrothermal alteration and low-grade metamorphism and contains zirconium, a highly incompatible and immobile trace element. For this reason, trace element analyses of zircon crystals in altered host rocks can provide data that can be used to interpret relative crustal thickness associated with arc-magma systems and tectonomagmatic setting. U/Yb and Th/Yb vs Hf concentration plots for zircon from arc magmas can be divided into low, medium, and high fields, which are correlated with crustal type and upper-crustal contamination (Grimes et al., 2015). Magma suites from continental crustal settings are characterized by zircon with U/Yb concentrations > ~0.1 to 0.2 and Th/Yb greater than ~0.1 (Grimes et al., 2015; Barth et al., 2017; Barth et al., 2018). Grimes et al. (2015) identified a variety of relations between trace elements that are different between continental-crustal igneous zircon and mid-ocean-ridge-sourced zircon. Continental arc zircon have U/Yb values between 0.1 and 4, and higher values are due to the greater influence of mature, large-ion-lithophile-enriched crust during formation of the host melts (Grimes et al., 2015). High U/Yb values reflect an enriched mantle source and/or crustal input and, in general, as Hf concentration increases, the U/Yb also increases as a result of melt fractionation (Grimes et al., 2015). Zircon crystallization will exert a dominant control on U, Yb, and Hf chemistry of the remaining melt, fractionating Zr relative to Hf and increasing Hf in later-formed grains (Grimes et al., 2015). Fractionation of zircon is also monitored by decreasing Ti concentration with increasing U/Yb and Hf concentration.

Three samples were analyzed for zircon geochemistry in conjunction with U-Pb geochronology: lower grey lithic tuff (KB 081221-1) and upper grey lithic tuff (KB 081121-1) in the Agnew Meadows area (Fig. 5), and the coarse lithic-rich facies (KB 081521-1) in the Red and White Spur area (Fig. 7). All three samples have high (>0.2) U/Yb (Fig. 40), and high (>0.1) Th/Yb (Fig. 41), suggesting a continental crustal setting. These data are combined with those presented by Barth et al. (2018) to suggest a petrogenetic link between rocks in the Agnew Meadows area, the Skelton Lake area, and the Red and White Spur area.

Zircon crystals with U/Nb ratio greater than 100 are characteristic of a continental magmatic arc source (Fig. 42; Grimes et al., 2015). Grimes et al. (2015) also determined that U (ppm) vs Nb (ppm) can be used to distinguish magmatic arc zircon from the mantle zircon array (Fig. 43). Data from this study and Barth et al. (2018) have U/Nb values well over 10, and the majority are over 100, strongly suggesting a magmatic arc setting. Trace element data for zircon from continental arc and post-collisional tectonomagmatic settings from Grimes et al. (2015) are normalized to mid-ocean ridge-derived zircon values (Fig. 44). The data from the zircon in this study and from Barth et al. (2018) are plotted for comparison and follow similar trends to the continental arc granitoids and post-collisional tectonomagmatic settings investigated by Grimes et al. (2015). The similarity suggests the zircon in rocks in the pendants in the eastern Sierra Nevada crystallized in a continental arc tectonomagmatic setting. These results imply that the three areas are petrogenetically linked. Zircon also partitions Yb relative to U, enriching the remaining melt in U relative to Yb, which is evident in the increase in U/Yb in later-formed grains. Plotting U/Yb as a function of age (Figs. 45, 46) shows a very slight increase in U/Yb with decreasing age, consistent with continuous zircon crystallization. Ti concentration also shows a negative correlation with Hf concentration (Fig. 47), further supporting continued zircon fractionation in the magma system.

Plotting Ti concentration vs Gd/Yb can show the effects of titanite and apatite competing with zircon for rare earth elements (Fig. 8 in Grimes et al., 2015). All zircon from this study and from Barth et al. (2018) are similar and have Gd/Yb values between 0.01 and 0.1 (Fig. 48), indicating similarity in source magma composition. The covariation in these zircons is likely driven by the influence of magma cooling and possibly co-crystallization of titanite and apatite in competition for REE with later-formed zircon.

Zircon preferentially incorporates heavy rare earth elements (HREE) making it sensitive to other cogenetic minerals that incorporate HREEs such as amphibole and garnet (Sundell et al., 2022). Increasing U/Yb indicates light rare earth element (LREE) enrichment compared to HREE, and this increase is suggestive of a relative increase in crustal thickness (Sundell et al., 2022). The relative increase in LREE compared to HREE is evident in the higher U/Yb in the younger zircon crystals analyzed in this study (Figs. 45, 46).

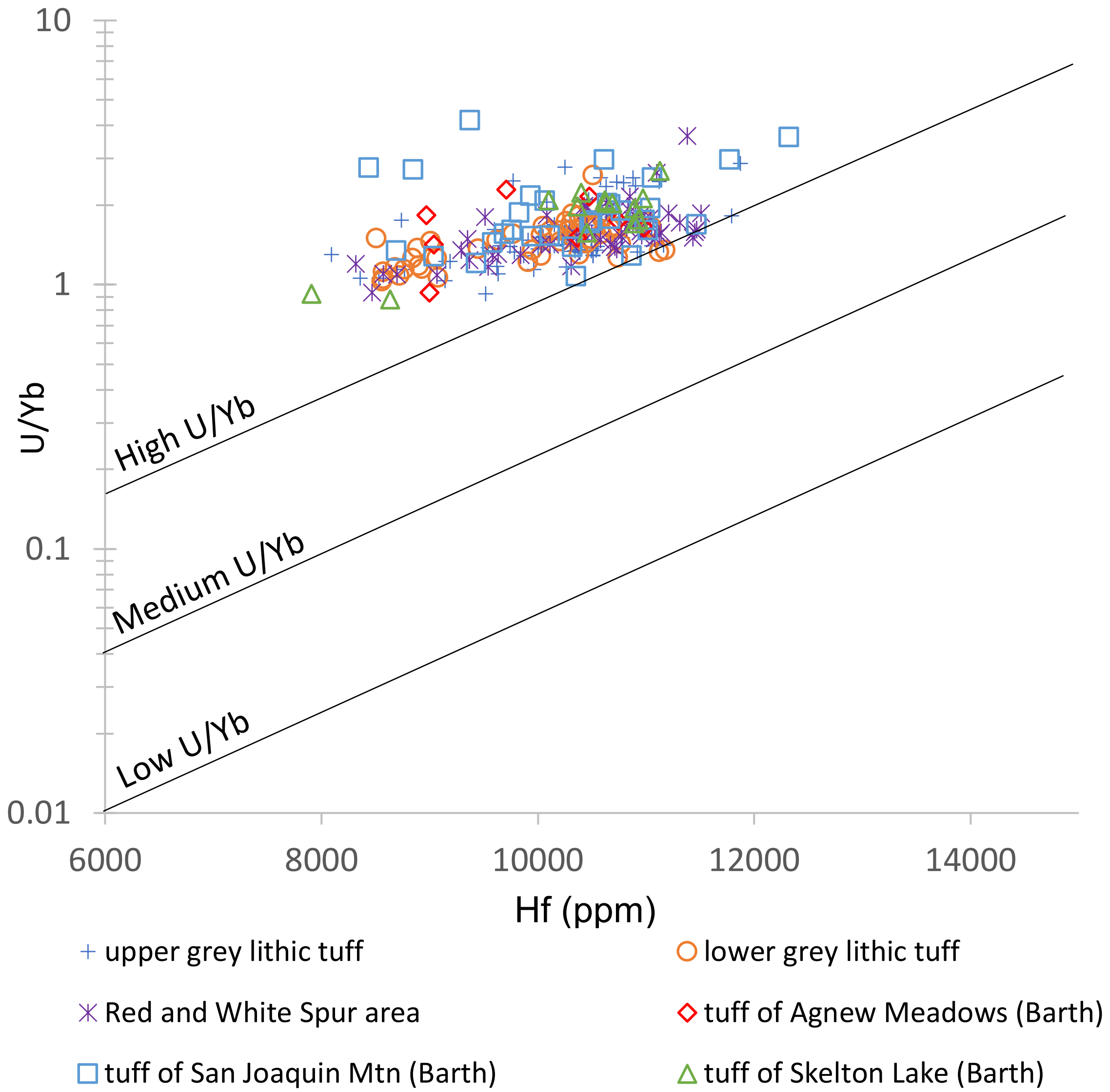

Figure 40: U/Yb vs Hf concentration with fields for high, medium, and low U/Yb (defined by Barth et al., 2017). Zircon from this study and from Barth et al. (2018) are clustered and have high U/Yb, indicating a continental arc source. High U/Yb values suggest a greater influence from mature, LILE-enriched crust during formation of host melts (Grimes et al., 2015).

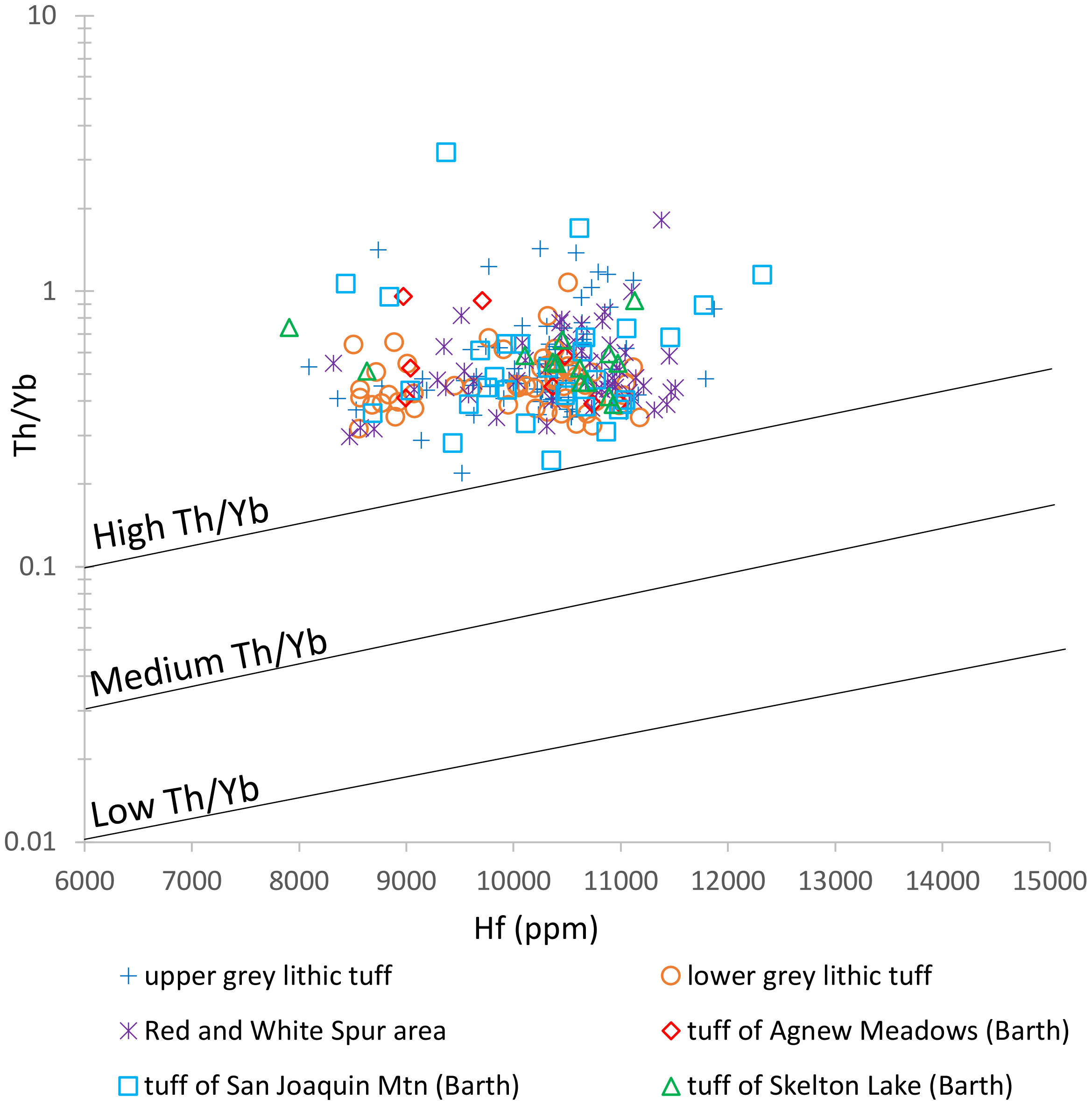

Figure 41: Trace element plot of Th/Yb vs Hf concentration with fields for high, medium, and low Th/Yb, which is correlated with relative crustal thickness defined by Grimes et al. (2015). All zircon from this study and from Barth et al. (2018) are clustered and have high Th/Yb, implying a tectonic setting with a relatively thick crust.

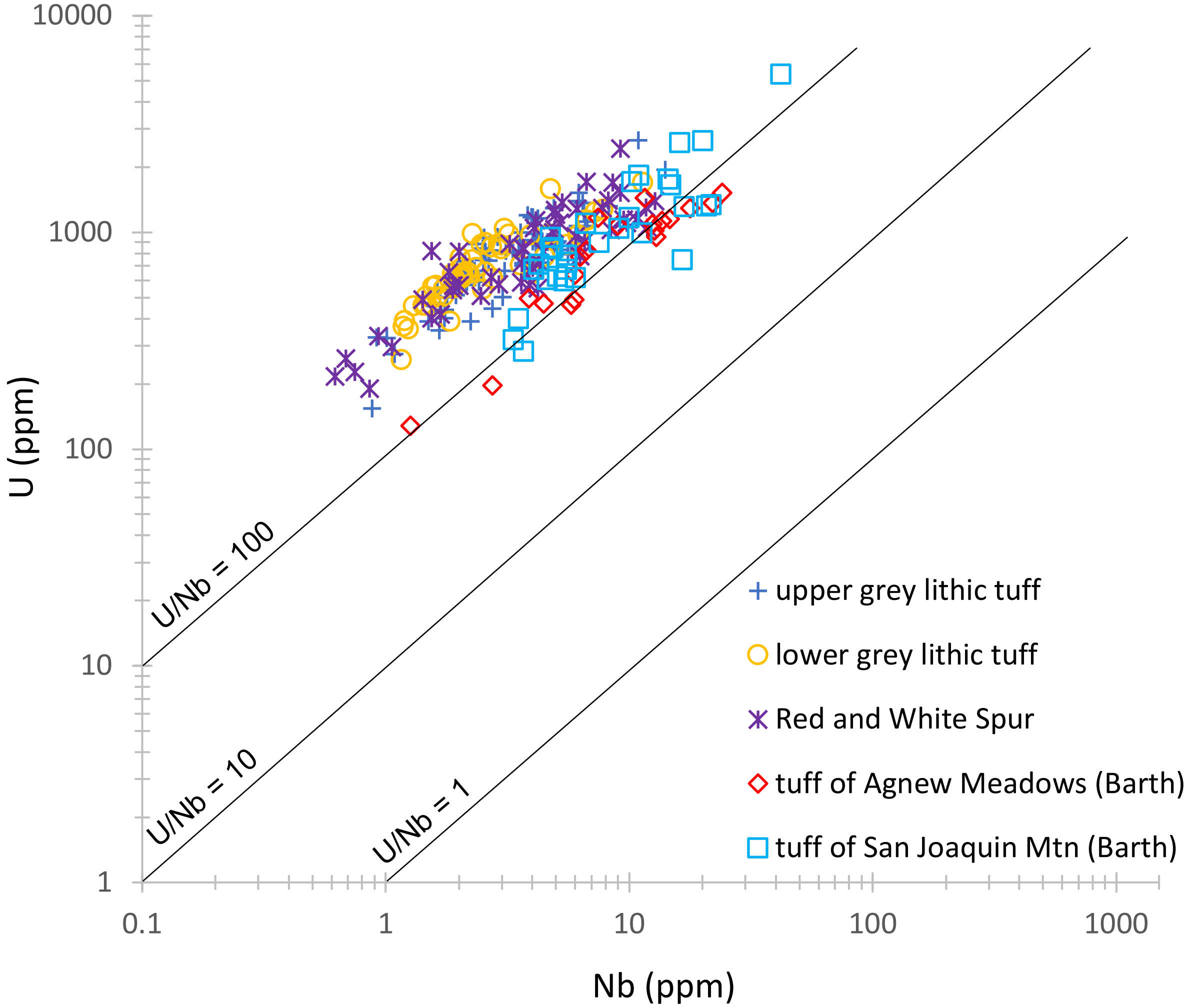

Figure 42: U concentration vs Nb concentration with lines differentiating U/Nb ratios of 1, 10, and 100. All zircon from this study and from Barth et al. (2018) are above a U/Nb ratio of 10, and most are above 100. Grimes et al. (2015) showed that a ratio higher than 100, as is the case for these zircons, is indicative of a continental magmatic arc source.

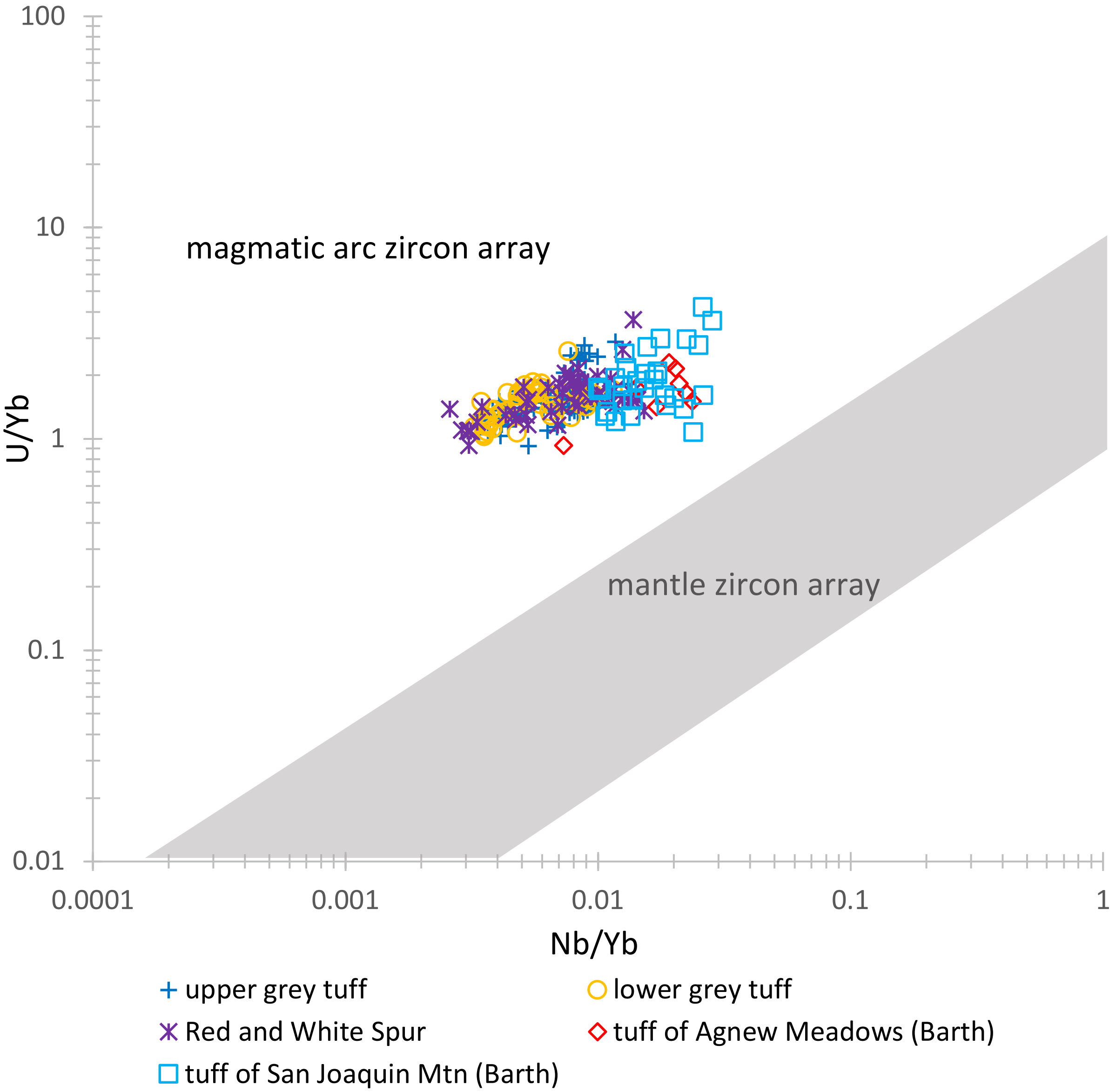

Figure 43: U/Yb versus Nb/Yb. Mantle zircon array and magmatic arc zircon array fields are from Grimes et al. (2015). The data from this study and from Barth et al. (2018) are similar and are all well within the magmatic arc zircon field.

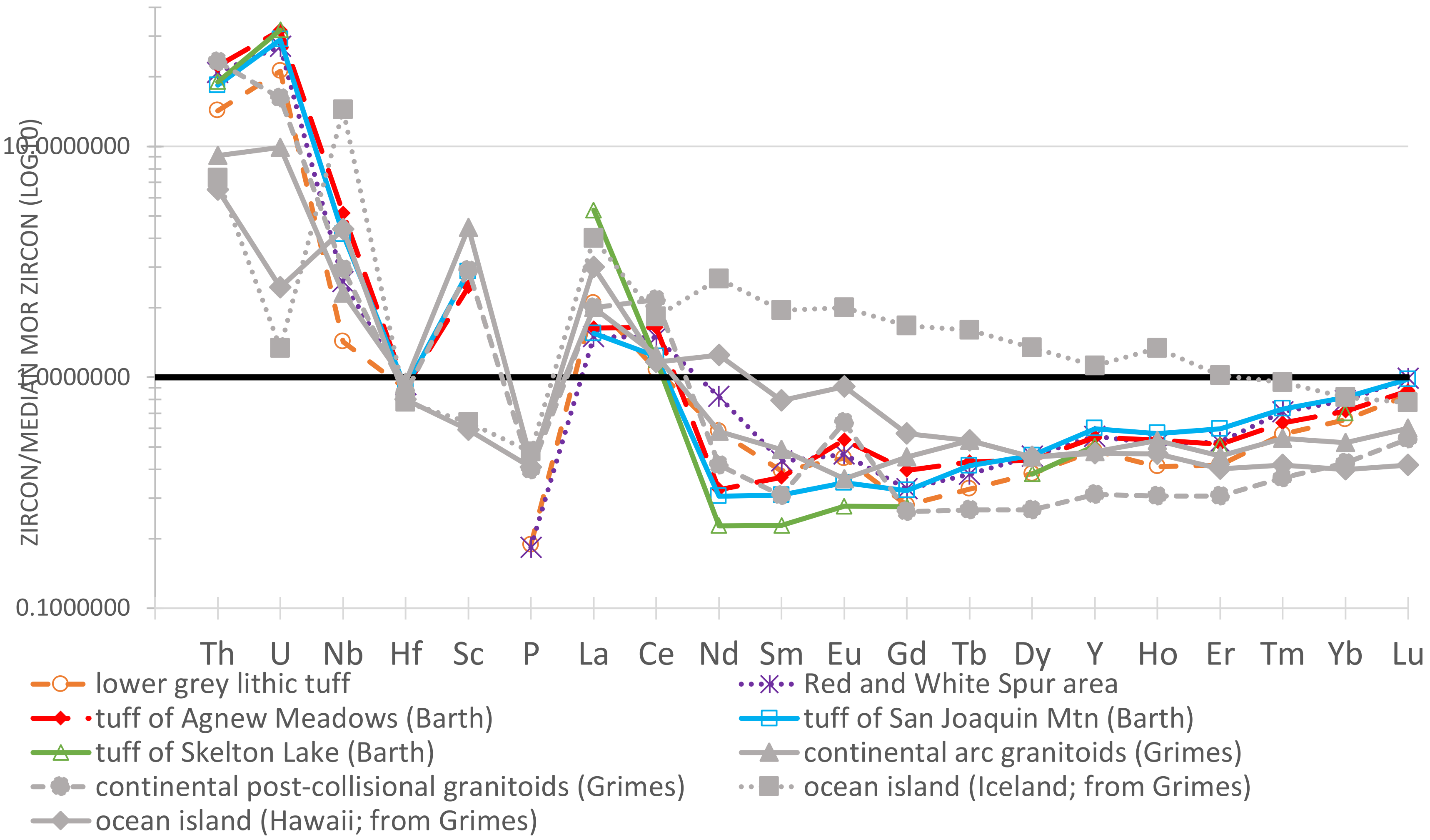

Figure 44: Multi-element variation diagram showing median trace element data from zircon from this study, Barth et al. (2018), and Grimes et al. (2015) for reference, normalized to median MOR-derived zircon (data from Grimes et al., 2015). The data from this study and Barth et al. (2018) follow trends similar to the continental arc granitoids, suggesting a continental magmatic arc setting for the Triassic volcanism in the eastern Sierra Nevada.

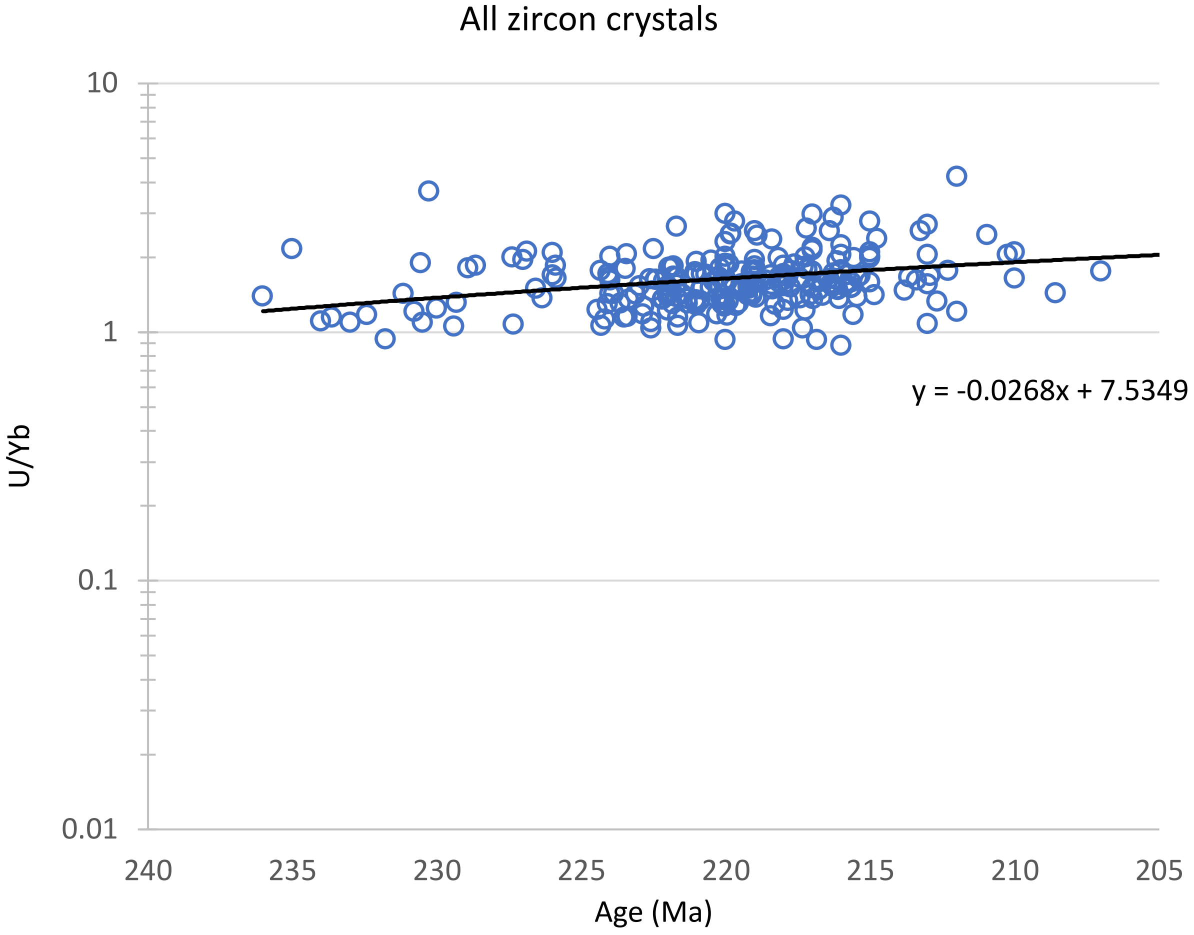

Figure 45: U/Yb as a function of age (Ma) for all individual zircon crystals analyzed in this study. A slight increase in U/Yb with decreasing age of the crystals is evident, consistent with continued crystallization of zircon enriching the remaining melt in U relative to Yb.

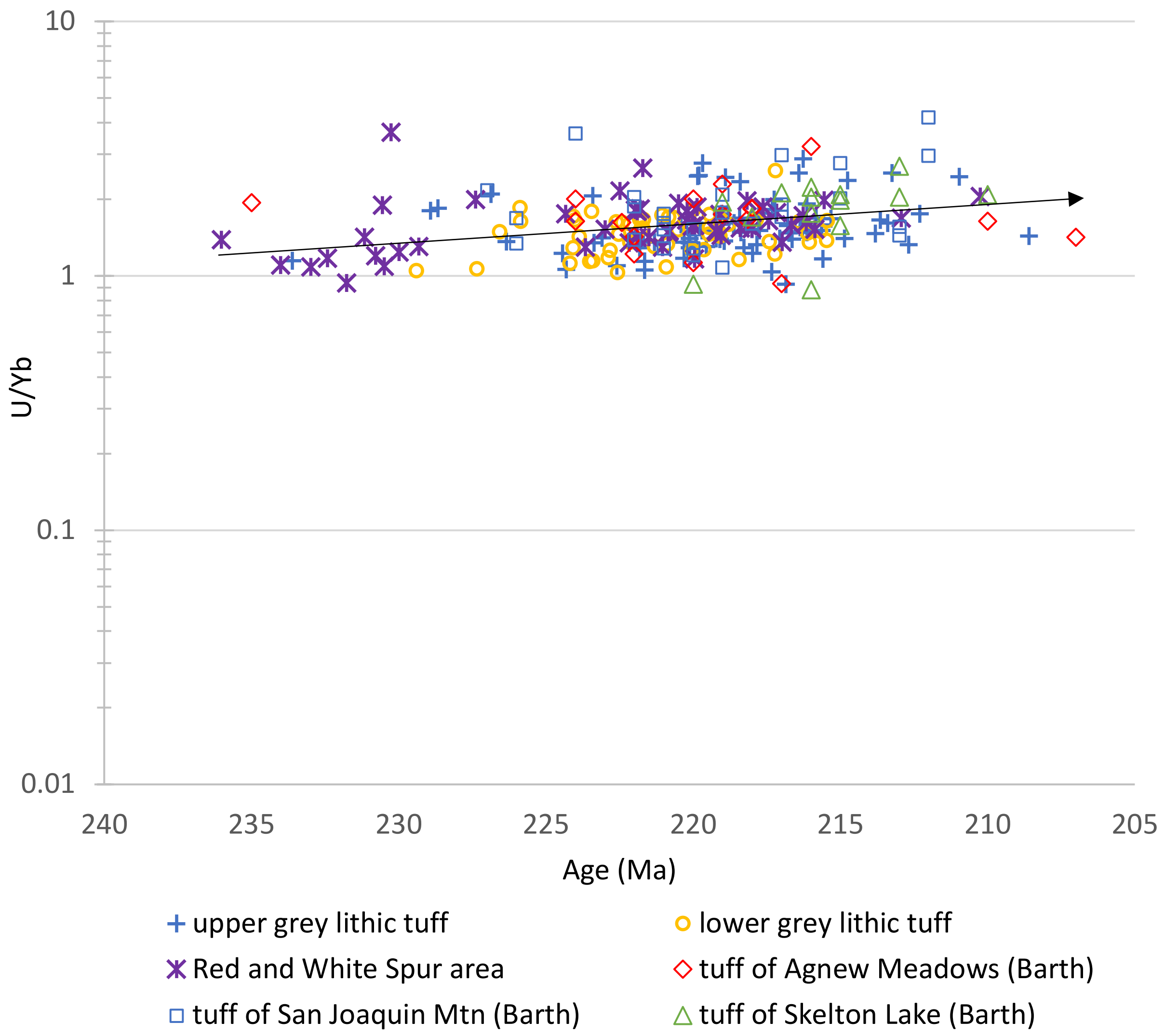

Figure 46: U/Yb as a function of age (Ma) for individual zircon grains separated by rock unit. Variation within each group is evident, but the overall trend of increasing U/Yb with decreasing zircon crystal age is still evident across the time span presented (black arrow).

Figure 47: Hf concentration vs Ti concentration for zircon from this study and from Barth et al. (2018) in related rocks in the Mount Morrison and Ritter Range pendants. Zircon trace element data from all areas are scattered, but in general show a slight negative correlation between these elements, indicative of progressive zircon crystallization in the same magma system. Similar concentrations in both elements for all samples suggests similar ranges of melt fractionation, which is consistent with the broad similarity in whole-rock chemical compositions of the tuffs.

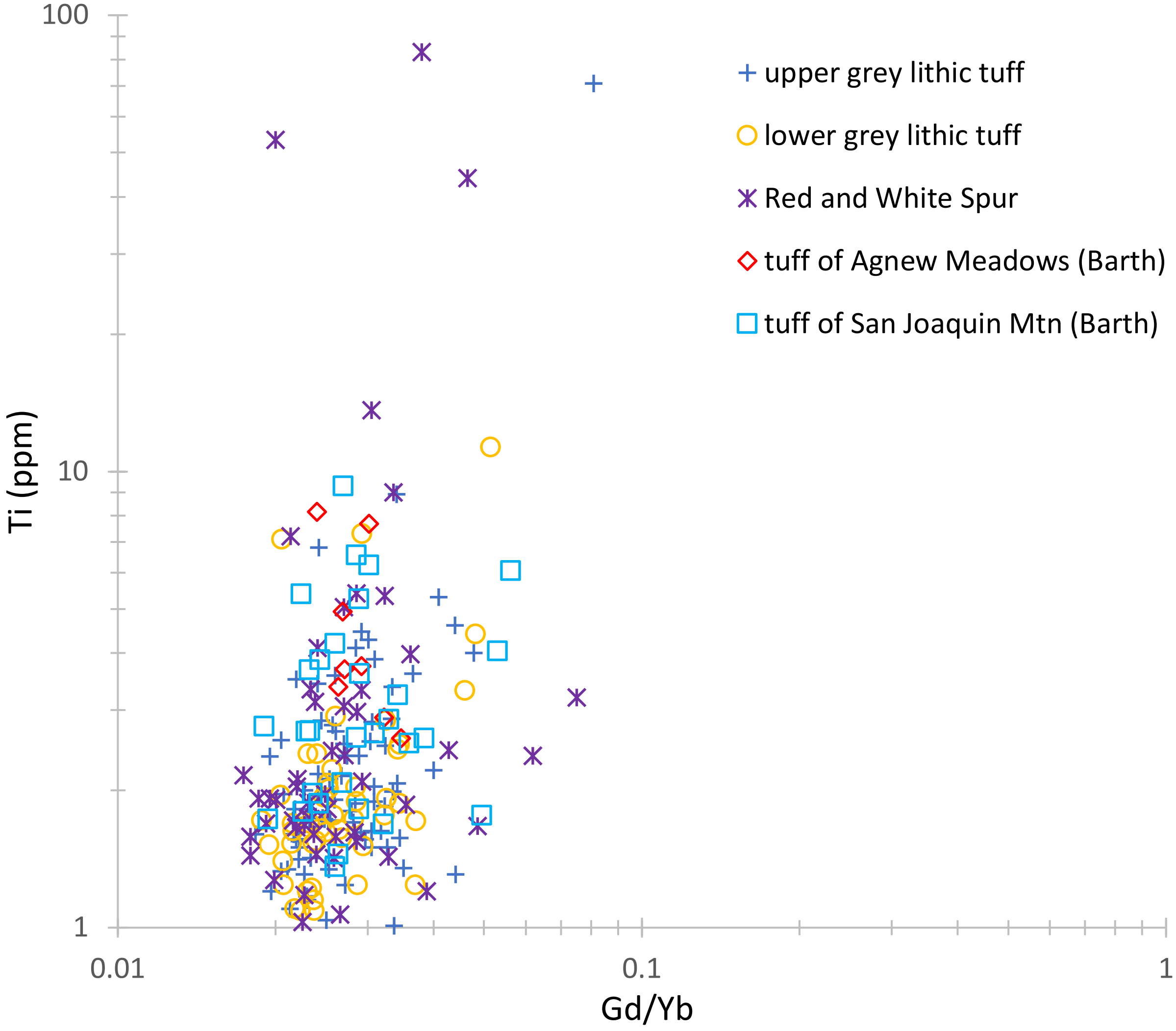

Figure 48: Ti concentration vs Gd/Yb ratio. All zircon from this study and from Barth et al. (2018) are similar, and are between 0.01 and 0.1 Gd/Yb, indicating similarity in source magma composition. The covariation in these zircons is likely driven by the influence of cooling and possibly co-crystallization of phases in competition for REE with later-formed zircon, such as titanite and apatite (Fig. 8 in Grimes et al., 2015).

7. INTERPRETATIONS

The goal of this study was to understand the characteristics of the magmatic arc following the transition from a passive continental margin setting to a volcanic arc in terms of depositional setting, volcanic eruption style, and progression of the arc geochemistry. Two pendants in the eastern Sierra Nevada host rocks that record this transition from Paleozoic passive margin to an active continental magmatic arc. Facies, whole-rock geochemistry, zircon trace element geochemistry, and zircon U-Pb analyses provided the basis for a model for the volcanism and depositional setting in this part of the arc as it was building.

7.1 FACIES INTERPRETATIONS

Most units in this study contain primary volcanic material and non-volcanic clasts from volcanic eruptions or subsequent debris flows. The primary textures of these rocks are often obscured by the effects of metamorphic and hydrothermal alteration, making the interpretation of depositional processes difficult. The majority of the units discussed in this study contain poorly sorted pumice, accidental and juvenile lithic fragments, and phenocrysts in a fine-grained matrix. Most units have flattened fragments of pumice and other lithic fragments that create a planar fabric (bedding and foliation). These deposits could be the result of primary volcanic eruptions and/or pyroclastic density currents that entrained and deposited both primary volcanic clasts and previously deposited volcanic and non-volcanic material. The unsorted nature of the units and the variety of lithic clasts could be the result of a debris flow that remobilized material previously deposited. Both pyroclastic density currents and debris flows could account for the variety of clast lithology, size, shape, and angularity. Fiamme are commonly bent around phenocrysts, which may indicate initial welding and/or subsequent deformation. Quartz phenocrysts are often not broken, and exhibit primary embayment textures, indicating they did not experience significant solid-state deformation. Thus, the deformation of the fiamme and pumices was likely caused by primary welding and burial processes. This suggests pyroclastic density currents are the likely source of heat needed to weld most of these deposits. Poorly sorted units without significant quartz phenocryst deformation and displaying evidence for welding, including bent fiamme, were likely the result of pyroclastic density currents. A higher proportion of volcanic to non-volcanic material also suggests a pyroclastic density current. Deposits with an abundance of non-volcanic clasts and matrix material suggests a debris flow, such as a lahar, was the likely emplacement mechanism.

Widespread sericite, epidote, and mica alteration combined with some scatter in the major element data suggest this area experienced hydrothermal alteration and/or alkali element mobility during regional metamorphism (Sorensen et al., 1993). This is supported by the presence of abundant cross-cutting veins composed of epidote, calcite, and quartz in most units.

Agnew Meadows Area

7.1.1 Tuff of Agnew Meadows

The tuff of Agnew Meadows (220 ± 2 Ma; Barth et al., 2018) is a thick (≥ 150 m) unit with elongate lithic clasts, pumice, and quartz and felspar phenocrysts in a fine-grained groundmass. Lithic clasts in this unit are quartzite that is likely derived from Paleozoic metasedimentary rock from the Palmetto Formation of the Roberts Mountain Allochthon (Rinehart et al., 1964). This formation may have cropped out in the area around the caldera and/or was country rock forming the walls of the magma chamber or the conduit.

7.1.2 Lower grey lithic tuff

The lower grey lithic tuff (221 ± 2 Ma) overlies the tuff of Agnew Meadows and is a < 75-m-thick unit composed of matrix-supported, poorly sorted sub-angular to angular dark grey and tan elongate pumice defining a slight foliation. The phenocrysts are sub-angular to sub-rounded quartz and two feldspars and vary in size. The groundmass is fine-grained quartz and feldspar crystals with widespread sericite and epidote alteration. The more abundant grey pumice clasts in this unit are compositionally similar to the tan pumice clasts. Klug and Cashman (1994) reported two populations of pumice in the deposits from the May, 1980, eruption of Mount St. Helens, with distinct color and textural differences. Lighter tan pumices have fewer phenocrysts, no microlites, and higher vesicularity than the grey pumice. These authors suggested that the differences in vesicle size and percentage resulted from the presence or absence of microlites. Magmas with microlites may fragment at lower bulk vesicularity than those without microlites, suggesting that the microlite-bearing clasts probably expand less after fragmentation The deposits of this eruption of Mount St. Helens reveal that the two pumice types were erupted concurrently for several phases of the eruptions, so likely had similar eruption sources and depositional processes. The lower grey lithic tuff in Agnew Meadows may be the result of a similar process involving different microlite populations. The higher concentration of grey pumice clasts in this unit compared to tan is likely the result of the lower vesicularity and therefore higher density of the grey pumice compared to the tan pumice. The density disparity could result in the grey pumice clasts being deposited closer to the source than the less dense tan pumice clasts.

7.1.3 Pumice conglomerate

The pumice conglomerate unit is a 100-m-thick deposit that overlies the lower grey lithic tuff and extends ~1 km along a northwest-trending strike (Fig. 3). Elongate, tan pumice clasts are 10-125 cm long, and define a foliation. The matrix has fiamme bent around medium- to fine-grained quartz and feldspar crystals with rare micas. The pumice length:width is ~2:1 and many are fused along margins. The concentration and size of the pumice clasts is greatest in the middle of the unit, with as much as 75% surface area composed of pumice and clasts averaging 75 cm long. The edge of the unit is ~50% pumice, and clasts are commonly 10-40 cm long in the outer 15 m of the deposit.

A few of the clasts contain a dark interior whose shape matches the shape of the clast and are about 5% of its volume. Petrography of the contact between the interior and the exterior of such clasts shows a sharp contact. The interior is composed of altered mafic minerals and oxides, although the alteration in all the rocks in this area makes identification of some minerals difficult.

Large pumice clasts are produced by both subaerial and subaqueous silicic eruptions, and the effects of water depth and temperature difference between air and water result in differences in size, vesicularity, and deposition. Large pumice clasts can be produced in subaerial eruptions, such as those produced during the 1980 eruption of Mount St. Helens, which are as much as a meter in diameter (Kuntz et al., 1981). The poorly sorted and sub-rounded pumice clasts were deposited with lithic and smaller grey pumice clasts with a coeval matrix of lapilli and ash (Mackaman-Lofland et al., 2014). According to Klug and Cashman (1996), conditions that promote bubble coalescence, and therefore increased permeability (such as low viscosity in magma and/or low eruption intensities) promote larger pyroclasts. In contrast, high viscosity and/or high eruption intensity would result in larger proportions of ash.

In subaqueous eruption settings, magmas are subject to several physical constraints that are much different than subaerial settings. These include hydrostatic pressure, bulk modulus, heat capacity, thermal conductivity, and the density of water mass (Cas and Simmons, 2018). These are orders of magnitude greater for water than for air, vastly changing the physical characteristics and behavior of magma in subaqueous settings. The exsolved volatile content of the magma in these systems is lower than subaerial systems because the magma decompresses to hydrostatic pressures much greater than atmospheric pressure. Exsolved volatiles are supercritical fluids at pressures greater than the critical points for H_2O and CO_2, meaning they have limited ability to expand (Cas and Simmons, 2018). This retention of volatiles makes subaqueously erupted magmas less viscous than their subaerial counterparts. The explosive expansion of gas bubbles in subaqueous magmas is limited because the gas overpressure is lower under the higher hydrostatic pressure. The high heat capacity of water makes erupted magma prone to rapid cooling and quench fragmentation, and clasts with bulk density less than water can rise buoyantly through the water column before becoming waterlogged (Fig. 49; Cas and Simmons, 2018; Mitchell et al., 2019). The rate at which these buoyant clasts become waterlogged and sink affects the dispersal and sedimentation of the pumice (Cas and Simmons, 2018).

The pumice created by subaqueous silicic systems is often produced by the effusion of silicic magma that form domes and flows (Mitchell et al., 2019). The water around the growing dome causes the pumiceous lava to quench and spall off the carapace (Fig. 49). These pumice clasts can either float up through the water column if the density is low enough or if it is too dense it spalls off the dome and is deposited proximally into unconsolidated volcanic ash from coeval caldera eruptions or phreatomagmatic eruptions from the dome (Downey and Lentz, 2006; Mitchell et al., 2019). These domes can develop on the edges of and outside the caldera but share the same magma source (Kano, 2003; Cas and Simmons, 2018; Manga et al., 2018; Mitchell et al., 2019).

Recent examples of such eruptions were described in the Kermadec and New Zealand arcs. The giant pumice clasts produced by the 1.8-ka subaqueous eruption at Lake Taupo, New Zealand, were the result of a dome carapace quenching and spalling large blocks (von Lichtan et al., 2016). The pumice clasts produced during the 2012 eruption of Havre volcano in the Kermadec arc were the result of magma quenching as it reached the seafloor and eventually becoming waterlogged and sinking back through the water column to come to rest as far as several hundred kilometers from the eruption site (Manga et al., 2018). The distance depends on the vesicularity of the pumice, the clast size, and the water currents (Mitchell et al., 2019). The pumice clasts could therefore be deposited into nearby sediment that is related to the caldera or could be deposited in unrelated, distal sediment.

The matrix support of the pumice conglomerate in this study suggests a subaqueous environment, in which the added pressure of water and the fast quench time allowed silicic magma to vesiculate quickly before spalling or quenching off the magma source (Downey and Lentz, 2006). Manga et al. (2018) also suggested some explosive subaqueous silicic activity accompanies the quench fragmentation (Fig. 49). In this case, the pumice clasts that are too dense to float initially will fall out of the eruption cloud early, while smaller and/or lighter pieces will rise and float. The magma does not form a dome, but rather a spine that forms cooling joints that propagate and initiate spalling of giant pumice. The fragmentation during the eruption creates ash-size particles that land both proximally and distally to the dome. The initial gas content and permeability of the individual pieces allows more permeable pieces to sink more quickly and be deposited proximally. The larger pumice clasts are deposited distally, with distance dependent on wind, current, and the clast density (Manga et al., 2018; Mitchell et al., 2019). Clasts that are initially too dense to float fall out near the vent, while those that can float are deposited some distance away. Pumice clasts that float may abrade each other, which may result in sub-rounded clasts.

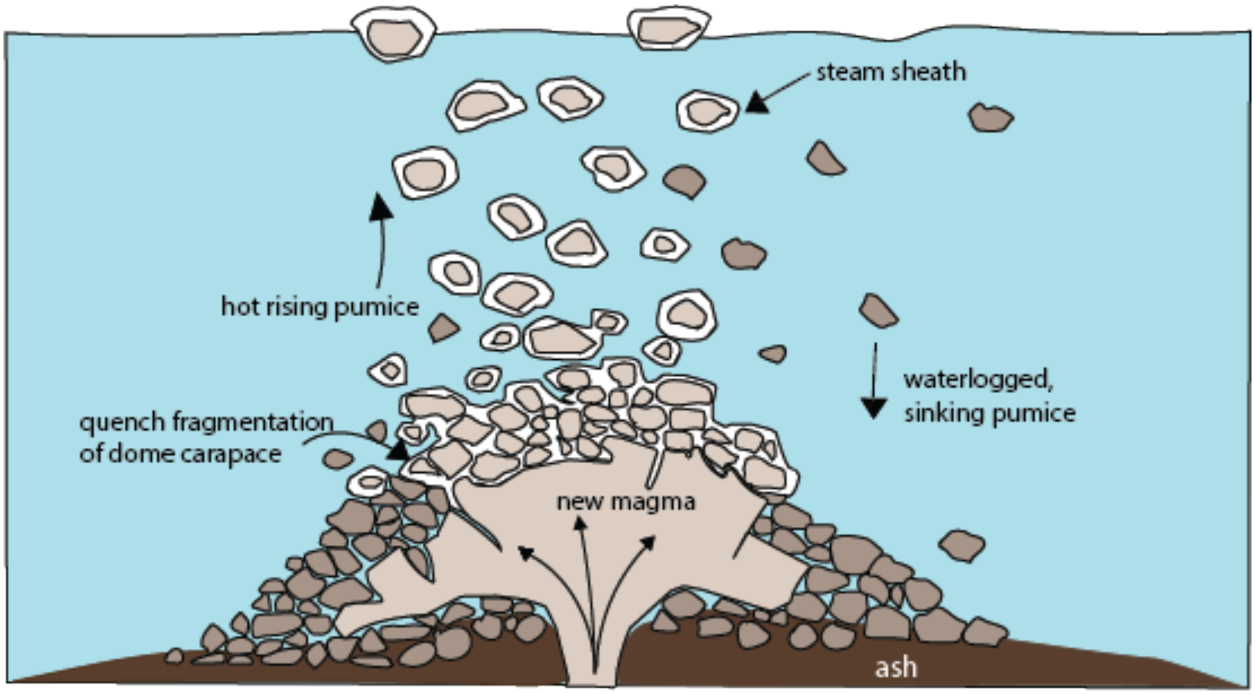

Figure 49: Schematic diagram (modified from Kano, 2003 and von Lichtan et al., 2016) showing a subaqueous silicic dome growing on the seafloor. New magma causes the dome to grow endogenously while water quenches pumice fragments that, if hot enough and impermeable, could rise through the water column. Eventually, these pumice clasts would cool and become waterlogged. When they are waterlogged, they will fall out of the water column and land proximally or distally in unconsolidated ash from the dome and/or caldera eruptions.

One model for the creation and deposition of the pumice conglomerate in the Agnew Meadows area involves a silicic dome. In this model, a dome grew endogenously, and the carapace was quickly quenched and broke irregularly. Pieces of the carapace broke off completely and spalled from the growing structure. If the pumice pieces were too dense to float, they would have simply rolled and tumbled down to come to rest in a pile. In this scenario, the size and density of the clasts would determine how proximally they landed. Denser clasts may have come to rest closer to the base of the dome, while the smaller, lighter pieces might have continued to roll and were deposited farther away. In cross-section, the pile of pumice clasts would be more concentrated near the middle, and less concentrated and with smaller pumice near the edges of the pile, which could explain the concentric clast concentration in map view (Fig. 50). The difference in pumice sizes could also be due to vesicularity and therefore density differences between clasts. The difference in clast concentration and size between the middle and edges of the pumice conglomerate unit could be explained by the differences in pumice density when they were quenched. The matrix in the pumice conglomerate unit in Agnew Meadows has similar characteristics and composition to the surrounding tuff units, suggesting the pumice were deposited in unconsolidated volcanic ash related to the upper and lower grey lithic tuffs. The proportion and size of quartz and feldspar phenocrysts is similar between the matrix of the upper and lower grey lithic tuffs and the pumice conglomerate, suggesting the dome deposits were coeval with the two tuffs.

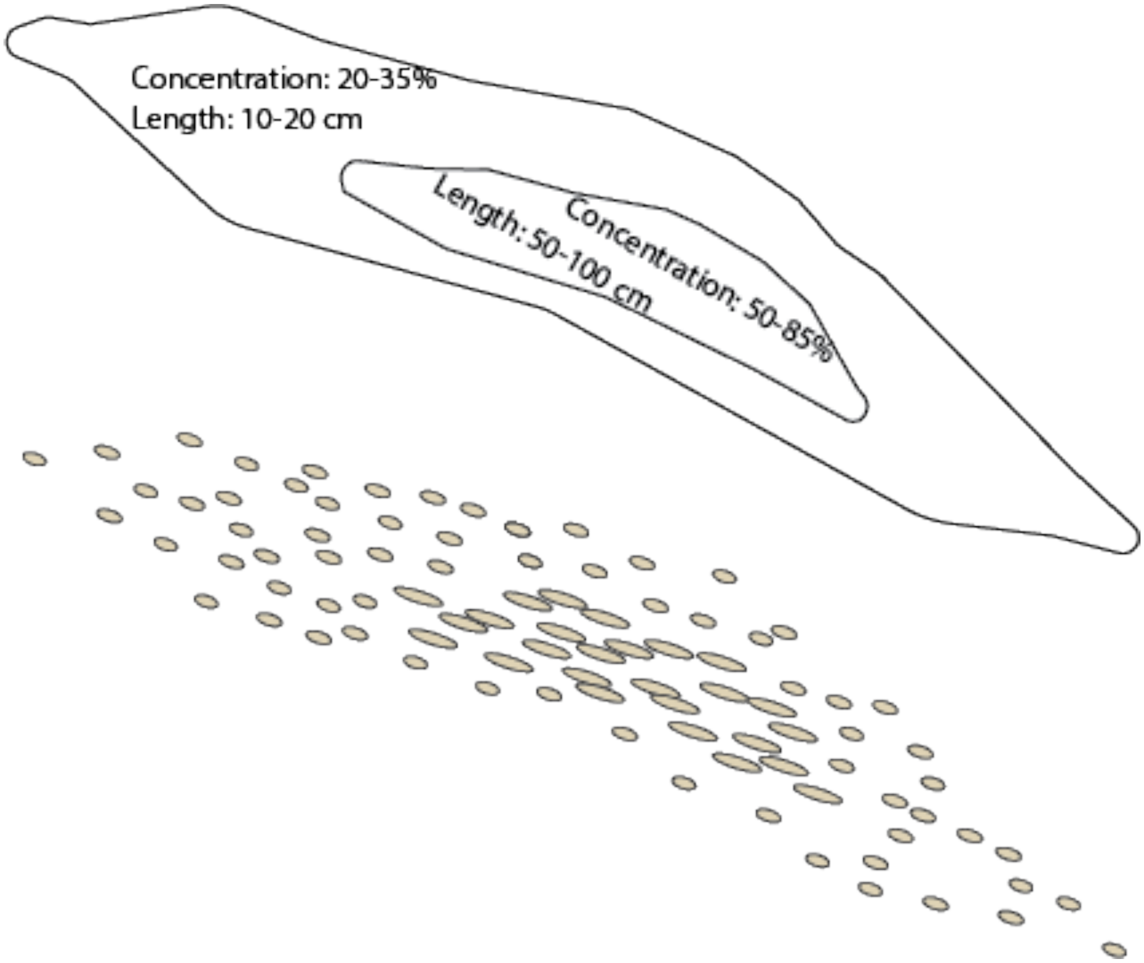

Figure 50: Map view of the pumice conglomerate in Agnew Meadows, showing the high and low concentration and large and small clast sizes. This distribution could represent a talus pile around a silicic dome growing on the seafloor.

Many of the clasts in all areas of the deposit are fused to at least one other nearby clast in the middle or the tip of the clasts. The exact nature of the connection is now obscured by the effects of metamorphism, weathering, and glacial polishing in the area. The clasts were likely fused as they spalled off the dome when the individual pieces were potentially still warm enough to bind to each other. If the clasts were initially roughly equant, very little surface area was fused as the pumice spalled together. The quench separation of clasts from each other may have occurred after landing as water contact continued to cool the surfaces (cf. Cas and

Simmons, 2018; Mitchell et al., 2019). Alternatively, the separation may have occurred in the water column, in which case the quenched clasts may not be deposited with the clasts that stay connected in the water column (Fig. 51; Manga et al., 2018).

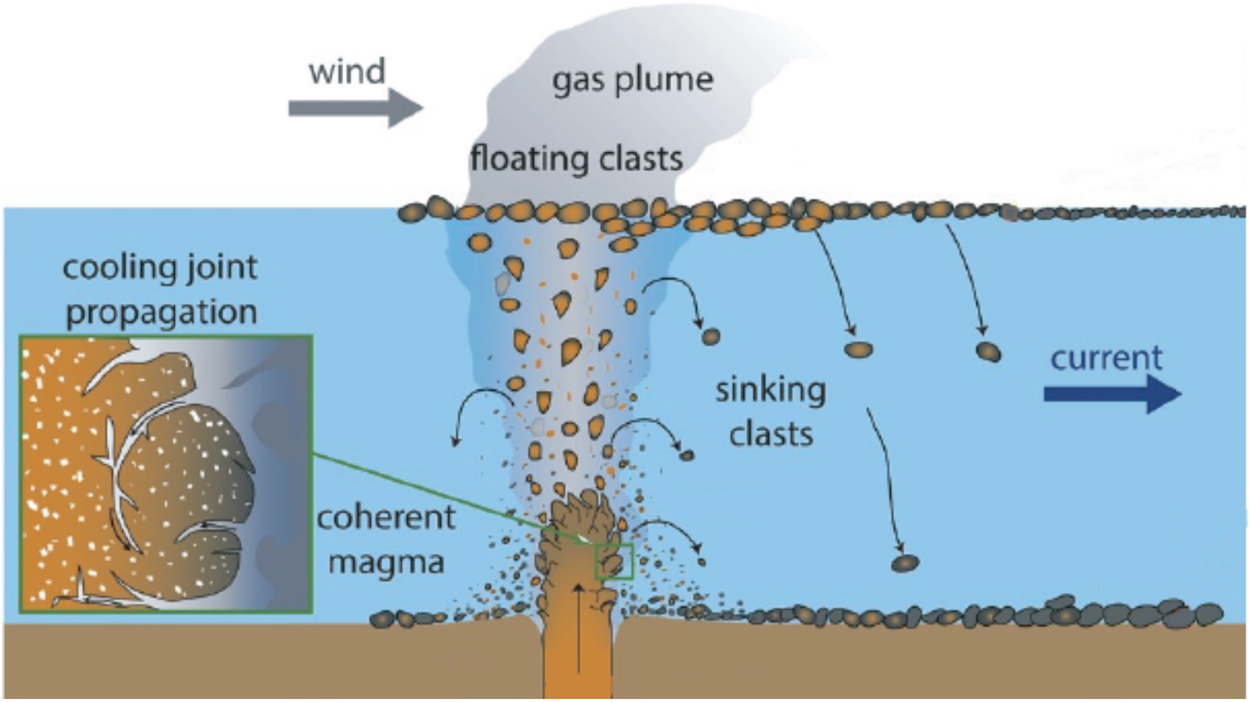

Figure 51: Schematic diagram (modified from Manga et al., 2018) depicting a subaqueous semi-explosive silicic eruption that would produce both large and small pumice pieces with larger, vesicular pieces floating and sinking into to distal and proximal sediment. The pumice conglomerate in Agnew Meadows could be a result of this process, with the matrix formed as a result of fragmentation and fallout coeval with the pumice formation.

The interiors of rare pumice clasts are more mafic in composition, reflecting a different magma was somehow encased in the more silicic interior. Klug and Cashman (1994) suggested that inclusions of more silicic pumice in grey pumice from the 1980 eruption of Mount St. Helens were the result of injection of a compositionally different magma just prior to eruption. The process that created the dark inclusions is difficult to determine without more textural evidence, but one possibility is that the ascending silicic magma entrained mafic clasts from inside the magma chamber, the conduit, or at the surface. The shape of the interior with regard to the overall clast shape suggests the material was soft enough to conform to the shape of the material around it as it formed. This would rule out the possibility of the clasts being solidified mafic clasts on the surface, which would likely be more angular. It is likely that mafic magma was injected into a majority silicic magma just prior to eruption, resulting in “blebs” of mafic magma being surrounded by silicic magma. The mafic magma may have been injected into the silicic magma and cooled, thereby becoming more viscous than the surrounding silicic magma. The heat transfer involved in the cooling would help to stir the magma, distributing the mafic blebs.

This unit is thin and laterally discontinuous, which indicates that it was the product of a localized event. The lateral discontinuity and stratigraphic placement in between ignimbrites suggest this is an extra-caldera setting involving a silicic dome rather than an intra-caldera megabreccia block. The pumice clasts are supported by a fine-grained matrix, which is likely the result of pumice floating and sinking in water rather than air. If the dome produced pumice in a subaerial setting, the resulting conglomerate would have been clast-supported. There is no firm evidence to rule out the possibility of a subaerial dome.

7.1.4 Upper grey lithic tuff

The upper grey lithic tuff (219 ± 2 Ma) is a <50-m-thick unit that overlies the pumice conglomerate and is at least 1 km in length along a northwest-trending strike. This unit has sub-rounded to sub-angular lithic fragments of grey and tan pumice and subhedral quartz and feldspar phenocrysts that define a slight foliation. Petrographic analysis reveals an abundance of alkali feldspar compared to plagioclase and broken and embayed quartz crystals, suggesting a change in magma chamber conditions that led to resorption and/or dissolution prior to eruption. This could have been the result of an injection of new magma or ascent to a shallower storage setting. The grey pumice clasts are larger than the tan pumice clasts and are similar to those in the lower grey lithic tuff that were likely also the result of microlites increasing viscosity and inhibiting bubble coalescence, making the grey pumice denser than the tan pumice (cf. Klug and Cashman, 1994). The upper and lower grey lithic tuffs have similar lithic and phenocryst compositions and proportions. The lithic fragments and phenocrysts in this unit are on average smaller than those in the lower grey lithic tuff, suggesting a less energetic process or a difference in explosivity of the eruption.

7.1.5 Quartzite conglomerate

The quartzite conglomerate unit is poorly sorted with a variety of clast compositions and sizes, and most clasts are sub-angular to sub-rounded. This unit is 150 m along strike and less than 50 m thick. The clasts are Paleozoic quartzite, marble, and other undifferentiated metasedimentary rocks in a matrix containing broken quartz and feldspar crystals, suggesting incorporation of volcanic material. The unsorted nature of this unit combined with the wide range of non-volcanic clast types and sizes suggests nearby volcanic and non-volcanic material was dislodged from outcrops and pre-existing deposits in the landscape and transported and deposited by a lahar. The dominant sub-angular clasts suggest minimal abrasion and transport, but the rounded nature of the quartzite clasts suggest prior transportation and abrasion. The quartzite clasts in this unit are similar in composition and size to those in the tuff of Agnew Meadows, so may have been dislodged from an outcrop of Paleozoic rock in the landscape and are likely from the same unit (Palmetto Formation of the Roberts Mountain Allochthon). Outcrops of this formation may have formed canyon walls or scarps previously eroded by debris flows. This deposit is surrounded by tuffs indicating eruptive activity before, during, and after its emplacement.

7.1.6 Tuff of San Joaquin Mountain

The tuff of San Joaquin Mountain (221 ± 2 Ma) overlies the upper grey lithic tuff and the quartzite conglomerate. This unit is at least 75 m thick and extends for a minimum of 1.5 km along strike. This unit is a lithic-rich tuff with fragments of primarily grey pumice with few tan pumice and rare Paleozoic(?) metasedimentary lithic fragments. This unit is poorly sorted with a matrix of quartz and feldspar phenocrysts with medium-grained, euhedral to subhedral quartz and feldspar phenocrysts. This unit is similar in composition to the lower grey lithic tuff and upper grey lithic tuff, suggesting it is related to the same caldera. This unit is thinner than the similar facies of the tuffs of Skelton Lake at Skelton Lake and the coarse lithic-rich tuff in Red and White Spur to the southeast, suggesting it is an extra-caldera deposit.

Skelton Lake Area

7.2.1 Tuff of Skelton Lake

The tuff of Skelton Lake at Skelton Lake is a thick (1.2 km) poorly sorted deposit of lithic fragments in a matrix enclosing medium- to fine-grained quartz and feldspar phenocrysts (Figs. 1, 7; Field, 2018). Field (2018) reports a total length of 13 km along strike, extending to the Red and White Spur area to the southeast. Glomerocrysts are present in dark clasts in this unit and are composed of equal parts quartz and two feldspars. The matrix of the clasts contains mafic minerals, including hornblende and rare pyroxenes. The composition of these clasts suggests magma mixing, decompression, and resorption occurred in the magma chamber prior to eruption (cf. Hogan, 1993). The phenocryst composition, proportions, lithic clast compositions, and zircon U-Pb age (220 ± 2 Ma) suggest this deposit is related to the tuff of San Joaquin Mountain in the Agnew Meadows area. This tuff has larger phenocrysts and dense, larger lithic clasts than the tuff of San Joaquin Mountain, and this combined with the thickness implies the tuff of Skelton Lake in this area is more proximal to a caldera. Larger, more dense material is often deposited closer to the caldera because these clasts cannot travel as far as finer particles from the same eruption (Lipman, 1984).

Red and White Spur Area

Field (2018) interpreted facies in the Red and White Spur area to represent caldera margin and fill based on the presence of chaotic breccia, higher proportions of larger lithic clasts than the Skelton Lake area, and a thickness greater than 1 km. Field (2018) also suggested that the unit is finer grained to the northwest and has a total length of 13 km along strike, suggesting the Red and White Spur area facies are most proximal and Skelton Lake is within the caldera. Lipman (1984) and Busby-Spera (1984) both suggested that thicknesses greater than 0.5 km are indicative of intra-caldera facies. These units may have originally been much thicker since rocks in the Ritter Range pendant experienced up to 50% shortening normal to cleavage and bedding (Tobisch and Fiske, 1976). The present study provides more detail for the facies in the proximal caldera-wall breccia and fill at the Red and White Spur area.

7.1.8 Coarse lithic-rich facies

Field (2018) did not differentiate facies within the tuff breccia in the Red and White Spur area. The coarse lithic-rich facies is within the 300-m thick tuff breccia as described by Field (2018). The coarse lithic-rich facies at Red and White Spur is a ≥ 200 m-thick tuff that extends for at least 2 km along a northwest/southeast strike (Figs. 1, 4). This unit is composed of poorly sorted, large (3-50 cm) angular to sub-angular grey pumice and dense grey Paleozoic metasedimentary clasts in a grey, medium-grained matrix of subhedral quartz and feldspar phenocrysts (1-3 cm). Most clasts are equant and do not define any foliation. This unit is too voluminous to be an extra-caldera deposit (Cole et al., 2005), suggesting this is an intra-caldera deposit and so is interpreted as caldera fill (Field, 2018). The greater thickness and higher abundance of larger lithic clasts in the tuff at Red and White Spur compared to the Skelton Lake area also implies it is an intra-caldera deposit that is related to the thick, compositionally similar tuff of Skelton Lake at Skelton Lake, and the thin extra-caldera tuff of San Joaquin Mountain in the Agnew Meadows area. This is further supported by the lack of bedding or sorting combined with the variability in size and shape of lithic clasts and phenocrysts, that on average are larger than those in the Agnew Meadows area and the Skelton Lake area. The Paleozoic metasedimentary lithic clasts in this unit likely formed the country rock below and around the caldera and were entrained in the eruptions or fell from the caldera walls. The ≥300 m thickness, chaotic nature of the sorting, and angularity of clasts in this facies suggests it was a lag breccia and/or material that fell from the caldera margins (Field, 2018). Busby-Spera (1984) reported megabreccia blocks up to 0.5 km in length that were from the caldera wall and floor that were incorporated into the intra-caldera ignimbrite deposits as the caldera filled. The outcrop of coarse lithic-rich facies in this study could thus be a part of a megabreccia block more than 100 m long.

7.1.9 Fine lithic-rich facies

Field (2018) did not discuss the details of this facies within the tuff breccia of Skelton Lake in the Red and White Spur area. The fine lithic-rich facies in the Red and White Spur area is southwest of the coarse facies and is similar in composition and texture, but hosts smaller clast sizes. This unit is ~ 150 m thick and extends for at least 1 km along strike. Clasts are mostly sub-angular grey vesicular pumice and grey Paleozoic metasedimentary rocks and the shape and composition of clasts is similar to the coarse facies nearby, but the overall size is smaller. The proximity to the coarse unit nearby suggests this unit is also intra-caldera megabreccia block (cf. Lipman, 1976). The size and shape of this deposit are difficult to assess, so the exact relation between this unit and the coarse lithic-rich facies is unknown.

7.1.10 Fine-grained tuff

Field (2018) did not differentiate this unit from other facies in the Skelton Lake area. The fine-grained lithic tuff in this area has few to no visible lithic fragments in a very fine-grained volcanic ash matrix. This tuff facies is similar to the tuff of Skelton Lake at Skelton Lake, implying it is related to that intra-caldera deposit. The fine-grained nature of this unit and the lack of foliation suggest this facies is the matrix around the intra-caldera megabreccia blocks in the area.

7.2 GEOCHEMISTRY INTERPRETATIONS

7.2.1 Whole-rock major element geochemistry

On a TAS diagram (Fig. 37), all the units analyzed in the three areas in this study are rhyolitic, the clast in the lower grey tuff is dacitic, and the clast in the tuff of Skelton Lake is trachydacitic. The lower silica content of the two clasts suggests injection of mafic magma just prior to eruption (cf. Klug and Cashman, 1994). The whole-rock data also reveal high potassium content and a wide range of values in sodium and phosphorous content (Fig. 37).

The eastern Sierra Nevada experienced more than 100 million years of potassium metasomatism, which is recorded in Triassic and Jurassic rocks in the area that were altered by seawater infiltration, hydrothermal alteration, and regional metamorphism (Hanson et al., 1993). This alteration may have been the cause for the high percentage of sericite, and therefore potassium, in all samples. This mineralization increased the total alkali values. Despite these alkali trends, the rocks still plot as rhyolite, but fractional crystallization trends are difficult to determine due to the scatter of the data on Harker variation diagrams. Potassium could also have been added to the magma via contamination of the magma by the upper crust. Only some of the other volcanic rocks in the Mount Morrison and Ritter Range pendants show high potassium content (Berglin, 2021). Therefore, it is likely that this increased potassium content is the result of metasomatism and a contribution from the crust and is therefore not reliable for use in determining fractional crystallization trends for a single magma system.

The major element oxides for the rocks in this study show some weak negative trends for Al_2O_3, Fe_2O_3*, MnO, and MgO and scatter in the data for CaO, Na_2O, K_2O, or P_2O_5 (Fig. 38). The latter are low-charge cations, which are mobile in fluids, so may have been affected by metamorphism or hydrothermal alteration in addition to the effects of partial melting, magma mixing, and/or crustal contamination. The scatter in the data for the low-charge cations could also indicate different volcanic sources, as products of the same volcanic source should follow trends for each oxide (Harker, 1909). Given the similarity in phenocryst composition and proportion, proximity of the units to one another, and the trends present in some oxides, it is likely the rocks are from the same volcanic source and the scatter is caused by other processes.

7.2.2 Zircon trace element geochemistry

The zircon data in this study are combined with zircon trace element data from Barth et al. (2018) to compare trace element geochemistry and support a petrogenetic link. Hafnium concentrations in zircon range from 7,500 to 12,500 ppm (Fig. 40). Zircon crystals with relatively high Hf have lower Th/U and are enriched in heavy rare-earth elements (higher Yb/Gd) compared to the lower-Hf grains (cf. Barth and Wooden, 2010). The overall compositional ranges and trends are similar in all samples, including those from Barth et al. (2018), suggesting that all zircon crystals share the same magmatic source. Barth et al. (2012) used the similarities in these trends to imply that ash-flow tuffs in the Saddlebag Lake pendant and intrusive rocks of the Scheelite Intrusive Suite are petrogenetically linked and provide substantial evidence for the presence of a long-lived, multi-stage, upper-crustal magma system.

Several trace element concentrations and ratios in zircon crystals are used to differentiate arc magmas and arc settings. Zircon crystals with U/Yb greater than ~0.1 and as high as 4 are characteristic of continental arc magmas (Grimes et al., 2015). This ratio increases with Hf concentration and fractionation, and the zircon crystals in this study have a U/Yb value >0.9, which strongly suggests they crystallized in a magma system hosted in thick, mature continental crust enriched in large-ion lithophile elements (cf. Grimes et al., 2015). U is highly incompatible, meaning crustal contamination will increase its concentration in magmas, and Yb is a HREE element and is preferred by garnet and amphibole crystallizing at relatively high lithostatic pressures (Mantle and Collins, 2008; Sundell et al., 2022). Fractionation alone would show covariation in U with respect to Hf, as both are incompatible during fractionation. The high U/Yb ratio is representative of a high LREE/HREE ratio, which points to residual melts depleted of HREEs due to competition with garnet and amphibole (Heaman et al., 1990). The concentrations of the incompatible HREE, Th, and U typically increase with magma differentiation, though zircon Th and U contents outpace the HREE increases, thereby increasing U/Yb and Th/Yb ratios in zircon (Reimink et al., 2020). Fractionation in the upper crust, and in the absence of HREE-fractionating garnet, results in an increase in Yb/Gd during fractionation involving plagioclase (Bell and Kirkpatrick, 2021). The magma could have been originally fractionated at depth, then in the shallower crust where contamination also complicated the U concentration. The crustal contamination is further supported by a Th/Yb value >0.1, which Grimes et al. (2015) also established indicates continental upper-crustal involvement. Th/Yb does not covary with Hf concentration, as would be expected from fractionation alone. Rather the Hf concentration increases and the Th/Yb ratio remains constant, suggesting LREE enrichment, likely from contamination in the upper crust. Zircon derived from deeper magmas show a deficit in Yb from garnet fractionation and suppression of plagioclase crystallization (Reimink et al., 2020). The continental-arc setting in this study is supported by the relation of Nb/Yb vs U/Yb. The values for zircon in this study (Fig. 43) are completely within the continental magmatic arc zircon array field of Grimes et al. (2015). The same conclusion is implied by the relation between U and Nb, as all zircon grains in the present study have U/Nb well over 10, with most over 100, which is associated with continental magmatic arcs. MORB-derived magma in thin crustal settings would have low U/Nb values, as U is fractionated into plagioclase (Grimes et al., 2015). All zircon data also cluster for most elements when plotted on a multi-element diagram normalized to mid-ocean ridge (MOR)-derived zircon (Grimes et al., 2015), and are most similar to the trends for the continental arc compilation and post-collisional tectono-magmatic settings from the same study (Fig. 44). The relative uptake of light and heavy rare earth elements (LREE and HREE) provides information on the relative continental crustal thickness. Trace element ratios such as U/Yb and Th/Yb relate LREE to HREE, and zircon with elevated LREE/HREE can be interpreted to have formed in thick crust where HREE are preferentially incorporated into garnet and amphibole and there is an abundance of incompatible LREE (Sundell et al., 2022). The increase in U/Yb with decreasing zircon crystallization age suggests a relative thickening of the continental crust. This suggests that the zircon in tuffs in the Agnew Meadows area, the tuff of Skelton Lake, and the tuffs in Red and White Spur are geochemically and petrogenetically similar and are the result of an oceanic-continental subduction zone involving relatively thick continental crust that contaminated an upper-crustal magma. When plotted against the U-Pb age for individual zircon, the U/Yb ratio is higher in younger zircon grains (Figs. 45, 46), implying some level of fractional crystallization or changes in magma chemistry due to crustal thickening and contamination during the 2- to 8-million-year history of this volcanic complex.

8. DISCUSSION

The goal of this study was to determine the paleogeography, eruption dynamics, and depositional processes and settings of Triassic rocks in two pendants in the eastern Sierra Nevada, California. Facies, whole-rock major element, zircon trace element, petrographic, and zircon U-Pb geochronology analyses provide evidence to suggest the early eastern Sierra Nevada arc was in a shallow-marine oceanic-continental subduction zone setting from at least ca. 223 to 216 Ma.

Several lines of evidence link three volcaniclastic rock successions in the Ritter Range and Mount Morrison pendants in the eastern Sierra Nevada, California. These rock units all lie along strike, and Field (2018) suggested that two facies in the Mount Morrison pendant are linked to the same source. The tuff of San Joaquin Mountain in Agnew Meadows is a 50 m-thick tuff that is compositionally similar to both the tuff of Skelton Lake at Skelton Lake and the lithic-rich tuff at Red and White Spur. The tuff of San Joaquin Mountain is thinner than the tuff of Skelton Lake. The high percentage of sub-angular lithic clasts in the facies at Red and White Spur suggests it is the most proximal to the caldera of the three facies. Field (2018) suggested that the 300-m-thick facies at Red and White Spur is caldera-wall breccia and fill, implying the caldera that produced the three facies is centered around the Red and White Spur area. These facies are coarser grained than those in the two other areas, and Field (2018) suggested the thickness of the unit and the chaotic nature of the breccia indicates an intra-caldera deposit (cf. Busby-Spera, 1984; Lipman, 1976; Cole, 2005). The coarse-grained tuff could be an outcrop of an up to 500-m-diameter megabreccia block encased in the tuff of Skelton Lake (cf. Busby-Spera, 1984). Whole-rock and zircon trace-element geochemistry are clustered and suggest the rocks in the three areas are petrogenetically linked, and zircon U-Pb ages overlap within 6 million years. The three facies were likely produced by formation and evolution of a caldera (e.g. Lipman, 1976; Cole, 2005) that deposited material at least as far as the Agnew Meadows area to the northwest. The pumice conglomerate may be the remnants of a talus pile produced by a silicic dome in the Agnew Meadows area (Fig. 52). The dome could also have been closer to the caldera margin and produced a pumice raft that sank and was deposited in the Agnew Meadows area, as is common in calderas of the Kermadec arc (Fig. 52; Rotella et al., 2013).

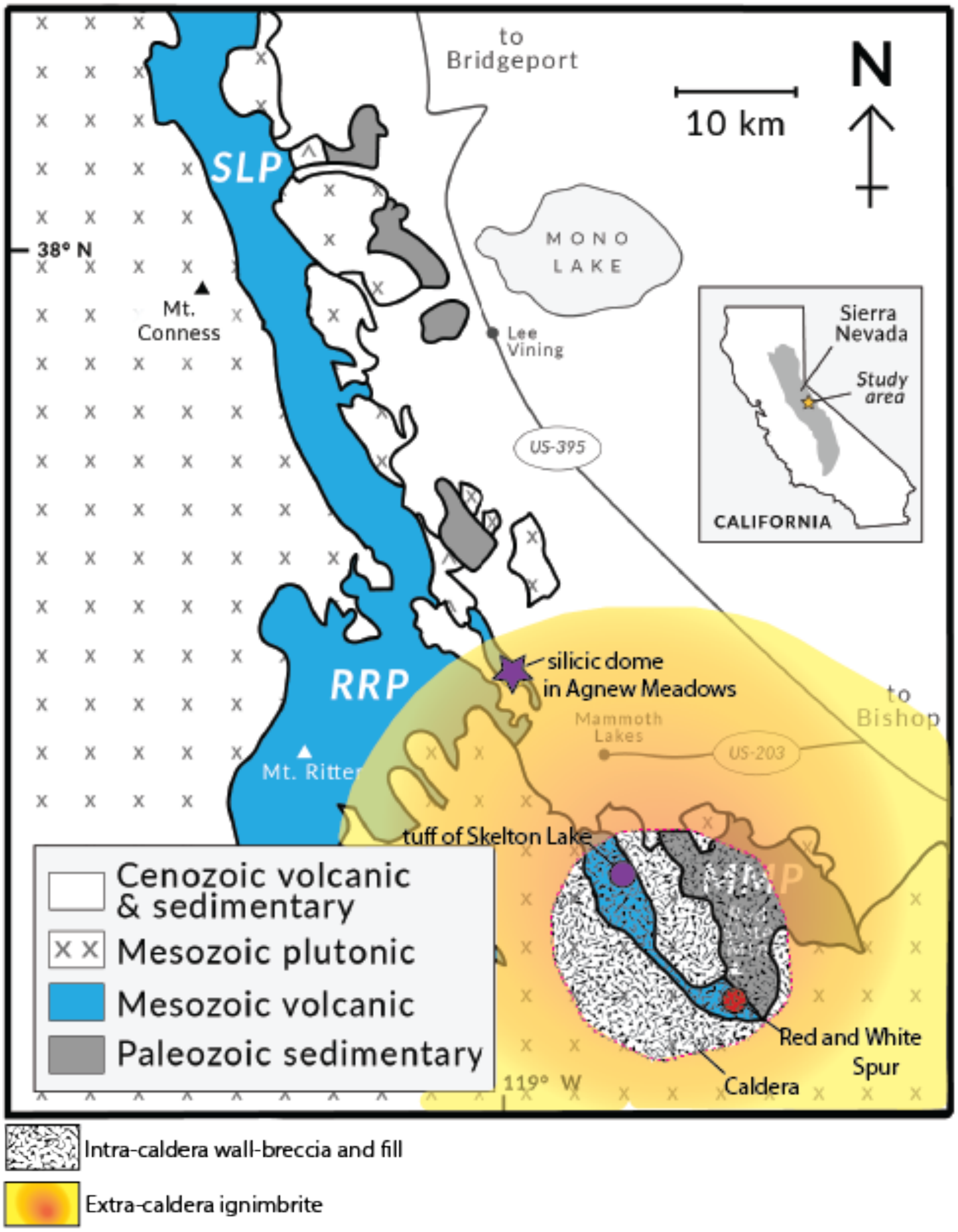

Figure 52: Summary figure of the caldera and extra-caldera ignimbrite extent. The full extent of the ignimbrite is unknown given the lack of available outcrops in the Ritter Range pendant. The caldera margin is based on thickness of the tuffs in the Mount Morrison pendant.

Observations of shallow-marine rocks from the Late Triassic Sierran arc are widespread, including in the northeastern edge and interior of the Mount Morrison pendant (Roberts, 2013; Paterson et al., 2014; Barth et al., 2018; Field, 2018). Textures indicative of subaqueous volcanic activity are widespread in breccias in the Mount Morrison, Ritter Range and Saddlebag Lake pendants (Savage, 2021; Berglin, 2021), The presence of lenses of sandstone and pelecypod-bearing limestone in the pendants also suggests a subaqueous depositional setting during Triassic time (Rinehart and Ross, 1964; Fiske and Tobisch, 1978; Berglin, 2021). The textural and stratigraphic characteristics of the pumice conglomerate in the Agnew Meadows area suggest it was deposited in a shallow-marine setting. The rocks in Agnew Meadows are geochemically and geochronologically correlated with rocks in the Red and White Spur area in the Mount Morrison pendant, suggesting the rocks in the two areas are petrogenetically linked.

The calderas of the Kermadec and the Izu-Bonin arcs provide incomplete analogs for subaqueous rhyolitic eruptions and depositional processes. The 2012 eruption of Havre volcano produced a raft of floating pumice formed by the effusive eruption of a rhyolitic vent on the edge of a caldera (Manga et al., 2018). The moderate water depth (900 mbsl) allowed the lava to effusively erupt onto the seafloor and cooling joints caused pieces of lava to break off as pumice and float in the seawater. The pumice is similar in composition to the ash found proximal to the source vent, leading Manga et al. (2018) to suggest they were contemporaneous though produced by different eruptions. The Sierra Nevada calderas may have been a similar depth to allow effusive and explosive eruptions. The Izu-Bonin arc also contains nine silicic calderas, including the Myojin Knoll caldera measuring 6 x 7 km in diameter

(Fiske et al., 2001). The Myojin Knoll volcano is the coalescence of at least three seafloor rhyolitic volcanoes made up of domes, lava flows, and volcaniclastic debris. Fiske et al. (2001) also found that syn-caldera pumice deposits are lithologically similar to the domes and thick lava flows of the volcano-building phase. The similar lithology in the Izu-Bonin arc further suggests similarity in eruptions and sources for the rocks in the Sierra Nevada. The Late Triassic Sierra Nevada caldera complexes may have been a similar size (13 km diameter and at least 200 km^3, Field, 2018), and were the result of many domes, flows, and explosive eruptions. The silicic subaqueous calderas in both the Kermadec and Izu-Bonin arcs may have similar eruption and deposition processes, but the tectonic setting of the Sierra Nevada system does not have a satisfactory geologically recent or modern analog.

Barth et al. (2011) documented an age of ca. 232 million years for the Black Mountain tuff, Barth et al. (2018) reported an age of 235 Ma for the oldest grain in Triassic tuffs in the Ritter Range pendant and 236 Ma in the Saddlebag Lake pendant, and Cao et al. (2015) documented an age of ca. 232 million years for the intrusion of the Spiller Canyon pluton, indicating that the earliest magmatism in this area of the eastern Sierra Nevada was approximately 15 million years before the widespread emplacement of silicic ignimbrites in the Ritter Range and Mount Morrison pendants. Granodioritic to granitic rocks of the underlying Scheelite Intrusive Suite range in age from 226 to 218 Ma, suggesting that batholith construction began within ~10 million years of the beginning of juvenile-arc silicic volcanism. The volcanic rocks are likely the product of an established silicic magma system that followed the eruption of older, mafic units in the pendants, like the breccia of Mammoth Rock (225 Ma, Berglin, 2021). The age distribution of rocks in the Mount Morrison pendant corresponds with pulses of Sierran arc volcanism recorded across the Sierra Nevada (Cao and Paterson, 2016; Barth et al., 2012, 2018; Field, 2018). The zircon U-Pb ages for the rocks in the current study further support the idea that the Triassic rocks in the pendants were emplaced in conjunction with intrusive rocks in a major pulse of Sierran arc magmatism between 226 and 216 Ma (Barth et al., 2011; Barth et al., 2012, 2018; Field, 2018).

The facies, geochemistry, and age of units in the three areas in this study expand the dataset and support the conclusions of Barth et al. (2018) and Field (2018). Units along strike in the Ritter Range and Mount Morrison pendants collectively support the presence of a caldera at least 13 km in diameter centered around the Red and White Spur area that was the source of ignimbrites that were accompanied by unstable slope slumps and debris flows and silicic domes. The Triassic landscape in this area likely consisted of large calderas fed by evolved magma chambers that were contaminated by the upper part of thick continental crust, which promoted cooling of the magma and crystal fractionation. Calderas formed and are the surface manifestation of some of the earliest silicic arc magmatism in the area. The early Mesozoic continental arc was building in a subsiding region of low relief near and below sea level (Fiske and Tobisch, 1978; Saleeby et al., 1978; Busby-Spera, 1983, 1984). The silicic magmatism followed at least 12 million years of subduction-related magmatism, and was accompanied by faulting, uplift, and deformation (Saleeby and Dunne, 2015). Induced subduction causes crustal thickening, thrust, uplift of the upper plate, and arc magmatism (Stern, 2004). The increase in U/Yb and LREE/HREE as the arc progressed suggests a thickening crust as the arc continued to build. Evidence for faulting and subsidence in older rocks in east-central California were interpreted by Lodes (2020) and Levy et al. (2021) to be related to the initial stages of induced subduction initiation.

9. CONCLUSIONS

The Mount Morrison and Ritter Range pendants in the eastern Sierra Nevada in California expose the transition from the Paleozoic Laurentian passive margin to the Mesozoic Cordilleran arc. The California-Coahuila transform fault truncated the passive margin, resulting in oblique convergence and the induced initiation of a subduction zone. During this transition, uplift, thrusting, arc magmatism, and crustal thickening affected the upper plate. The Triassic volcaniclastic rocks are some of the oldest volcanic deposits in the Mount Morrison and Ritter Range pendants. The facies, geochemical signatures, and ages of the units in the Agnew Meadows, Skelton Lake, and the Red and White Spur areas provide context for the paleogeography and eruption dynamics of some of the earliest rhyolitic arc volcanism.

Facies analysis of the volcaniclastic rocks in the Agnew Meadows area provides several indications about the eruption dynamics and depositional setting during Late Triassic (221-216 Ma) volcanic eruptions that produced voluminous tuffs and localized dome deposits. Tuffs in the Agnew Meadows area (218-221 Ma) have lithic clasts that are primarily Paleozoic quartzite and undifferentiated metasedimentary rocks. The tuffs also contain tan and grey pumice, and abundant phenocrysts of plagioclase, potassium feldspar, and quartz with rare hornblende, pyroxenes, and oxides. Fiamme are abundant in rocks in the Agnew Meadows area and are commonly bent around phenocrysts. The tuff of Skelton Lake at Skelton Lake (217 ± 2 Ma, Barth et al., 2018) and the lithic facies in the Red and White Spur area (220 ± 2 Ma) have similar types and proportions of phenocrysts as the tuffs in the Agnew Meadows area, suggesting cogenesis. The intra-caldera megabreccia and thick fill in the Mount Morrison pendant are the intra-caldera facies related to the extra-caldera deposits in the Agnew Meadows area. Sericite, epidote, and chlorite are abundant alteration products, and were likely the result of contact metamorphism.

Whole-rock geochemistry of the rocks in the Agnew Meadows area, Skelton Lake, and the Red and White Spur area indicate they are high-silica rhyolites with low Mg#. The low Mg# suggests the magma source was an evolved andesite that fractionated from a primitive melt. The zircon trace element data are consistent with a continental arc magmatic setting with a thick crust and upper-crustal contamination. These data also suggest continued zircon crystallization in the magma system, and all zircon data are well clustered for all samples and with those previously analyzed by Barth et al. (2018). This further supports a petrogenetic link between the zircon crystals in rocks with similar phenocryst and lithic clast populations in the three areas.

The lithic-rich facies in the Red and White Spur area and the tuff of Skelton Lake in the Mount Morrison pendant are similar in age, textural characteristics, and composition to the tuff of San Joaquin Mountain in the Agnew Meadows area, though with coarser lithic and phenocryst populations. The lithic-rich facies are chaotic megabreccia blocks at least 300 m thick, suggesting the Red and White Spur area is intra-caldera. The intra-caldera tuff is 1.2 km thick at

Skelton Lake in the Mount Morrison pendant and thins to 50 m in the extra-caldera tuff of San Joaquin Mountain in the Ritter Range pendant. The three units are related and suggest at least one caldera was at least 13 km in diameter and was fed by the same magma system as effusive domes nearby. At least one dome was located either on the caldera margin or as far away as the Agnew Meadows area.

This study supports the hypothesis of Field (2018) that the remnants of at least one large caldera complex crop out in two pendants in the Sierra Nevada, separated by the Cretaceous batholith. At least one caldera produced frequent explosive eruptions of rhyolitic volcaniclastic material, which resulted in multiple tuffs with poorly sorted lithic fragments sourced from the conduit and the landscape, as well as pumice and quartz and feldspar phenocrysts. Vesicular, buoyant pumice clasts were produced by the effusive eruption of a rhyolitic dome that quenched quickly in seawater, allowing the hot pumice clasts to rise through the water column before becoming waterlogged and sinking into unconsolidated tuff erupted from the nearby caldera and emplaced by contemporaneous PDCs. Sometime during the caldera eruptions, a lahar entrained metasedimentary clasts and volcanic material and deposited a block of quartzite conglomerate. These findings suggest the Late Triassic landscape along the western edge of Triassic North America was dotted with calderas and domes that erupted in a subaqueous marine setting. These calderas are some of the earliest silicic volcanism related to the initiation of a subduction zone at least 15 m.y. prior, and may have been active for at least 2 and as long as 8 m.y.

REFERENCES

Bailey, R.A., Dalrymple, G.B. and Lanphere, M.A., 1976. Volcanism, structure, and geochronology of long valley caldera, mono county, california. Journal of Geophysical Research, 81(5), pp.725-744.

Barker, S.J., Rotella, M.D., Wilson, C.J.N., Wright, I.C., and Wysoczanski, R.J., 2012, Contrasting pyroclast density spectra from subaerial and submarine silicic eruptions in the Kermadec arc: implications for eruption processes and dredge sampling: Bulletin of Volcanology, v. 74, p. 1425–1443, doi:10.1007/s00445-012-0604-2.

Barth, A.P. and Wooden, J.L., 2010. Coupled elemental and isotopic analyses of polygenetic zircons from granitic rocks by ion microprobe, with implications for melt evolution and the sources of granitic magmas. Chemical Geology, 277(1-2), pp.149-159.

Barth, A.P., Walker, J.D., Wooden, J.L., Riggs, N.R., and Schweickert, R.A., 2011, Birth of the Sierra Nevada magmatic arc: Early Mesozoic plutonism and volcanism in the east-central Sierra Nevada of California: , p. 21.

Barth, A.P., Feilen, A.D.G., Yager, S.L., Douglas, S.R., Wooden, J.L., Riggs, N.R., and Walker, J.D., 2012. Petrogenetic connections between ash-flow tuffs and a granodioritic to granitic intrusive suite in the Sierra Nevada arc, California, Geosphere, v. 8, no. 2, p. 250-264.

Barth, A.P., Tani, K., Meffre, S., Wooden, J.L., Coble, M.A., Arculus, R.J., Ishizuka, O., and Shukle, J.T., 2017, Generation of silicic melts in the early Izu-Bonin arc recorded by detrital zircons in proximal arc volcaniclastic rocks From the Philippine Sea: Geochemistry, Geophysics, Geosystems, v. 18, p. 3576–3591, doi:10.1002/2017GC006948.

Barth, A.P., Wooden, J.L., Riggs, N.R., Walker, J.D., Tani, K., Penniston-Dorland, S.C., Jacobson, C.E., Laughlin, J.A., and Hiramatsu, R., 2018, Marine volcaniclastic record of early arc evolution in the eastern Ritter Range Pendant, central Sierra Nevada, California: Geochemistry, Geophysics, Geosystems, v. 19, p. 2543–2559, doi:10.1029/2018GC007456.

Bas, M.J.L., Maitre, R.W.L., Streckeisen, A., Zanettin, B., and IUGS Subcommission on the Systematics of Igneous Rocks, 1986, A Chemical Classification of Volcanic Rocks Based on the Total Alkali-Silica Diagram: Journal of Petrology, v. 27, p. 745–750, doi:10.1093/petrology/27.3.745.

Bateman, P.C., 1992, Plutonism in the central part of the Sierra Nevada batholith, California: U.S. Geological Professional Paper 1483, 186 p.

Bell, E.A., and Kirkpatrick, H.M., 2021, Effects of crustal assimilation and magma mixing on zircon trace element relationships across the Peninsular Ranges Batholith: Chemical Geology, v. 586, p. 120616, doi:10.1016/j.chemgeo.2021.120616.

Berglin, S.K., 2021, Volcanic facies and geochemical analysis of the Triassic Mammoth Rock reccia as a test of early-arc paleogeography and subduction inception, eastern Sierra Nevada, California, thesis, Northern Arizona University.

Busby-Spera, C.J., 1983. Paleogeographic reconstruction of a submarine volcanic center: Geochronology, volcanology and sedimentology of the Mineral King Roof Pendant, Sierra Nevada, California. Princeton University.

Busby-Spera, C.J., 1984, Large-volume rhyolite ash flow eruptions and submarine caldera collapse in the Lower Mesozoic Sierra Nevada, California: Journal of Geophysical Research, v. 89, p. 8417, doi:10.1029/JB089iB10p08417.

Cao, W., Paterson, S., Memeti, V., Mundil, R., Anderson, J.L. and Schmidt, K., 2015, Tracking paleodeformation fields in the Mesozoic central Sierra Nevada arc: Implications for intra-arc cyclic deformation and arc tempos, Lithosphere, v. 7, no. 3, p. 296-320.

Cas, R.A.F., and Giordano, G., 2014, Submarine Volcanism: a Review of the Constraints, Processes and Products, and Relevance to the Cabo de Gata Volcanic Succession: Italian Journal of Geosciences, v. 133, p. 362–377, doi:10.3301/IJG.2014.46.

Cas, R.A.F., and Simmons, J.M., 2018, Why deep-water eruptions are so different from subaerial eruptions: Frontiers in Earth Science, v. 6, p. 198, doi:10.3389/feart.2018.00198.

Cole, J., Milner, D., and Spinks, K., 2005, Calderas and caldera structures: a review: Earth-Science Reviews, v. 69, p. 1–26, doi:10.1016/j.earscirev.2004.06.004.

Curtis, G.H., 1968, The Stratigraphy of the Ejecta from the 1912 Eruption of Mount Katmai and Novarupta, Alaska, in Geological Society of America Memoirs, Geological Society of America, v. 116, p. 153–210, doi:10.1130/MEM116-p153.

Dickinson, W.R., 1977, Paleozoic plate tectonics and the evolution of the Cordilleran continental margin.

Dobbs, S.C., Riggs, N.R., Marsaglia, K.M., González-León, C.M., Cecil, M.R., and Smith, M.E., 2021, The Permian Monos Formation: Stratigraphic and detrital zircon evidence for Permian Cordilleran arc development along the southwestern margin of Laurentia (northwestern Sonora, Mexico): Geosphere, v. 17, p. 520–537, doi:10.1130/GES02320.1.

Downey, W.S., and Lentz, D.R., 2006, Igneous Rock Associations 6. Modelling of deep submarine pyroclastic volcanism: A Review and New Results: GEOSCIENCE CANADA, v. 33, p. 20.

Druitt, T.H. and Sparks, R.S.J., 1984. On the formation of calderas during ignimbrite eruptions. Nature, 310(5979), pp.679-681.

Ducea, M., 2001, The California arc: Thick granitic batholiths, eclogitic residues lithosphericscale thrusting, and magmatic flare-ups: GSA Today, v. 11, p. 4-10.

Field, D.M. Episodic Sierran arc magmatism expressed in Mesozoic rocks of the Mount Morrison pendant, east-central Sierra Nevada, California: , p. 130.

Fiske, R.S. and Matsuda, T., 1964. Submarine equivalents of ash flows in the Tokiwa Formation, Japan. American Journal of Science, 262(1), pp.76-106.

Fiske, R.S., and Tobisch, O.T., 1978, Paleogeographic significance of volcanic rocks of the Ritter Range pendant, central Sierra Nevada, California. Pg 209-221.

Fiske, R.S., and Tobisch, O.T., 1994, Middle Cretaceous ash flow tuff and caldera-collapse deposit in the Minarets Caldera, east-central Sierra Nevada, California: Geological Society of America Bulletin, v. 106, p. 582–593, doi: 10.1130/00167606(1994)

Fiske, R.S., Naka, J., Iizasa, K., Yuasa, M., and Klaus, A., 2001, Submarine silicic caldera at the front of the Izu-Bonin arc, Japan: Voluminous seafloor eruptions of rhyolite pumice: Geological Society of America Bulletin, v. 113, p. 813–824, doi:10.1130/0016-7606(2001)

Gehrels, G.E., 2000, Introduction to detrital zircon studies of Paleozoic and Triassic strata in western Nevada and northern California, *in* Paleozoic and Triassic paleogeography and tectonics of western Nevada and Northern California, Geological Society of America, doi:10.1130/0-8137-2347-7.1.

Grimes, C.B., Wooden, J.L., Cheadle, M.J., and John, B.E., 2015, “Fingerprinting” tectono-magmatic provenance using trace elements in igneous zircon: Contributions to Mineralogy and Petrology, v. 170, p. 46, doi:10.1007/s00410-015-1199-3.

Hanson, B., S. Sorensen, M. Barton, and R. Fiske, 1993, Long-Term Evolution of Fluid-Rock Interactions in Magmatic Arcs: Evidence from the Ritter Range Pendant, Sierra Nevada, California, and Numerical Modeling, Journal of Petrology, v. 34, n. 1, p. 23-6.

Harker, A., 1909. The Natural History of Igneous Rocks. London, Metheuen, 384 pp.: Metheuen, London, p. 384.

Heaman, L.M., Bowins, R., and Crocket, J., 1990, The chemical composition of igneous zircon suites: implications for geochemical tracer studies: Geochimica et Cosmochimica Acta, v. 54, p. 1597–1607, doi:10.1016/0016-7037(90)90394-Z.

Heiken, G., Goff, F., Gardner, J.N., Baldridge, W.S., Hulen, J.B., Nielson, D.L. and Vaniman, D., 1990. The valles/toledo caldera complex, jemez volcanic field, New Mexico. Annual Review of Earth and Planetary Sciences, 18, p.27.

Hogan, J.P., 1993. Monomineralic glomerocrysts: textural evidence for mineral resorption during crystallization of igneous rocks. The Journal of geology, 101(4), pp.531-540.

Huber, N., and C. Rinehart, 1965, Geologic map of the Devils Postpiles quadrangle, Sierra Nevada, California, Map GQ-437: U.S. Geological Survey, Reston, Virginia.

Jackson, S.E., Pearson, N.J., Griffin, W.L., and Belousova, E.A., 2004, The application of laser ablation-inductively coupled plasma-mass spectrometry to in situ U–Pb zircon geochronology: Chemical Geology, v. 211, p. 47–69, doi:10.1016/j.chemgeo.2004.06.017.

Jones, E., and J. Rougvie, 2004, Structural and metamorphic history in the vicinity of Purple Lake, Mount Morrison roof pendant, California: Geological Society of America Abstracts and Programs, v. 36, n. 3, p. 42.

Kano, K., 2003, Subaqueous pumice eruptions and their products: A review, *in* White, J.D.L., Smellie, J.L., and Clague, D.A. eds., Geophysical Monograph Series, Washington, D. C., American Geophysical Union, v. 140, p. 213–229, doi:10.1029/140GM14.

Kelemen, P.B., Hanghøj, K. and Greene, A.R., 2014. One view of the geochemistry of subduction-related magmatic arcs, with an emphasis on primitive andesite and lower crust. Elsevier.

Klug, C., and Cashman, K.V., 1994, Vesiculation of May 18, 1980, Mount St. Helens magma: Geology, v. 22, p. 468, doi:10.1130/0091-7613(1994)022<0468:VOMMSH>2.3.CO;2.

Klug, C., and Cashman, K.V., 1996, Permeability development in vesiculating magmas: implications for fragmentation: Bulletin of Volcanology, v. 58, p. 87–100, doi:10.1007/s004450050128.

Kokelaar, P., 1986. Magma-water interactions in subaqueous and emergent basaltic. Bulletin of Volcanology, 48(5), pp.275-289.

Kylander-Clark, A.R.C., Hacker, B.R., and Cottle, J.M., 2013, Laser-ablation split-stream ICP petrochronology: Chemical Geology, v. 345, p. 99–112, doi:10.1016/j.chemgeo.2013.02.019.

Levy, D.A., Zuza, A.V., Haproff, P.J., and Odlum, M.L., 2021, Early Permian tectonic evolution of the Last Chance thrust system: An example of induced subduction initiation along a plate boundary transform: GSA Bulletin, v. 133, p. 1105–1127, doi:10.1130/B35752.1.

von Lichtan, I.J., White, J.D.L., Manville, V., and Ohneiser, C., 2016, Giant rafted pumice blocks from the most recent eruption of Taupo volcano, New Zealand: Insights from palaeomagnetic and textural data: Journal of Volcanology and Geothermal Research, v. 318, p. 73–88, doi:10.1016/j.jvolgeores.2016.04.003.

Lipman, P.W., 1984, The roots of ash flow calderas in western North America: Windows into the tops of granitic batholiths: Journal of Geophysical Research, v. 89, p. 8801, doi:10.1029/JB089iB10p08801.

Lodes, E., Riggs, N.R., Smith, M.E., and Stone, P., 2020, Cordilleran subduction initiation: retroarc timing and basinal response in the Inyo Mountains, eastern California (T. S. Abu-Alam, Ed.): Lithosphere, v. 2020, p. 9406113, doi:10.2113/2020/9406113.

Ludwig, K.R., 2012, Berkeley Geochronology Center Special Publication No. 5: , p. 75.

Mackaman-Lofland, C., Brand, B.D., Taddeucci, J., and Wohletz, K., 2014, Sequential fragmentation/transport theory, pyroclast size–density relationships, and the emplacement dynamics of pyroclastic density currents — A case study on the Mt. St. Helens (USA) 1980 eruption: Journal of Volcanology and Geothermal Research, v. 275, p. 1–13, doi:10.1016/j.jvolgeores.2014.01.016.

Manga, M. et al., 2018, The pumice raft-forming 2012 Havre submarine eruption was effusive: Earth and Planetary Science Letters, v. 489, p. 49–58, doi:10.1016/j.epsl.2018.02.025.

Mantle, G.W., and Collins, W.J., 2008, Quantifying crustal thickness variations in evolving orogens: Correlation between arc basalt composition and Moho depth: Geology, v. 36, p. 87, doi:10.1130/G24095A.1.

Mitchell, S.J., Houghton, B.F., Carey, R.J., Manga, M., Fauria, K.E., Jones, M.R., Soule, S.A., Conway, C.E., Wei, Z., and Giachetti, T., 2019, Submarine giant pumice: a window into the shallow conduit dynamics of a recent silicic eruption: Bulletin of Volcanology, v. 81, p. 42, doi:10.1007/s00445-019-1298-5.

Morgan, B.A. and Rankin, D.W., 1972, Major structural break between Paleozoic and Mesozoic rocks in the eastern Sierra Nevada, California. Geological Society of America Bulletin, 83(12), pp.3739-3744.

Murch, A.P., White, J.D.L., Barreyre, T., Carey, R.J., Mundana, R., and Ikegami, F., 2020, Volcaniclastic dispersal during submarine lava effusion: The 2012 eruption of Havre Volcano, Kermadec arc, New Zealand: Frontiers in Earth Science, v. 8, p. 237, doi:10.3389/feart.2020.00237.

Nokleberg, W., and R. Kistler, 1980, Paleozoic and Mesozoic deformations in the central Sierra Nevada, California: United States Geological Survey Professional Paper 1145.

Paterson, S.R., and Ducea, M.N., 2015, Arc Magmatic Tempos: Gathering the Evidence: Elements, v. 11, p. 91–98, doi:10.2113/gselements.11.2.91.

Reimink, J.R., Davies, J.H.F.L., Bauer, A.M., and Chacko, T., 2020, A comparison between zircons from the Acasta Gneiss Complex and the Jack Hills region: Earth and Planetary Science Letters, v. 531, p. 115975, doi:10.1016/j.epsl.2019.115975.

Rinehart, C.D., Ross, D.C., and Pakiser, L.C., 1964, Geology and Mineral DepOsits of the Mount Morrison Quadrangle Sierra Nevada, California: , p. 112.

Rotella, M.D., Wilson, C.J.N., Barker, S.J., and Wright, I.C., 2013, Highly vesicular pumice generated by buoyant detachment of magma in subaqueous volcanism: Nature Geoscience, v. 6, p. 129–132, doi:10.1038/ngeo1709.

Russell, S., and W. Nokleberg, 1977, Superimposition and timing of deformations in the Mount Morrison roof pendant and in the central Sierra Nevada, California: Geologic Society of America Bulletin, v. 88, i. 3, p. 334-345.

Saleeby, J., 2011, Geochemical mapping of the Kings-Kaweah ophiolite belt, California—Evidence for progressive mélange formation in a large offset transform-subduction initiation environment, in Mélanges: Processes of Formation and Societal Significance, Geological Society of America, doi:10.1130/2011.2480(02).

Saleeby, J., and G. Dunne, 2015, Temporal and tectonic relations of Early Mesozoic arc magmatism, southern Sierra Nevada, California: Geological Society of America Special Papers, v. 513.

Savage, J.A., 2021, Mafic magmatism, subaqueous volcanism, and dome growth in the early Triassic Sierran arc, east-central, Sierra Nevada, California: Thesis, Northern Arizona University.

Schweickert, R.A., and Cowan, D.S., 1975, Early Mesozoic tectonic evolution of the western Sierra Nevada, California. Geological Society of America Bulletin, v. 86, no. 10, p. 1329-1336.

Schweickert, R., and M. Lahren, 2006, Geologic evolution of Saddlebag Lake pendant, eastern Sierra Nevada, California: Tectonic implications, in Girty, G., and Cooper, J.D., eds., Using stratigraphy, sedimentology, and geochemistry to unravel the geologic history of the southwestern Cordillera: Pacific Section: Society for Sedimentary Geology, p. 27-56.

de Silva, S., N. Riggs, and A. Barth, 2015, Quickening the pulse: fractal tempos in continental magmatism: Elements, v. 11, p. 113-118.

Sláma, J. et al., 2008, Plešovice zircon — A new natural reference material for U–Pb and Hf isotopic microanalysis: Chemical Geology, v. 249, p. 1–35, doi:10.1016/j.chemgeo.2007.11.005.

Smith, R.L., 1979, Ash-flow magmatism: Geological Society of America, Special Paper 180.

Sorensen, S.S. and Grossman, J.N., 1993. Accessory minerals and subduction zone metasomatism: a geochemical comparison of two mélanges (Washington and California, USA). Chemical Geology, 110(1-3), pp.269-297.

Sorensen, S., G. Dunne, R. Hanson, M. Barton, J. Becker, O. Tobisch, and R Fiske, 1998, From Jurassic shores to Cretaceous plutons: Geochemical evidence for paleoalteration environments of metavolcanic rocks, eastern California: Geological Society of America Bulletin, v. 110, n. 3, p. 326-343.

Sruoga, P., M. Japas, F. Salani, and L. Kleiman, 2013, La Peligrosa caldera: A key event during the Jurassic ignimbrite flare-up in southern Patagonia, Argentina: Journal of Volcanology and Geothermal Research, v. 269. P. 44-56.

Stern, R., 2004, Subduction initiation: spontaneous and induced: Earth and Planetary Science Letters, v. 226, p. 275–292, doi:10.1016/S0012-821X(04)00498-4.

Stevens, C.H., Stone, P., Dunne, G.C., Greene, D.C., Walker, J.D. and Swanson, B.J., 1997. Paleozoic and Mesozoic evolution of east-central California. *International Geology Review*, *39*(9), pp.788-829.

Stevens, C.H. and Stone, P., 2005. Structure and regional significance of the Late Permian (?) Sierra Nevada–Death Valley thrust system, east-central California. Earth-Science Reviews, 73(1-4), pp.103-113.

Stix, J., 1991. Subaqueous, intermediate to silicic-composition explosive volcanism: a review. Earth-Science Reviews, 31(1), pp.21-53.

Stone, P., Barth, A.P., Wooden, J.L., Fohey-Breting, N.K., Vazquez, J.A. and Priest, S.S., 2013. Geochronologic and Geochemical Data from Mesozoic Rocks in the Black Mountains Area Northeast of Victorville, San Bernardino County, California (p. 31). US Department of the Interior, US Geological Survey.

Sundell, K.E., George, S.W.M., Carrapa, B., Gehrels, G.E., Ducea, M.N., Saylor, J.E., and Pepper, M., 2022, Crustal thickening of the northern central Andean plateau inferred From trace elements in zircon: Geophysical Research Letters, v. 49, doi:10.1029/2021GL096443.

Vermeesch, P., 2018, IsoplotR: A free and open toolbox for geochronology: Geoscience Frontiers, v. 9, p. 1479–1493, doi:10.1016/j.gsf.2018.04.001.

Walker, G.P., 1984. Downsag calderas, ring faults, caldera sizes, and incremental caldera growth. Journal of Geophysical Research: Solid Earth, 89(B10), pp.8407-8416.

Walker, J.D., 1988, Permian and Triassic rocks of the Mojave Desert and their implications for timing and mechanisms of continental truncation, Tectonics, v. 7, n. 3, p. 685-709.

Wiedenbeck, M. et al., 2004, Further Characterisation of the 91500 Zircon Crystal: Geostandards and Geoanalytical Research, v. 28, p. 9–39, doi:10.1111/j.1751-908X.2004.tb01041.x.

Williams, H., 1941. Calderas and their origin. Bull. Geol. Sci. Dep., 25, pp.239-346.

APPENDIX A

SAMPLE NUMBER	DESCRIPTION
AGNEW MEADOWS AREA	
KB 080521-1	<u>*Hand sample*</u>*:* Lower grey lithic tuff. Sample contains 2 cm-long elongate lithic fragments and grey and tan pumice pieces also 2 cm long. This sample also has 10% quartz phenocrysts 1-2 mm in an aphanitic, altered groundmass, as evidenced by a sugary, altered appearance. Slight foliation is defined by the elongate pumice pieces and lithic fragments deformed around quartz phenocrysts. <u>*Thin section*</u>*:* Fine-grained groundmass with sericite alteration makes up 85% of the rock. Phenocrysts include: 4% subhedral to anhedral quartz (1-2 mm), 0.5% subhedral to anhedral plagioclase (0.5 mm), 1% anhedral K-spar with sericite alteration (1 mm), and ≤1% subhedral oxides. Rock also contains 2% pumice pieces (1 mm) and 2% lithic fragments (1 mm) composed of 85% quartz and 15% plagioclase.
KB 080521-3	<u>*Hand sample*</u>*:* Lower grey lithic tuff. Light grey with 10% feldspar phenocrysts (1 mm) and 3% quartz phenocrysts (1 mm), in an aphanitic groundmass. <u>*Thin section*</u>*:* Fine-grained groundmass containing quartz and feldspars with epidote and sericite alteration throughout makes up 25% of the rock. Phenocrysts include: 2% subhedral quartz (1 mm), 1% embayed, anhedral quartz (0.5 mm), and 2% K-spar with sericite

SAMPLE NUMBER	**DESCRIPTION**
	alteration (1-2 mm). Also contains 60% very elongate pumice pieces (1-4 mm long) and 5% quartzite clasts (3 mm long).
KB 080721-1A	*Hand sample:* Lower grey lithic tuff. Tuff is medium grey and contains 10% quartz phenocrysts (1-2 mm) and 15% dark grey pumice clasts (2-3 mm) in an aphanitic groundmass. The pumice are slightly deformed around the quartz phenocrysts, defining a slight foliation.
KB 081221-2	*Hand sample:* Lower grey lithic tuff. Light grey with 5% quartz phenocrysts (1 mm) and 2% feldspar phenocrysts (1 mm) in an aphanitic groundmass. It also contains 1%, 1-3 mm grey pumices.
KB-080721-1B	*Hand sample:* Grey clast in Lower grey lithic tuff. Dark grey with a mm-scale diffuse, flame-like boundary with the host tuff. 5%, < 1 mm, equant to elongate quartz phenocrysts in an aphanitic groundmass. The boundary between the clast and the surrounding lower grey lithic tuff is ~ 5 mm and grades from the grey clast to a white boundary zone, to the medium grey lower grey lithic tuff. The clast is less resistant than the overall rock, such that the phenocrysts in the clast are more resistant to weathering within the clast than in the *Thin section:* Fine-grained groundmass containing quartz and mica makes up 85% of the rock. Phenocrysts include: 2% subhedral quartz (1 mm), 3% subhedral quartz (0.5 mm), 0.5% subhedral quartz (2 mm), and 1% anhedral K-spar with sericite alteration (1 mm). Also contains 6% elongate pumice pieces (2 mm) that have altered to mica and define a slight foliation around the phenocrysts.

SAMPLE NUMBER	**DESCRIPTION**
KB 080521-2A	*Hand sample:* Pumice conglomerate matrix. Sample is dark grey with 5%, 0.5-1 mm quartz phenocrysts in a grey, sugary groundmass. *Thin section:* Fine-grained groundmass of quartz crystals and sericite and epidote alteration make up 85% of the rock. Phenocrysts include: 4% subhedral to anhedral quartz (0.5 mm-2mm) and ≤ 1% anhedral K-spar with sericite alteration (0.5 mm). This sample also contains 10% fiamme (0.5-2 mm) deformed around phenocrysts.
KB 080521-2B	*Hand sample:* Pumice conglomerate clast. Clast is white with 5% quartz phenocrysts (1 mm) and 5% elongate pumice pieces in an aphanitic groundmass. *Thin section:* Fine-grained groundmass containing quartz makes up 85% of the rock. Phenocrysts include a variety of sizes of quartz: 0.1 mm-0.5 mm (4%) and 1 mm-2 mm (2%); and 0.1 mm K-spar with sericite alteration makes up 2% of the rock. Also contains 5% undeformed pumice pieces (1 mm).
KB 080921-2	*Hand sample:* Pumice conglomerate clast. White-tan pumice containing 5% quartz phenocrysts 1-2 mm, 3% feldspar phenocrysts 1 mm, 5% elongate pumiceous fragments 2-4 mm long, with 85% white aphanitic groundmass. *Thin section:* Microcrystalline groundmass containing quartz and feldspars with epidote and sericite alteration throughout makes up

SAMPLE NUMBER	**DESCRIPTION**
	88% of the rock. Phenocrysts include: 2% subhedral quartz (1-2 mm), 2% euhedral quartz (0.25 mm), and 1% subhedral K-spar (0.25 mm) with sericite alteration. Also includes 7% pumiceous fragments (1 mm) that have altered to fine mica and define a foliation around phenocrysts.
KB 080921-1	_Hand sample_: Pumice conglomerate clast, including dark interior. Elongate pumice clast portion is tan-white with 4 % quartz phenocrysts 1 mm in diameter and, 2 % feldspar phenocrysts 1 mm, with >90 % aphanitic, white groundmass. Dark grey-brown interior has 1% quartz phenocrysts 0.5 mm in an aphanitic dark grey groundmass. _Thin section_: Fine-grained groundmass with 2% quartz (1 mm), 1% feldspar (1 mm), 1% hornblende (1 mm), and 1% oxide phenocrysts (1 mm). Sericite and mica alteration throughout make mineral identification difficult. The contact between the interior and the exterior is sharp.
KB 080821-3	_Hand sample_: Pumice conglomerate from an area with low clast density. The clast is light grey to white and contains 7 % quartz phenocrysts 1-2mm and 1-2 mm long elongate tan pumice pieces in a white groundmass. _Thin section_: Fine-grained groundmass containing quartz and feldspars with epidote and sericite alteration makes up 75% of the rock. Phenocrysts include 4% subhedral quartz (2 mm), 3% euhedral

SAMPLE NUMBER	DESCRIPTION
	to subhedral quartz (0.5 mm), and 1% subhedral K-spar with sericite alteration. Also contains 17% pumiceous fragments ranging in size from 1-3 mm that have altered to fine mica and define a foliation around phenocrysts.
KB 080821-1	<u>Hand sample</u>*:* Grey tuff SE of the pumice conglomerate. Sample contains 7% quartz phenocrysts (1-2 mm), 1% K-spar phenocrysts (2 mm), and 20% 1-3 cm-long elongate dark grey pumice pieces that define a weak foliation. The groundmass is grey and aphanitic. <u>*Thin section*</u>: Microcrystalline groundmass containing quartz, feldspars, and micas with epidote and sericite alteration makes up 80% of the rock. Phenocrysts include: 2% subhedral quartz (3 mm), 2% euhedral quartz (1 mm), 2% magnetite (0.5 mm), 4% anhedral K-spar with sericite alteration (1-2 mm), and 6% altered mafic minerals (0.5 mm).
KB 080821-2	<u>Hand sample</u>*:* Grey tuff SE of the pumice conglomerate. Sample is dark grey with 1-2 mm quartz phenocrysts and rare 2-4 mm feldspar phenocrysts in an aphanitic groundmass. Weak foliation of grey pumice pieces around subhedral quartz phenocrysts. <u>*Thin section*</u>: Microcrystalline groundmass containing quartz, feldspars, and micas with epidote and sericite alteration makes up 80% of the rock. Phenocrysts include: 2% subhedral quartz (3 mm), 2% euhedral quartz (1 mm), 2% magnetite (0.5 mm), 4% anhedral K-

SAMPLE NUMBER	DESCRIPTION
	spar with sericite alteration (1-2 mm), 6% altered mafic minerals (0.5 mm), and 4% anhedral K-spar with sericite alteration (≤ 1 mm).
KB 080921-3	*Hand sample:* upper grey lithic tuff. Fine- to medium-grained grey tuff containing rare tan elongate pumice clasts 2-4 mm long and rare grey elongate lithic fragments 2-15 mm long. The rock also contains equant quartz phenocrysts (5%, 1-2 mm) and 6% equant feldspar phenocrysts ranging in size from 1 mm to 3 mm. *Thin section:* Fine-grained groundmass containing quartz and feldspars with epidote and sericite alteration makes up 80% of the rock. Phenocrysts include: 6% subhedral to anhedral quartz (1-2 mm), 3% anhedral, fractured K-spar with sericite alteration (1-2 mm), and 1% fractured K-spar glomerocrysts (4 mm). Also contains 5% fine-grained quartzite fragments (2-5 mm long) and 5% pumice fragments deformed around phenocrysts.
KB 080321-1	*Hand sample:* Upper grey lithic tuff. Rock contains 25% 1-2 mm quartz phenocrysts in a grey aphanitic groundmass. Also includes rare lenses (3 mm x 5 mm) of very dark grey, aphanitic material and mm-scale layers with 15% quartz (1 mm) and 15% feldspar phenocrysts (1 mm), and other rare lenses with 1 mm-long tan elongate pumice fragments. *Thin section:* Fine-grained groundmass containing quartz and feldspars with epidote and sericite alteration makes up 85% of the rock. Phenocrysts include: 3% subhedral to anhedral quartz 0.25 mm

SAMPLE NUMBER	**DESCRIPTION**
	- >1 mm, 1% anhedral plagioclase (0.5-0.75 mm), and 1% anhedral K-spar with sericite alteration (0.5 mm). Sample also includes 5%, 2.5 mm-long pumice pieces deformed around feldspar and quartz phenocrysts, and 5% lithic fragments that are <0.25 mm and primarily composed of quartz.
KB 081121-1	*Hand sample:* Upper grey lithic tuff. Fine- to medium-grained grey tuff containing rare tan elongate pumice clasts 2-3 mm in length, rare grey elongate lithic fragments 2-3 mm in length, and very rare elongate quartzite clasts 4 mm long. Also contains phenocrysts of quartz (5%, 1 mm), feldspars (4%, 1 mm), and ribbons of biotite (6%, 1-2 mm long), in an aphanitic, grey groundmass that makes up 85% of the rock.
KB 081021-1	*Hand sample:* Tuff of San Joaquin Mountain. Light grey tuff with a weak foliation defined by dark grey to black wispy pumices 1-3 mm long (10%), 7% quartz phenocrysts 1-2 mm, and 10% feldspar phenocrysts 2-3 mm in an aphanitic groundmass. *Thin section:* Fine-grained groundmass containing quartz and feldspars with epidote and sericite alteration throughout makes up 80% of the rock. Phenocrysts include 5% subhedral to anhedral, fractured quartz (2-3 mm), 3% subhedral plagioclase (2-3 mm), and 2% subhedral K-spar (1-2 mm) with sericite alteration. Also contains 3% quartzite lithic fragments (2 mm) and 7% epidote- and mica-altered pumice fragments (2-4 mm long) folded around phenocrysts.

SAMPLE NUMBER	**DESCRIPTION**
KB 081021-2	*Hand sample:* Quartzite-rich lithic tuff north of Agnew Meadows. This tuff includes a variety of dark black irregular lithic fragments approximately 3 cm in the longest dimension. Also includes 3 cm-long porphyritic ellipsoids containing 5% quartz phenocrysts (1 mm) in a dark, aphanitic groundmass. Dark grey aphanitic lithic fragments are rare and measure 1-2 cm long with a few 5-7 cm long. Very rare ellipsoid quartzite clasts measure more than 15 cm in length. Dark grey wispy pumices measure less than 1 cm long and define a weak foliation. The matrix contains 7% quartz phenocrysts (1 mm) and 10% feldspar phenocrysts (1-2 mm). *Thin section:* Microcrystalline groundmass containing quartz and sericite alteration makes up 80% of the rock. Phenocrysts include 3% euhedral to subhedral, fractured quartz (1-2 mm), 2% euhedral to subhedral plagioclase (1-2 mm), and 1% anhedral K-spar with moderate sericite alteration (1-2 mm). Also includes 3% glomerocrysts composed of feldspar pseudomorphs (1-2 mm), and 16% pumice pieces (3-5 mm long) deformed around phenocrysts.
KB 081221-1	*Hand sample:* Lithic-rich tuff northwest of Pumice Conglomerate. This tuff has abundant elongate tan to dark grey lithic fragments 2 mm – 6 cm long. These fragments are primarily quartzite and pumice, with rare aphanitic grey lithic fragments 2 – 7 cm long, while the pumice pieces are maximum 2 cm long. The matrix is composed of 10% quartz phenocrysts (1-2 mm) and 10% feldspar phenocrysts (1 mm) in an

SAMPLE NUMBER	DESCRIPTION
	aphanitic grey groundmass. A weak foliation is defined by the pumice and lithic fragments. *Thin section:* Fine-grained groundmass containing quartz and feldspars with epidote and sericite alteration throughout makes up 80% of the rock. Phenocrysts throughout include: 2% subhedral quartz (1-2 mm), 3% K-spar with sericite alteration (1-3 mm), and 1% subhedral, altered hornblende (1-2 mm). Also contains 12% pumices 2-7 mm in length, which are wrapped around phenocrysts, and 2% altered mafic glomerocrysts (2 mm).
KB 081021-3	*Hand sample:* Quartzite conglomerate. This unit contains a variety of poorly sorted lithic fragments, elongate quartzite clasts 1 cm – 10 cm long in a grey matrix. The matrix is composed of a variety of poorly sorted lithic fragments ranging in lithology from quartzite to pumice to aphanitic grey fragments, all measuring <1 mm to 5 cm. *Thin section:* Microcrystalline groundmass containing quartz and sericite alteration makes up 85% of the rock. Phenocrysts include: 2% subhedral quartz (1 mm) and 1% K-spar with sericite alteration (0.5 mm). Also contains 7% quartzite lithic clasts (2mm-1.5 cm), 2% clasts composed of calcite (3 mm), and 3% pumice pieces (2-3 mm) wrapped around lithic clasts and phenocrysts.

SAMPLE NUMBER	DESCRIPTION
SKELTON LAKE	
KB 080621-1	*Hand sample:* Tuff of Skelton Lake at Skelton Lake. Tuff is light grey with 15% quartz phenocrysts ranging in size from 0.5 to 2 mm, 1% plagioclase phenocrysts < 1 mm, and <1% biotite crystals 0.5 mm in size in an aphanitic, altered groundmass. Lithic fragments and grey pumice pieces are abundant and vary in size from 1 mm – 12 mm long ellipsoids, with most less than 3 mm long. The edges of the pumice pieces are irregular. The lithic fragments are dark quartzite and unspecified Paleozoic metasedimentary rocks. *Thin section:* Fine-grained groundmass containing quartz and feldspars with epidote and sericite alteration throughout makes up 84% of the rock. Phenocrysts include: 5% subhedral quartz (4 mm), 5% subhedral quartz (1-2.5 mm), 3% epidote alteration, 3% anhedral K-spar with sericite alteration (1-2 mm), and 1% subhedral, altered plagioclase (2 mm).
KB 080621-2	*Hand sample:* Porphyritic clast in tuff of Skelton Lake at Skelton Lake with black with 1-4 mm glomerocrysts composed of equal parts quartz and feldspar phenocrysts, each 1-2 mm. The matrix around the glomerocrysts contains 0.5-2 mm hornblende phenocrysts (7%) in an aphanitic groundmass. *Thin section:* Cryptocrystalline groundmass with sericite, epidote, and chlorite alteration makes up 80% of the rock. Phenocrysts include: 5%

SAMPLE NUMBER	DESCRIPTION
	subhedral quartz (1-4 mm), 2% subhedral, altered plagioclase (2.5 mm), and 1% subhedral microcline (2 mm). Also contains 10% glomerocrysts (2.5 mm) containing fine-grained quartz (0.25 mm).
RED AND WHITE SPUR	
KB 081521-1	<u>Hand sample</u>*:* Lithic-rich tuff facies at Red and White Spur. Tuff is grey with abundant dark grey to black lithic fragments and pumice pieces. Lithic fragments range from <1 cm – 10 cm long. Pumices are vesicular and vary in size from <1 cm – 15 cm long. Most are elongate, but some are irregularly shaped. Some are grey with 7% white phenocrysts (1-2 mm). The groundmass contains 10% quartz phenocrysts (1-3 mm) and 7% feldspar phenocrysts (1-2 mm) in a light grey aphanitic groundmass. <u>Thin section</u>*:* Fine-grained groundmass containing quartz and feldspars with epidote and sericite alteration throughout makes up 90% of the rock. Phenocrysts throughout include: 5% subhedral, fractured quartz (2-4 mm), 2% subhedral K-spar with sericite alteration (2-3 mm), and 3% subhedral hornblende (1 mm).
KB 081521-2	<u>Hand sample</u>*:* Fine-grained tuff at Red and White Spur. Tuff has abundant lithic fragments. Most of the lithic fragments are dark grey and range from 1 to 7 cm long. Most are elongate, but some are irregular shapes. Most are aphanitic and grey, but the minority are vesicular and contain <5% quartz phenocrysts (1 mm). The matrix

SAMPLE NUMBER	DESCRIPTION
	contains 15% quartz phenocrysts (1-3 mm) and 15% feldspar phenocrysts (1-3 mm). *Thin section:* Fine to medium-grained groundmass containing quartz, feldspars, and biotite with epidote and sericite alteration throughout makes up 90% of the rock. Phenocrysts throughout include: 5% subhedral, fractured quartz (2-5 mm), 4% subhedral K-spar (1-2 mm), and 1% plagioclase (1 mm). Also contains 1% altered mafic crystals (3-5 mm).
KB 081521-3	*Hand sample:* “Conglomerate facies” at Red and White Spur. Sample is light grey, non-foliated, and contains 10% quartz phenocrysts ranging in size from 0.5 to 4 mm in a light grey, aphanitic groundmass. *Thin section:* Fine to medium-grained groundmass containing quartz, feldspar, and biotite with epidote and sericite alteration throughout makes up 90% of the rock. Phenocrysts throughout include: 8% subhedral to anhedral quartz (2-5 mm), 2% subhedral plagioclase (1-2 mm), and 0.5% subhedral K-spar with sericite alteration (1 mm). Also includes rare glomerocrysts containing 95% quartz (1 mm) and 5% biotite (1 mm).

APPENDIX B

Sample	^{207}Pb/^{235}U	^{207}Pb/^{235}U 2σ error	^{206}Pb/^{238}U	^{206}Pb/^{238}U 2σ error	^{238}U/^{206}Pb	^{238}U/^{206}Pb 2σ error	^{207}Pb/^{206}Pb	^{207}Pb/^{206}Pb 2σ error	Concor-dance	Discor-dance
KB081121-1-1	0.250	0.003	0.0342	0.0003	29.24	0.27	0.053	0.001	0.67	0.96
KB081121-1-2	0.233	0.002	0.0337	0.0002	29.66	0.15	0.050	0.000	1.06	1.01
KB081121-1-3	0.239	0.002	0.0333	0.0002	30.00	0.16	0.052	0.000	0.76	0.97
KB081121-1-4	0.241	0.003	0.0344	0.0003	29.08	0.25	0.050	0.000	1.00	0.99
KB081121-1-5	0.241	0.003	0.0347	0.0003	28.84	0.22	0.051	0.000	0.99	1.00
KB081121-1-6	0.240	0.003	0.0346	0.0004	28.90	0.31	0.050	0.000	1.11	1.00
KB081121-1-7	0.245	0.005	0.0347	0.0003	28.84	0.21	0.051	0.001	0.89	0.99
KB081121-1-8	0.238	0.003	0.0341	0.0003	29.29	0.29	0.050	0.000	1.00	1.00
KB081121-1-9	0.242	0.004	0.0345	0.0003	29.03	0.24	0.051	0.001	0.96	0.99
KB081121-1-10	0.243	0.005	0.0348	0.0005	28.77	0.41	0.050	0.001	1.02	1.00
KB081121-1-11	0.233	0.004	0.0342	0.0003	29.27	0.23	0.049	0.001	1.32	1.02
KB081121-1-12	0.238	0.004	0.0343	0.0006	29.18	0.51	0.050	0.000	1.10	1.00
KB081121-1-13	0.250	0.004	0.0357	0.0006	28.00	0.43	0.050	0.000	1.08	1.00
KB081121-1-14	0.242	0.003	0.0350	0.0003	28.56	0.24	0.050	0.000	1.11	1.01
KB081121-1-15	0.241	0.002	0.0344	0.0002	29.07	0.16	0.051	0.000	0.98	0.99
KB081121-1-16	0.237	0.002	0.0339	0.0002	29.52	0.18	0.050	0.000	1.02	0.99
KB081121-1-17	0.239	0.003	0.0345	0.0003	28.97	0.27	0.050	0.000	1.11	1.01
KB081121-1-18	0.243	0.003	0.0347	0.0004	28.83	0.32	0.051	0.000	0.98	1.00
KB081121-1-19	0.240	0.003	0.0346	0.0003	28.91	0.27	0.051	0.000	1.01	1.00
KB081121-1-20	0.244	0.004	0.0351	0.0003	28.47	0.24	0.051	0.001	1.01	1.00
KB081121-1-21	0.238	0.003	0.0339	0.0002	29.50	0.21	0.051	0.000	0.96	0.99
KB081121-1-22	0.245	0.003	0.0343	0.0003	29.16	0.28	0.052	0.000	0.83	0.98
KB081121-1-23	0.239	0.002	0.0343	0.0003	29.12	0.22	0.050	0.000	1.09	1.00
KB081121-1-24	0.234	0.002	0.0335	0.0003	29.82	0.23	0.050	0.000	1.01	1.00
KB081121-1-25	0.247	0.004	0.0331	0.0004	30.26	0.33	0.054	0.001	0.55	0.94
KB081121-1-26	0.241	0.003	0.0344	0.0004	29.09	0.31	0.051	0.000	0.95	1.00
KB081121-1-27	0.236	0.003	0.0341	0.0003	29.33	0.23	0.050	0.000	1.11	1.01
KB081121-1-28	0.249	0.003	0.0358	0.0003	27.93	0.27	0.050	0.000	1.09	1.00
KB081121-1-30	0.241	0.002	0.0343	0.0002	29.17	0.20	0.051	0.000	0.97	0.99
KB081121-1-31	0.241	0.002	0.0346	0.0003	28.94	0.27	0.051	0.000	1.00	1.00

Table 2a: U-Pb analytical data for 79 zircon from the upper grey lithic tuff in Agnew Meadows.

Sample	$^{207}Pb/^{235}U$	$^{207}Pb/^{235}U$ 2_σ error	$^{206}Pb/^{238}U$	$^{206}Pb/^{238}U$ 2_σ error	$^{238}U/^{206}Pb$	$^{238}U/^{206}Pb$ 2_σ error	$^{207}Pb/^{206}Pb$	$^{207}Pb/^{206}Pb$ 2_σ error	Concor-dance	Discor-dance
KB081121-1-32	0.241	0.002	0.0336	0.0002	29.81	0.20	0.052	0.000	0.75	0.97
KB081121-1-33	0.241	0.002	0.0345	0.0003	29.02	0.21	0.051	0.000	0.98	1.00
KB081121-1-34	0.239	0.002	0.0341	0.0003	29.36	0.23	0.051	0.000	0.94	0.99
KB081121-1-35	0.238	0.002	0.0340	0.0003	29.40	0.22	0.050	0.000	1.04	1.00
KB081121-1-36	0.244	0.002	0.0347	0.0003	28.84	0.25	0.051	0.000	0.97	0.99
KB081121-1-37	0.238	0.003	0.0337	0.0003	29.70	0.26	0.051	0.000	0.93	0.99
KB081121-1-38	0.236	0.003	0.0337	0.0004	29.67	0.31	0.050	0.000	0.98	0.99
KB081121-1-39	0.235	0.003	0.0340	0.0003	29.46	0.23	0.050	0.000	1.09	1.00
KB081121-1-40	0.239	0.002	0.0341	0.0002	29.30	0.20	0.050	0.000	1.01	1.00
KB081121-1-41	0.263	0.006	0.0362	0.0007	27.60	0.53	0.052	0.001	0.75	0.97
KB081121-1-42	0.242	0.003	0.0347	0.0003	28.79	0.21	0.050	0.000	1.02	1.00
KB081121-1-43	0.243	0.002	0.0342	0.0003	29.28	0.21	0.051	0.000	0.87	0.98
KB081121-1-44	0.243	0.003	0.0347	0.0003	28.79	0.27	0.051	0.000	0.99	1.00
KB081121-1-45	0.242	0.003	0.0345	0.0004	28.99	0.31	0.051	0.000	0.97	0.99
KB081121-1-46	0.244	0.002	0.0346	0.0003	28.91	0.21	0.051	0.000	0.92	0.99
KB081121-1-47	0.249	0.009	0.0354	0.0013	28.25	1.04	0.050	0.000	1.03	1.00
KB081121-1-48	0.247	0.005	0.0350	0.0006	28.59	0.48	0.051	0.000	1.00	0.99
KB081121-1-49	0.244	0.002	0.0347	0.0004	28.82	0.32	0.051	0.000	1.00	0.99
KB081121-1-50	0.246	0.003	0.0346	0.0003	28.89	0.27	0.051	0.001	0.89	0.98
KB081121-1-51	0.248	0.004	0.0353	0.0004	28.36	0.34	0.051	0.000	0.98	0.99
KB081121-1-52	0.246	0.004	0.0353	0.0003	28.37	0.25	0.050	0.000	1.07	1.00
KB081121-1-53	0.245	0.003	0.0348	0.0003	28.78	0.21	0.051	0.000	0.94	0.99
KB081121-1-54	0.244	0.002	0.0345	0.0003	28.99	0.23	0.051	0.000	0.87	0.99
KB081121-1-55	0.239	0.003	0.0342	0.0004	29.25	0.32	0.050	0.000	1.06	1.00
KB081121-1-56	0.244	0.002	0.0346	0.0002	28.93	0.20	0.051	0.000	0.91	0.99
KB081121-1-57	0.242	0.002	0.0346	0.0003	28.94	0.24	0.050	0.000	1.05	0.99
KB081121-1-58	0.245	0.003	0.0350	0.0004	28.59	0.29	0.050	0.000	1.04	1.00
KB081121-1-59	0.238	0.003	0.0340	0.0002	29.40	0.20	0.050	0.000	1.03	0.99

Table 2b: U-Pb analytical data for 79 zircon from the upper grey lithic tuff in Agnew Meadows.

Sample	$^{207}Pb/^{235}U$	$^{207}Pb/^{235}U$ 2_{σ} error	$^{206}Pb/^{238}U$	$^{206}Pb/^{238}U$ 2_{σ} error	$^{238}U/^{206}Pb$	$^{238}U/^{206}Pb$ 2_{σ} error	$^{207}Pb/^{206}Pb$	$^{207}Pb/^{206}Pb$ 2_{σ} error	Concor-dance	Discor-dance
KB081121-1-61	0.246	0.002	0.0349	0.0002	28.65	0.17	0.051	0.001	0.94	0.99
KB081121-1-62	0.250	0.002	0.0338	0.0002	29.62	0.20	0.053	0.000	0.62	0.94
KB081121-1-63	0.243	0.003	0.0343	0.0004	29.15	0.32	0.051	0.000	0.94	0.98
KB081121-1-64	0.258	0.004	0.0369	0.0003	27.10	0.23	0.051	0.000	1.02	1.00
KB081121-1-65	0.254	0.004	0.0361	0.0003	27.69	0.23	0.051	0.001	0.99	0.99
KB081121-1-66	0.241	0.003	0.0345	0.0004	29.02	0.35	0.050	0.000	1.02	0.99
KB081121-1-67	0.240	0.003	0.0342	0.0003	29.27	0.28	0.050	0.000	1.04	0.99
KB081121-1-68	0.255	0.006	0.0353	0.0005	28.36	0.43	0.052	0.001	0.83	0.97
KB081121-1-69	0.242	0.004	0.0340	0.0004	29.38	0.38	0.051	0.000	0.87	0.98
KB081121-1-70	0.239	0.003	0.0341	0.0004	29.33	0.31	0.050	0.000	1.03	0.99
KB081121-1-71	0.910	0.220	0.0401	0.0020	24.94	1.24	0.155	0.033	0.11	0.41
KB081121-1-72	0.248	0.003	0.0347	0.0003	28.79	0.28	0.051	0.000	0.84	0.98
KB081121-1-73	0.244	0.003	0.0347	0.0004	28.79	0.36	0.050	0.000	1.02	0.99
KB081121-1-74	0.257	0.003	0.0345	0.0003	29.00	0.28	0.053	0.000	0.64	0.94
KB081121-1-76	0.250	0.003	0.0351	0.0003	28.53	0.28	0.052	0.000	0.84	0.98
KB081121-1-77	0.251	0.008	0.0354	0.0009	28.22	0.73	0.051	0.000	0.95	0.99
KB081121-1-78	0.243	0.008	0.0344	0.0011	29.07	0.93	0.051	0.001	0.97	0.99
KB081121-1-79	0.241	0.004	0.0342	0.0004	29.23	0.32	0.051	0.000	0.93	0.99
KB081121-1-80	0.245	0.003	0.0348	0.0002	28.74	0.20	0.051	0.000	0.97	0.99

Table 2c: U-Pb analytical data for 79 zircon from the upper grey lithic tuff in Agnew Meadows.

Sample	Age (Ma) ^{207}Pb/^{235}U	207/235 age 2σ error	Age (Ma) ^{206}Pb/^{238}U	206/238 age 2σ error	Age (Ma) ^{208}Pb/^{232}U	208/232 age 2σ error	Age (Ma) ^{207}Pb/^{206}Pb	207/206 age 2σ error
KB081121-1-1	226	3	217	2	219	3	321	24
KB081121-1-2	212	2	214	1	210	2	200	18
KB081121-1-3	218	2	211	1	208	2	277	15
KB081121-1-4	219	3	218	2	216	3	216	14
KB081121-1-5	219	2	220	2	217	2	221	16
KB081121-1-6	218	3	219	2	218	4	197	14
KB081121-1-7	222	4	220	2	219	3	244	30
KB081121-1-8	217	2	216	2	211	3	215	15
KB081121-1-9	220	3	218	2	214	3	226	28
KB081121-1-10	220	4	220	3	217	4	214	27
KB081121-1-11	213	3	217	2	209	5	160	44
KB081121-1-12	216	3	217	4	214	6	195	22
KB081121-1-13	227	3	226	3	224	5	208	21
KB081121-1-14	220	2	222	2	221	3	198	20
KB081121-1-15	219	2	218	1	215	2	221	15
KB081121-1-16	216	2	215	1	209	2	209	13
KB081121-1-17	218	2	219	2	215	2	195	16
KB081121-1-18	221	3	220	2	215	2	224	15
KB081121-1-19	218	2	219	2	215	3	216	18
KB081121-1-20	222	3	223	2	227	3	218	32
KB081121-1-21	217	2	215	2	213	3	223	19
KB081121-1-22	223	2	217	2	216	3	262	18
KB081121-1-23	218	2	218	2	214	2	198	8
KB081121-1-24	213	2	213	2	196	6	208	20
KB081121-1-25	224	3	210	2	212	4	385	40
KB081121-1-26	219	2	218	2	210	2	227	22
KB081121-1-27	215	2	216	2	208	3	193	17
KB081121-1-28	226	2	227	2	232	4	206	16

Table 2d: U-Pb analytical data for 79 zircon from the upper grey lithic tuff in Agnew Meadows.

Sample	Age (Ma) ^{207}Pb/^{235}U	207/235 age 2σ error	Age (Ma) ^{206}Pb/^{238}U	206/238 age 2σ error	Age (Ma) ^{208}Pb/^{232}U	208/232 age 2σ error	Age (Ma) ^{207}Pb/^{206}Pb	207/206 age 2σ error
KB081121-1-29	221	3	222	2	222	4	209	22
KB081121-1-30	219	2	217	2	210	2	223	15
KB081121-1-31	219	2	219	2	209	2	217	10
KB081121-1-32	219	2	213	1	212	3	284	12
KB081121-1-33	219	1	218	2	212	2	221	13
KB081121-1-34	217	2	216	2	211	3	229	15
KB081121-1-35	217	2	216	2	211	2	207	12
KB081121-1-36	222	2	220	2	212	2	224	11
KB081121-1-37	217	2	214	2	209	3	228	10
KB081121-1-38	215	3	214	2	207	4	216	14
KB081121-1-39	215	2	215	2	206	2	196	16
KB081121-1-40	217	2	216	2	211	2	212	13
KB081121-1-41	237	5	229	4	244	8	305	24
KB081121-1-42	220	2	220	2	216	3	219	19
KB081121-1-43	221	2	217	2	213	2	249	9
KB081121-1-44	221	3	220	2	213	3	221	16
KB081121-1-45	220	3	219	2	212	3	224	14
KB081121-1-46	222	2	219	2	211	2	238	13
KB081121-1-47	225	7	224	8	221	12	216	16
KB081121-1-48	225	5	222	4	217	6	220	18
KB081121-1-49	222	2	220	2	214	2	218	12
KB081121-1-50	223	3	219	2	215	3	245	24
KB081121-1-51	225	3	223	3	220	3	226	17
KB081121-1-52	223	3	223	2	217	3	207	16
KB081121-1-53	223	3	220	2	215	2	232	22
KB081121-1-54	222	2	219	2	215	2	249	9
KB081121-1-55	217	3	217	2	209	3	202	14
KB081121-1-56	222	2	219	2	217	3	240	17
KB081121-1-57	220	2	219	2	210	3	207	13

Table 2e: U-Pb analytical data for 79 zircon from the upper grey lithic tuff in Agnew Meadows.

Sample	Age (Ma) $^{207}Pb/^{235}U$	207/235 age 2σ error	Age (Ma) $^{206}Pb/^{238}U$	206/238 age 2σ error	Age (Ma) $^{208}Pb/^{232}U$	208/232 age 2σ error	Age (Ma) $^{207}Pb/^{206}Pb$	207/206 age 2σ error
KB081121-1-58	222	3	222	2	217	3	216	16
KB081121-1-59	217	3	216	1	209	2	213	20
KB081121-1-60	222	3	221	3	218	4	212	21
KB081121-1-61	224	2	221	1	213	2	233	26
KB081121-1-62	227	2	214	1	217	2	342	17
KB081121-1-63	221	2	217	2	213	3	231	9
KB081121-1-64	233	3	234	2	227	3	233	20
KB081121-1-65	230	3	229	2	223	2	230	23
KB081121-1-66	220	3	218	3	211	2	213	12
KB081121-1-67	218	3	217	2	214	3	207	15
KB081121-1-68	231	5	223	3	225	8	267	31
KB081121-1-69	220	3	216	3	197	8	247	15
KB081121-1-70	218	3	216	2	212	2	209	21
KB081121-1-71	620	130	253	12	720	160	2000	540
KB081121-1-72	225	2	220	2	219	3	259	17
KB081121-1-73	222	3	220	3	215	3	215	13
KB081121-1-74	232	2	219	2	230	4	342	14
KB081121-1-76	227	3	222	2	219	3	262	20
KB081121-1-77	227	6	225	6	226	10	234	21
KB081121-1-78	220	7	218	7	216	11	229	23
KB081121-1-79	219	3	217	2	212	3	231	14
KB081121-1-80	222	2	221	2	220	2	225	13

Table 2f: U-Pb analytical data for 79 zircon from the upper grey lithic tuff in Agnew Meadows.

Sample	$^{207}\text{Pb}/^{235}\text{U}$	$^{207}\text{Pb}/^{235}\text{U}$ 2σ error	$^{206}\text{Pb}/^{238}\text{U}$	$^{206}\text{Pb}/^{238}\text{U}$ 2σ error	$^{238}\text{U}/^{206}\text{Pb}$	$^{238}\text{U}/^{206}\text{Pb}$ 2σ error	$^{207}\text{Pb}/^{206}\text{Pb}$	$^{207}\text{Pb}/^{206}\text{Pb}$ 2σ error	Concor-dance	Discor-dance
KB081221-1-1	0.248	0.006	0.04	0.00	28.51	0.77	0.051	0.001	0.97	0.99
KB081221-1-2	0.266	0.010	0.03	0.00	28.83	0.86	0.056	0.001	0.51	0.91
KB081221-1-3	0.246	0.005	0.03	0.00	28.69	0.60	0.051	0.001	0.95	0.99
KB081221-1-5	0.245	0.006	0.03	0.00	28.79	0.62	0.051	0.001	0.96	0.99
KB081221-1-6	0.251	0.009	0.04	0.00	27.88	0.82	0.050	0.001	1.14	1.00
KB081221-1-7	0.247	0.006	0.03	0.00	28.66	0.65	0.051	0.001	0.87	0.99
KB081221-1-9	0.247	0.006	0.04	0.00	28.56	0.65	0.051	0.001	0.99	0.99
KB081221-1-10	0.268	0.009	0.03	0.00	28.97	0.67	0.056	0.002	0.48	0.91
KB081221-1-11	0.245	0.006	0.04	0.00	28.49	0.79	0.051	0.001	1.01	1.00
KB081221-1-12	0.244	0.008	0.03	0.00	28.81	0.97	0.050	0.001	1.03	0.99
KB081221-1-13	0.242	0.006	0.03	0.00	29.09	0.68	0.051	0.001	0.96	0.99
KB081221-1-14	0.245	0.006	0.04	0.00	28.47	0.75	0.050	0.001	1.05	1.00
KB081221-1-15	0.242	0.008	0.03	0.00	28.90	0.74	0.050	0.001	1.16	1.00
KB081221-1-16	0.242	0.006	0.03	0.00	29.28	0.67	0.051	0.001	0.96	0.98
KB081221-1-17	0.242	0.006	0.03	0.00	28.73	0.63	0.050	0.001	1.07	1.00
KB081221-1-18	0.246	0.006	0.03	0.00	28.63	0.65	0.051	0.001	0.99	0.99
KB081221-1-19	0.249	0.007	0.04	0.00	28.06	0.75	0.050	0.001	1.08	1.00
KB081221-1-20	0.252	0.010	0.04	0.00	28.33	0.94	0.051	0.001	0.89	0.98
KB081221-1-21	0.242	0.008	0.03	0.00	29.41	0.98	0.051	0.001	0.94	0.98
KB081221-1-22	0.243	0.006	0.03	0.00	28.88	0.74	0.051	0.001	0.99	1.00
KB081221-1-23	0.242	0.007	0.03	0.00	29.40	0.67	0.051	0.001	0.89	0.98
KB081221-1-24	0.247	0.007	0.04	0.00	28.43	0.67	0.051	0.001	0.95	0.99
KB081221-1-25	0.245	0.006	0.03	0.00	28.85	0.68	0.051	0.001	1.00	0.99
KB081221-1-26	0.242	0.010	0.03	0.00	29.15	1.25	0.050	0.001	1.02	0.99
KB081221-1-28	0.243	0.006	0.03	0.00	28.87	0.74	0.051	0.001	0.96	0.99
KB081221-1-29	0.247	0.006	0.04	0.00	28.47	0.68	0.051	0.001	0.97	0.99
KB081221-1-30	0.248	0.008	0.04	0.00	28.42	0.95	0.051	0.001	0.95	0.99
KB081221-1-31	0.242	0.006	0.03	0.00	28.93	0.69	0.051	0.001	0.98	1.00
KB081221-1-32	0.241	0.005	0.03	0.00	29.17	0.63	0.051	0.001	0.95	0.99
KB081221-1-34	0.249	0.007	0.03	0.00	29.32	0.71	0.052	0.001	0.71	0.96

Table 3a: U-Pb analytical data for 53 zircon from the lower grey lithic tuff in Agnew Meadows.

Sample	^{207}Pb/^{235}U	^{207}Pb/^{235}U 2σ error	^{206}Pb/^{238}U	^{206}Pb/^{238}U 2σ error	^{238}U/^{206}Pb	^{238}U/^{206}Pb 2σ error	^{207}Pb/^{206}Pb	^{207}Pb/^{206}Pb 2σ error	Concordance	Discordance
KB081221-1-35	0.245	0.006	0.03	0.00	28.68	0.73	0.051	0.001	0.97	0.99
KB081221-1-36	0.269	0.008	0.04	0.00	28.36	0.66	0.055	0.001	0.54	0.92
KB081221-1-37	0.243	0.005	0.03	0.00	28.96	0.65	0.051	0.001	0.97	0.99
KB081221-1-39	0.246	0.006	0.03	0.00	28.79	0.63	0.051	0.001	0.94	0.99
KB081221-1-40	0.245	0.006	0.03	0.00	28.66	0.68	0.051	0.001	0.98	0.99
KB081221-1-41	0.245	0.006	0.03	0.00	28.74	0.67	0.051	0.001	0.99	0.99
KB081221-1-42	0.251	0.008	0.04	0.00	27.96	0.82	0.050	0.001	1.05	1.00
KB081221-1-43	0.248	0.005	0.04	0.00	28.27	0.63	0.051	0.001	1.00	1.00
KB081221-1-44	0.242	0.007	0.03	0.00	29.33	0.71	0.051	0.001	0.93	0.98
KB081221-1-45	0.251	0.011	0.04	0.00	28.25	1.18	0.051	0.001	0.95	0.99
KB081221-1-46	0.264	0.013	0.04	0.00	27.55	1.26	0.052	0.001	0.77	0.97
KB081221-1-48	0.256	0.010	0.04	0.00	28.01	1.03	0.052	0.001	0.85	0.98
KB081221-1-49	0.242	0.006	0.03	0.00	29.32	0.68	0.051	0.001	0.93	0.98
KB081221-1-50	0.246	0.008	0.03	0.00	28.89	0.83	0.051	0.001	0.84	0.98
KB081221-1-51	0.249	0.007	0.04	0.00	28.35	0.76	0.051	0.001	0.97	0.99
KB081221-1-52	0.250	0.009	0.04	0.00	28.34	0.88	0.051	0.001	1.00	0.99
KB081221-1-53	0.253	0.008	0.04	0.00	28.25	0.77	0.051	0.001	0.86	0.98
KB081221-1-54	0.248	0.006	0.04	0.00	28.46	0.71	0.051	0.001	0.99	0.99
KB081221-1-55	0.257	0.009	0.04	0.00	28.50	0.71	0.053	0.001	0.69	0.96
KB081221-1-57	0.247	0.006	0.04	0.00	28.28	0.68	0.050	0.001	1.05	1.00
KB081221-1-58	0.250	0.006	0.04	0.00	28.29	0.62	0.051	0.001	0.95	0.99
KB081221-1-59	0.246	0.007	0.03	0.00	28.58	0.76	0.051	0.001	1.00	0.99
KB081221-1-60	0.243	0.007	0.03	0.00	30.89	0.98	0.054	0.001	0.57	0.93

Table 3b: U-Pb analytical data for 53 zircon from the lower grey lithic tuff in Agnew Meadows.

Sample	Age (Ma) ^{207}Pb/^{235}U	207/235 age 2σ error	Age (Ma) ^{206}Pb/^{238}U	206/238 age 2σ error	Age (Ma) ^{208}Pb/^{232}U	208/232 age 2σ error	Age (Ma) ^{207}Pb/^{206}Pb	207/206 age 2σ error
KB081221-1-1	225	3	222	4	222	6	228	22
KB081221-1-2	241	8	220	5	238	8	431	37
KB081221-1-3	224	1	221	1	220	2	230	12
KB081221-1-5	222	3	220	2	220	2	233	22
KB081221-1-6	227	6	227	5	234	6	197	37
KB081221-1-7	224	2	221	2	218	4	253	25
KB081221-1-9	224	3	222	2	222	4	223	18
KB081221-1-10	241	6	219	3	209	5	448	66
KB081221-1-11	222	3	222	4	224	6	220	13
KB081221-1-12	221	6	220	6	226	10	213	15
KB081221-1-13	221	3	218	3	220	3	226	22
KB081221-1-14	223	3	223	4	225	6	211	22
KB081221-1-15	220	5	219	4	225	6	187	26
KB081221-1-16	220	3	217	2	222	3	223	22
KB081221-1-17	220	3	221	2	217	3	204	17
KB081221-1-18	223	3	221	2	223	3	222	24
KB081221-1-19	226	4	226	4	239	8	207	18
KB081221-1-20	228	7	224	6	228	10	249	34
KB081221-1-21	220	5	216	6	218	9	227	15
KB081221-1-22	221	3	219	3	220	5	221	18
KB081221-1-23	220	4	216	2	224	4	240	38
KB081221-1-24	224	4	223	3	223	4	233	21
KB081221-1-25	222	3	220	3	222	2	219	12
KB081221-1-26	220	7	218	8	220	13	212	18
KB081221-1-28	221	3	220	3	222	5	228	14
KB081221-1-29	224	3	223	3	227	3	228	21
KB081221-1-30	225	5	223	6	229	9	233	21
KB081221-1-31	220	3	219	3	220	5	225	18
KB081221-1-32	219	1	217	2	219	2	228	15
KB081221-1-34	226	4	216	3	219	3	302	37

Table 3c: U-Pb analytical data for 53 zircon from the lower grey lithic tuff in Agnew Meadows.

Sample	Age (Ma) ^{207}Pb/^{235}U	207/235 age 2σ error	Age (Ma) ^{206}Pb/^{238}U	206/238 age 2σ error	Age (Ma) ^{208}Pb/^{232}U	208/232 age 2σ error	Age (Ma) ^{207}Pb/^{206}Pb	207/206 age 2σ error
KB081221-1-35	223	3	221	3	228	5	225	19
KB081221-1-36	242	5	223	3	256	6	410	34
KB081221-1-37	221	2	219	2	221	3	223	16
KB081221-1-39	223	3	220	2	221	4	232	19
KB081221-1-40	223	3	221	3	222	4	224	14
KB081221-1-41	223	3	221	3	222	3	220	16
KB081221-1-42	228	5	227	5	233	7	213	20
KB081221-1-43	225	2	224	2	226	2	221	23
KB081221-1-44	220	4	216	3	222	4	230	25
KB081221-1-45	227	8	225	8	231	14	235	17
KB081221-1-46	238	10	230	9	238	17	304	30
KB081221-1-48	231	7	226	7	232	11	264	12
KB081221-1-49	220	3	216	3	222	4	232	16
KB081221-1-50	223	5	219	4	227	6	258	27
KB081221-1-51	226	4	223	4	229	6	229	24
KB081221-1-52	227	6	224	5	226	7	222	23
KB081221-1-53	229	5	224	4	242	5	260	24
KB081221-1-54	225	3	223	3	228	3	224	14
KB081221-1-55	232	6	222	3	238	6	317	40
KB081221-1-57	224	3	224	3	230	4	212	18
KB081221-1-58	227	2	224	2	226	3	234	18
KB081221-1-59	224	4	222	4	226	6	221	21
KB081221-1-60	221	4	205	5	181	10	356	24

Table 3d: U-Pb analytical data for 53 zircon from the lower grey lithic tuff in Agnew Meadows.

Sample	^{207}Pb/^{235}U	^{207}Pb/^{235}U 2σ error	^{206}Pb/^{238}U	^{206}Pb/^{238}U 2σ error	^{238}U/^{206}Pb	^{238}U/^{206}Pb 2σ error	^{207}Pb/^{206}Pb	^{207}Pb/^{206}Pb 2σ error	Concor-dance	Discor-dance
KB081521-1-1	0.257	0.007	0.04	0.00	27.40	0.70	0.050	0.001	1.09	0.99
KB081521-1-2	0.248	0.006	0.04	0.00	28.41	0.63	0.051	0.001	0.98	0.99
KB081521-1-3	0.247	0.007	0.04	0.00	28.54	0.77	0.051	0.001	0.97	0.99
KB081521-1-4	0.249	0.006	0.03	0.00	28.87	0.67	0.052	0.001	0.82	0.97
KB081521-1-5	0.256	0.008	0.04	0.00	27.33	0.66	0.050	0.001	1.08	1.00
KB081521-1-6	0.253	0.010	0.04	0.00	27.86	1.09	0.051	0.001	1.01	0.99
KB081521-1-7	0.263	0.007	0.04	0.00	27.23	0.60	0.051	0.001	0.93	0.98
KB081521-1-8	0.241	0.006	0.03	0.00	29.15	0.65	0.051	0.001	0.97	0.99
KB081521-1-9	0.245	0.006	0.03	0.00	28.91	0.72	0.051	0.001	0.92	0.98
KB081521-1-10	0.237	0.006	0.03	0.00	29.76	0.64	0.051	0.001	0.92	0.99
KB081521-1-11	0.239	0.005	0.03	0.00	29.37	0.67	0.050	0.001	1.02	0.99
KB081521-1-12	0.241	0.007	0.03	0.00	29.28	0.72	0.051	0.001	0.87	0.99
KB081521-1-13	0.247	0.007	0.03	0.00	29.03	0.73	0.052	0.001	0.79	0.97
KB081521-1-14	0.245	0.006	0.03	0.00	28.91	0.61	0.051	0.001	0.90	0.99
KB081521-1-15	0.246	0.005	0.03	0.00	28.79	0.63	0.051	0.001	0.91	0.99
KB081521-1-16	0.238	0.006	0.03	0.00	29.23	0.70	0.050	0.001	1.12	1.00
KB081521-1-17	0.234	0.006	0.03	0.00	30.15	0.73	0.051	0.001	0.91	0.99
KB081521-1-18	0.244	0.007	0.03	0.00	28.77	0.69	0.051	0.001	0.94	0.99
KB081521-1-19	0.256	0.010	0.04	0.00	27.47	1.12	0.051	0.001	1.06	1.00
KB081521-1-20	0.242	0.007	0.03	0.00	29.39	0.91	0.051	0.001	0.92	0.98
KB081521-1-21	0.261	0.006	0.04	0.00	27.46	0.70	0.052	0.001	0.84	0.98
KB081521-1-22	0.242	0.006	0.03	0.00	29.24	0.67	0.051	0.001	0.91	0.98
KB081521-1-23	0.245	0.006	0.03	0.00	29.00	0.64	0.051	0.001	0.91	0.98
KB081521-1-24	0.258	0.006	0.04	0.00	27.43	0.62	0.051	0.001	0.95	0.99
KB081521-1-25	0.248	0.006	0.04	0.00	28.56	0.64	0.051	0.001	0.91	0.99
KB081521-1-26	0.244	0.006	0.03	0.00	28.81	0.67	0.051	0.001	0.99	0.99
KB081521-1-27	0.242	0.005	0.03	0.00	29.17	0.64	0.051	0.001	0.92	0.99
KB081521-1-28	0.248	0.005	0.04	0.00	28.47	0.63	0.051	0.001	0.93	0.99
KB081521-1-29	0.264	0.008	0.04	0.00	27.16	0.79	0.051	0.001	0.93	0.98
KB081521-1-31	0.245	0.006	0.03	0.00	28.61	0.66	0.050	0.001	1.03	1.00

Table 4a: U-Pb analytical data for 53 zircon from the coarse-grained lithic tuff at Red and White Spur.

Sample	$^{207}Pb/^{235}U$	$^{207}Pb/^{235}U$ 2_σ error	$^{206}Pb/^{238}U$	$^{206}Pb/^{238}U$ 2_σ error	$^{238}U/^{206}Pb$	$^{238}U/^{206}Pb$ 2_σ error	$^{207}Pb/^{206}Pb$	$^{207}Pb/^{206}Pb$ 2_σ error	Concor-dance	Discor-dance
KB081521-1-32	0.247	0.006	0.04	0.00	28.56	0.69	0.051	0.001	1.00	0.99
KB081521-1-33	0.249	0.014	0.04	0.00	28.49	1.57	0.051	0.001	0.87	0.99
KB081521-1-34	0.246	0.009	0.04	0.00	28.33	1.12	0.051	0.001	1.01	1.00
KB081521-1-35	0.247	0.006	0.03	0.00	29.27	0.64	0.052	0.001	0.75	0.97
KB081521-1-36	0.247	0.006	0.03	0.00	28.73	0.69	0.051	0.001	0.94	0.99
KB081521-1-37	0.243	0.006	0.03	0.00	28.79	0.67	0.050	0.001	1.07	1.00
KB081521-1-38	0.248	0.008	0.03	0.00	28.65	0.84	0.051	0.001	0.90	0.98
KB081521-1-39	0.263	0.010	0.04	0.00	26.81	1.02	0.051	0.001	0.97	1.00
KB081521-1-40	0.246	0.008	0.04	0.00	28.56	0.99	0.051	0.001	0.98	0.99
KB081521-1-41	0.261	0.007	0.04	0.00	27.51	0.72	0.051	0.001	0.89	0.98
KB081521-1-42	0.265	0.007	0.04	0.00	27.03	0.64	0.051	0.001	0.92	0.98
KB081521-1-43	0.246	0.006	0.03	0.00	28.69	0.68	0.051	0.001	0.94	0.99
KB081521-1-44	0.244	0.009	0.03	0.00	28.90	1.09	0.051	0.001	0.94	0.99
KB081521-1-45	0.256	0.008	0.04	0.00	27.46	0.62	0.051	0.001	0.97	1.00
KB081521-1-46	0.243	0.006	0.03	0.00	28.79	0.69	0.051	0.001	0.97	1.00
KB081521-1-47	0.247	0.006	0.03	0.00	28.81	0.67	0.051	0.001	0.94	0.98
KB081521-1-48	0.281	0.012	0.04	0.00	27.45	0.74	0.055	0.002	0.54	0.91
KB081521-1-49	0.252	0.006	0.03	0.00	28.64	0.67	0.052	0.001	0.77	0.97
KB081521-1-50	0.243	0.006	0.03	0.00	29.04	0.69	0.051	0.001	0.95	0.99
KB081521-1-51	0.250	0.006	0.04	0.00	28.22	0.65	0.051	0.001	0.92	0.99
KB081521-1-52	0.244	0.006	0.03	0.00	29.03	0.67	0.051	0.001	0.89	0.99
KB081521-1-53	0.244	0.006	0.03	0.00	29.10	0.78	0.051	0.001	0.89	0.98
KB081521-1-54	0.247	0.006	0.04	0.00	28.55	0.68	0.051	0.001	0.96	0.99

Table 4b: U-Pb analytical data for 53 zircon from the coarse-grained lithic tuff at Red and White Spur.

Sample	Age (Ma) ^{207}Pb/^{235}U	207/235 age 2σ error	Age (Ma) ^{206}Pb/^{238}U	206/238 age 2σ error	Age (Ma) ^{208}Pb/^{232}U	208/232 age 2σ error	Age (Ma) ^{207}Pb/^{206}Pb	207/206 age 2σ error
KB081521-1-1	232	3	231	4	235	5	210	19
KB081521-1-2	225	2	223	2	228	4	226	19
KB081521-1-3	224	4	222	4	227	5	228	17
KB081521-1-4	226	3	220	3	229	3	267	17
KB081521-1-5	232	5	232	3	237	5	213	34
KB081521-1-6	229	7	227	8	231	10	225	12
KB081521-1-7	237	4	233	2	234	4	249	29
KB081521-1-8	220	3	218	2	218	3	226	16
KB081521-1-9	223	4	219	3	222	5	237	19
KB081521-1-10	216	2	213	2	219	3	231	20
KB081521-1-11	218	2	216	2	217	3	211	15
KB081521-1-12	219	4	216	3	233	4	248	17
KB081521-1-13	224	4	218	3	229	7	273	25
KB081521-1-14	223	3	219	1	222	3	243	16
KB081521-1-15	223	2	220	2	219	2	241	15
KB081521-1-16	218	4	217	3	221	3	193	13
KB081521-1-17	213	3	210	3	212	3	229	14
KB081521-1-18	222	4	220	3	221	4	232	12
KB081521-1-19	231	7	231	8	233	11	217	16
KB081521-1-20	220	5	216	5	215	7	233	10
KB081521-1-21	236	3	231	4	235	5	273	10
KB081521-1-22	220	3	217	2	224	4	237	17
KB081521-1-23	222	2	219	2	219	2	239	16
KB081521-1-24	233	3	231	2	228	2	240	17
KB081521-1-25	225	2	222	2	221	3	241	12
KB081521-1-26	223	3	220	3	219	4	221	14
KB081521-1-27	220	2	217	2	216	3	234	21
KB081521-1-28	226	2	223	2	222	3	237	13
KB081521-1-29	238	5	233	5	229	6	248	23
KB081521-1-31	222	3	222	2	219	3	214	15

Table 4c: U-Pb analytical data for 53 zircon from the coarse-grained lithic tuff at Red and White Spur.

Sample	Age (Ma) ^{207}Pb/^{235}U	207/235 age 2σ error	Age (Ma) ^{206}Pb/^{238}U	206/238 age 2σ error	Age (Ma) ^{208}Pb/^{232}U	208/232 age 2σ error	Age (Ma) ^{207}Pb/^{206}Pb	207/206 age 2σ error
KB081521-1-32	224	3	222	3	220	4	220	18
KB081521-1-33	226	10	223	11	222	17	255	17
KB081521-1-34	223	6	223	7	217	7	225	19
KB081521-1-35	224	3	217	2	219	4	285	27
KB081521-1-36	224	3	221	3	219	3	234	12
KB081521-1-37	221	3	220	3	220	6	211	20
KB081521-1-38	225	5	221	5	224	6	245	17
KB081521-1-39	237	6	236	8	227	6	243	15
KB081521-1-40	223	6	222	6	218	9	226	9
KB081521-1-41	235	3	230	4	230	4	262	24
KB081521-1-42	238	4	234	3	231	4	252	32
KB081521-1-43	223	3	221	3	215	3	233	13
KB081521-1-44	221	7	219	7	217	11	231	20
KB081521-1-45	232	5	231	2	228	3	235	40
KB081521-1-46	221	3	220	3	216	3	225	14
KB081521-1-47	224	3	220	3	212	3	232	17
KB081521-1-48	253	10	231	4	263	19	422	57
KB081521-1-49	228	3	221	3	223	2	285	22
KB081521-1-50	221	2	218	3	208	3	228	14
KB081521-1-51	226	3	224	3	218	2	242	18
KB081521-1-52	222	2	218	2	211	3	243	12
KB081521-1-53	222	3	218	4	209	4	243	16
KB081521-1-54	225	3	222	3	214	4	230	18

Table 4d: U-Pb analytical data for 53 zircon from the coarse-grained lithic tuff at Red and White Spur.

Sample	U (ppm)	Th (ppm)	Si (ppm)	P (ppm)	Ti (ppm)	Y (ppm)	Nb (ppm)	La (ppm)	Ce (ppm)	Pr (ppm)	Nd (ppm)
KB081121-1-1	592	176.4	1.47E+05	137.3	3.37	901	2.42	3.25	28.4	1.99	6.58
KB081121-1-2	806	265.5	1.53E+05	104.5	1.66	1107	3.51	0.0073	13.03	0.095	0.81
KB081121-1-3	1528	646	1.53E+05	112.8	5.3	1386	6.22	2.68	30.1	1.84	6.61
KB081121-1-4	923	317.5	1.53E+05	117.6	1.8	1110	3.58	0.041	13.45	0.092	1.22
KB081121-1-5	1003	350	1.52E+05	480	2.12	1257	6.14	4.5	38.6	3.7	11.7
KB081121-1-6	586	169	1.53E+05	111.9	1.42	826	1.97	0.0045	9.2	0.025	0.333
KB081121-1-7	325	133.1	1.50E+05	63.9	6.8	551	1.013	0.137	5.8	0.075	0.68
KB081121-1-8	1176	640	1.53E+05	79.2	1.99	1091	3.98	0.0114	22.79	0.051	0.82
KB081121-1-9	620	259.4	1.51E+05	660	1.35	1095	2.33	28	75	9.7	24.5
KB081121-1-10	471	182.8	1.51E+05	84.1	1.89	928	1.67	0.019	9.14	0.075	0.95
KB081121-1-11	153.6	36.4	1.48E+05	60.1	1.82	339	0.88	0.014	3.12	0.014	0.2
KB081121-1-12	274	76.4	1.48E+05	89.4	1.55	546	1.09	0.0123	5.16	0.04	0.43
KB081121-1-13	327	111.6	1.47E+05	48.9	2.82	510	0.92	0.0077	4.52	0.057	0.77
KB081121-1-14	702	176.7	1.45E+05	79.1	1.1	980	3.76	0.0076	12.85	0.017	0.42
KB081121-1-15	816	248	1.48E+05	121.9	1.71	1074	3.33	0.182	12.75	0.186	1.2
KB081121-1-16	1001	371	1.49E+05	148	1.62	1011	3.59	0.88	17.2	0.67	3.2
KB081121-1-17	1179	569	1.53E+05	78	1.56	1121	4.02	0.059	22.5	0.093	0.67
KB081121-1-18	812	403	1.46E+05	73.5	2.07	804	2.56	0.015	13.34	0.051	0.74
KB081121-1-19	1070	434	1.58E+05	73.9	1.73	1346	6.15	0.014	28.3	0.049	0.5
KB081121-1-20	388	125.6	1.51E+05	73.5	2.78	800	2.24	0.0061	8.57	0.041	0.54
KB081121-1-21	402	104.9	1.53E+05	57.8	1.15	616	1.74	0.0108	6.88	0.029	0.33
KB081121-1-22	910	319.5	1.52E+05	502	2.84	1216	5.09	1.16	24.6	1.64	6.26
KB081121-1-23	955	312	1.49E+05	73.9	1.17	1123	4.92	-1.84E-05	14.74	0.054	0.5
KB081121-1-24	665	317	1.53E+05	90	2.56	1103	2.32	0.034	14.09	0.136	1.35
KB081121-1-25	796	275	1.85E+05	4.90E+03	70.8	1400	5.6	47	290	40	133
KB081121-1-26	844	286.8	1.48E+05	93.9	1.96	1111	4.92	0.015	17.07	0.034	0.75
KB081121-1-27	886	278	1.52E+05	105.6	1.91	1121	4.13	0.007	12.97	0.039	0.56
KB081121-1-28	821	289	1.50E+05	66.3	1.5	923	3.12	0.0029	14.79	0.043	0.6
KB081121-1-29	502	200	1.51E+05	70.6	2.69	978	3.03	0.0099	14.2	0.06	0.7
KB081121-1-30	984	379	1.49E+05	78.8	2.87	1087	4.1	0.7	20.22	0.59	2.39
KB081121-1-31	1393	1125	1.50E+05	116.1	4.6	1776	6.16	0.045	47.2	0.236	2.65

Table 5a: Zircon trace element geochemical data for 79 zircon from the upper grey lithic tuff in Agnew Meadows.

Sample	Sm (ppm)	Eu (ppm)	Gd (ppm)	Tb (ppm)	Dy (ppm)	Ho (ppm)	Er (ppm)	Tm (ppm)	Yb (ppm)	Lu (ppm)	Hf (ppm)	Ta (ppm)
KB081121-1-1	3.06	1.38	13.32	5.28	71.3	28.5	150.1	40.1	399	86.4	10220	2.32
KB081121-1-2	1.74	0.69	12.93	5.94	88.9	38.4	199	54.7	550	126.2	10410	4.03
KB081121-1-3	4.3	1.83	25.6	9.79	135.2	51.6	252.7	67.4	625	137	10730	7.3
KB081121-1-4	1.97	0.66	15.4	6.69	95.4	41.8	213.7	56.1	552	122.2	10310	3.69
KB081121-1-5	3.6	0.86	16.9	6.52	103.4	45.4	245	67.8	667	150.1	10010	5.93
KB081121-1-6	0.86	0.348	8.99	3.45	55.6	24.1	131.5	38.4	385	87.8	10270	2.03
KB081121-1-7	0.66	0.431	6.04	2.62	39	16.55	88.7	24.5	250	63.5	8090	0.74
KB081121-1-8	1.92	0.59	15.5	5.97	89.5	35.3	177.2	48.4	463	101.6	10580	5.25
KB081121-1-9	5.38	1.17	16.9	6.08	83.9	35.6	180.5	49.6	482	106.1	10510	2.48
KB081121-1-10	2.35	0.74	12.4	5.2	73.1	28.4	145.7	41.3	402	88.1	9620	1.81
KB081121-1-11	0.36	0.154	3.83	1.5	24	10.38	54.3	15.93	166.1	39.3	9520	0.78
KB081121-1-12	0.9	0.334	5.89	2.62	39	16.6	90.7	25.6	265	61.5	9140	1.14
KB081121-1-13	1.16	0.468	7.33	2.58	41.3	15.82	83.1	22.57	240	53.9	10000	0.91
KB081121-1-14	1.04	0.388	10.55	4.36	68	29.4	165.6	48.3	495	115.1	10230	4.32
KB081121-1-15	1.62	0.62	13.5	5.66	92.3	36.9	193.2	54.6	535	119.4	10050	3.18
KB081121-1-16	1.71	0.6	12.3	5.3	79.2	32.3	157.4	42.7	423	89.7	10900	4.51
KB081121-1-17	1.87	0.62	14.4	6.05	93.2	36.2	187.5	50.9	485	104.2	10790	5.08
KB081121-1-18	1.08	0.506	11.21	4.45	59.6	25.8	127.9	33.5	328	71.8	9770	3.31
KB081121-1-19	1.93	0.498	17.3	6.93	113.9	48.3	258.2	71	698	156.2	11050	6.43
KB081121-1-20	1.18	0.38	9.1	3.65	58.2	24.09	134.8	36.7	354	80.4	9630	1.99
KB081121-1-21	0.63	0.232	6.61	2.83	46.3	19.1	102.2	29.4	287	62.9	11050	2.3
KB081121-1-22	2.79	0.66	15.9	7	110.2	46.3	244	64.1	650	139.9	9650	4.78
KB081121-1-23	1.58	0.492	12.45	5.31	86.1	36.2	197.2	53.8	542	122.6	10640	4.98
KB081121-1-24	2.1	0.75	15.2	5.76	83.8	34.8	178.1	47.4	502	104.5	10390	2.47
KB081121-1-25	25	4	45	10.7	119	43	220.4	57.6	557	131.2	10050	4.43
KB081121-1-26	1.34	0.518	13.19	5.88	93.2	40.8	219	62.8	636	136	9780	4.2
KB081121-1-27	1.6	0.63	15.2	6.54	96.4	42	220	60.7	586	129.9	10300	3.91
KB081121-1-28	1.47	0.366	11.94	4.74	70	28.4	150.5	39.9	392	83.8	10470	4.23
KB081121-1-29	1.66	0.67	11.5	4.94	74.2	31	163	43.7	441	98.4	8770	2.28
KB081121-1-30	2.51	1.12	16.4	6.61	94.3	36	188.2	50.2	493	107.4	10640	4.81
KB081121-1-31	4.62	1.7	34.9	13.28	174.1	67	326	83.8	794	168.3	8740	5.11

Table 5b: Zircon trace element geochemical data for 79 zircon from the upper grey lithic tuff in Agnew Meadows.

Sample	U (ppm)	Th (ppm)	Si (ppm)	P (ppm)	Ti (ppm)	Y (ppm)	Nb (ppm)	La (ppm)	Ce (ppm)	Pr (ppm)	Nd (ppm)
KB081121-1-32	1237	526	1.48E+05	92.2	3.87	1397	6.53	1.79	45.6	1.27	5.1
KB081121-1-33	700	255.2	1.47E+05	579	1.87	1036	3.67	12.5	57.6	6.87	20.2
KB081121-1-34	1119	369	1.51E+05	79	3.57	1293	6.59	0.286	20.4	0.237	1.6
KB081121-1-35	1071	339	1.50E+05	390	1.74	1215	6.72	1.81	28.9	1.85	7.3
KB081121-1-36	1200	617	1.45E+05	373	1.57	1038	3.83	3.43	30.1	2.21	8.2
KB081121-1-37	955	364	1.47E+05	277	1.85	1168	2.88	2.44	20.5	1.47	5.5
KB081121-1-38	573	137.5	1.49E+05	107.8	1.5	741	2.14	0.0047	7.23	0.028	0.264
KB081121-1-39	664	207.4	1.50E+05	63.2	1.34	876	3.08	0.044	12.6	0.057	0.63
KB081121-1-40	904	366	1.50E+05	68.1	2	1093	4.61	0.0031	20.4	0.05	0.58
KB081121-1-41	1370	530	1.50E+05	302	2.38	1530	6.46	2.4	30.2	1.61	5.9
KB081121-1-42	722	254.2	1.46E+05	69.3	4.1	1083	3.68	0.103	15	0.113	1.36
KB081121-1-43	2665	801	1.47E+05	106.1	4.27	1934	10.89	1.36	26.1	1.09	4.25
KB081121-1-44	728	188.1	1.51E+05	74.9	1.6	1067	4.34	0.0073	12.61	0.038	0.57
KB081121-1-45	865	271	1.50E+05	72.5	1.74	1088	4.37	0.0075	15.86	0.038	0.47
KB081121-1-46	1325	598	1.51E+05	99.6	3.43	1842	8.24	0.06	41.2	0.168	1.39
KB081121-1-47	571	220	1.48E+05	141	1.7	1040	1.83	0.013	10.3	0.073	0.8
KB081121-1-48	457	161	1.45E+05	116.3	2.53	890	1.59	0.0059	8.2	0.045	0.66
KB081121-1-49	830	278.9	1.51E+05	67.6	2.37	1080	5.22	0.017	20.58	0.044	0.81
KB081121-1-50	469	146.1	1.51E+05	95.4	1.33	671	1.55	0.015	10.54	0.032	0.39
KB081121-1-51	948	321.2	1.48E+05	490	2.15	1366	6.17	6.5	41	4.1	15.4
KB081121-1-52	740	270.2	1.50E+05	154	1.63	837	2.64	0.44	16.3	0.44	2.4
KB081121-1-53	502	160.1	1.56E+05	95.4	1.01	889	1.79	2.51	67.7	2.09	6.91
KB081121-1-54	1291	522	1.50E+05	79.6	2.5	1161	4.92	0.75	24.5	0.65	2.4
KB081121-1-55	663	170.1	1.46E+05	120.2	1.41	911	2.2	0.003	8.57	0.015	0.34
KB081121-1-56	867	235.7	1.47E+05	950	2.04	1174	5.76	17	72	11	37.1
KB081121-1-57	745	227.4	1.53E+05	118.7	3.5	976	2.52	0.015	10.46	0.048	0.54
KB081121-1-58	661	227	1.49E+05	121.1	1.24	1020	2.04	0.0075	11.41	0.07	0.69
KB081121-1-59	846	288	1.46E+05	96.9	1.63	1112	2.5	0.036	12.2	0.092	1.01
KB081121-1-60	514	155	1.47E+05	86.5	1.6	767	1.94	0.009	9.88	0.021	0.56
KB081121-1-61	829	337	1.46E+05	86.3	1.5	1280	2.67	0.0043	13.99	0.099	1.27

Table 5c: Zircon trace element geochemical data for 79 zircon from the upper grey lithic tuff in Agnew Meadows.

Sample	Sm (ppm)	Eu (ppm)	Gd (ppm)	Tb (ppm)	Dy (ppm)	Ho (ppm)	Er (ppm)	Tm (ppm)	Yb (ppm)	Lu (ppm)	Hf (ppm)	Ta (ppm)
KB081121-1-32	3.46	1.43	21.8	8.65	125.5	50.7	268.5	71.3	705	151.9	10310	6.89
KB081121-1-33	4.12	0.752	13.42	5.03	73	31.1	170.4	47.5	473	106.6	10420	4.19
KB081121-1-34	1.91	0.82	17.3	6.92	112.2	46.8	246.9	68.8	665	149	10450	6.59
KB081121-1-35	3	0.61	15.7	6.73	102.8	45.2	241	68.4	676	148.4	10570	6.5
KB081121-1-36	2.8	0.658	14.9	5.89	83.6	32.8	166.1	45.8	432	93.6	10250	4.39
KB081121-1-37	2.79	0.77	19.1	7.53	105.1	44.5	220.7	59.8	592	129.2	9600	3.05
KB081121-1-38	0.72	0.305	7.68	3.2	51.7	22.66	123.4	34.5	346	79.4	10250	2.32
KB081121-1-39	1.16	0.332	10.03	4.2	64.5	27.7	144.6	40.3	397	87.2	10920	4.04
KB081121-1-40	1.5	0.513	13.27	5.91	88.8	39.6	210.6	58.3	584	133.2	10440	5.21
KB081121-1-41	3.36	1.12	21.9	9.3	137	57.2	283	78	759	168	10680	5.74
KB081121-1-42	2.05	0.67	15.3	6.48	94.6	39.4	203.4	55.3	537	120.8	10490	3.45
KB081121-1-43	3.85	1.45	27.9	12.31	179.5	73.6	367	96.5	927	199.2	11870	13.11
KB081121-1-44	1.12	0.331	9.85	4.52	74.3	31.9	182.3	51.9	538	123.3	10540	4.85
KB081121-1-45	1.37	0.453	13.21	5.45	87	37.6	196.7	54.2	538	118.1	10290	5.3
KB081121-1-46	2.74	1.04	22.8	10.07	152.5	67.5	356	96	949	208.7	9740	6.29
KB081121-1-47	1.81	0.75	15.2	5.84	87	36.3	194	53.7	540	122	8360	1.72
KB081121-1-48	1.3	0.54	11.7	4.64	68.6	29.7	157	43.6	433	100	8530	1.59
KB081121-1-49	1.21	0.591	12.2	5.62	88.4	40.1	228.5	63	626	140.9	10920	5
KB081121-1-50	0.96	0.325	6.85	3.04	47.1	20.1	111.8	32.2	334	76.2	10360	1.91
KB081121-1-51	4.2	0.92	18.8	7.79	120.3	49.5	264	73	704	153.5	10340	5.09
KB081121-1-52	1.75	0.518	10.97	4.36	66.3	27.3	135.7	36.9	360	80.3	10080	3.48
KB081121-1-53	2.77	0.83	13.1	4.54	69.8	28.1	144.8	39.7	389	83.9	10510	2.06
KB081121-1-54	2.31	1	17.8	6.99	106.9	42.7	215.2	57.7	550	120.2	10630	5.95
KB081121-1-55	0.9	0.303	9.29	3.98	64.5	27.8	148.8	41.9	420	94.9	10350	2.47
KB081121-1-56	7.9	1.18	19.5	6.95	97.4	41.8	229.1	65.5	633	142.6	10500	5.43
KB081121-1-57	1.3	0.458	10.26	4.58	69.7	32.26	165.4	46	468	105.7	10460	3
KB081121-1-58	1.29	0.55	13	4.99	77.8	32.7	172.7	48.4	479	108.7	9540	2.3
KB081121-1-59	2.47	0.83	17.8	6.82	99.2	40.9	211.2	58	561	119.4	10780	3.06
KB081121-1-60	0.97	0.359	8.23	3.63	57	24.9	130.2	36.9	380	87.4	10370	2.18
KB081121-1-61	2.38	0.88	20.2	8.17	116.3	48.6	247	65.2	619	135.6	10300	3.01

Table 5d: Zircon trace element geochemical data for 79 zircon from the upper grey lithic tuff in Agnew Meadows.

Sample	U (ppm)	Th (ppm)	Si (ppm)	P (ppm)	Ti (ppm)	Y (ppm)	Nb (ppm)	La (ppm)	Ce (ppm)	Pr (ppm)	Nd (ppm)
KB081121-1-62	1161	528	1.43E+05	87	4	1073	4.22	0.71	19.82	0.525	2.61
KB081121-1-63	1949	515	1.48E+05	106.3	1.2	1999	14.06	0.074	23.1	0.078	0.58
KB081121-1-64	389	162.4	1.45E+05	59.5	2.21	828	1.5	0.034	8.91	0.086	1.2
KB081121-1-65	574	199	1.49E+05	52.6	2.58	621	1.83	-1.73E-05	13.9	0.04	0.57
KB081121-1-66	737	236.8	1.46E+05	113.8	1.04	964	2.11	0.0043	10.44	0.03	0.52
KB081121-1-67	438	114.8	1.50E+05	70.8	1.31	683	1.75	-1.73E-05	8.09	0.013	0.32
KB081121-1-68	353	105	1.47E+05	46.6	1.82	543	1.66	0.0106	6.53	0.0063	0.33
KB081121-1-69	445	164	1.51E+05	53	2.17	759	2.75	0.48	19.5	0.4	1.84
KB081121-1-70	916	318.9	1.48E+05	65.7	1.72	1033	4.22	0.014	17.36	0.039	0.74
KB081121-1-71	592	268	1.53E+05	255	3.6	954	2.15	37	87	9.6	23.6
KB081121-1-72	623	277.1	1.48E+05	45.1	4.46	550	2.11	0.0015	13.97	0.013	0.44
KB081121-1-73	899	309	1.49E+05	157	1.56	1202	5.02	1.2	22.8	0.67	2.7
KB081121-1-74	883	321	1.47E+05	117.6	8.9	1117	2.38	2.98	67.1	2.65	8.83
KB081121-1-76	949	459	1.51E+05	380	1.31	1634	2.53	4.2	39	2.5	9.1
KB081121-1-77	616	242	1.48E+05	770	2.38	1019	1.88	21	64	8.3	23
KB081121-1-78	545	195	1.48E+05	106.3	1.95	890	1.63	0.0076	10.6	0.056	0.53
KB081121-1-79	604	168	1.51E+05	116.1	1.34	844	1.89	0.022	8.06	0.05	0.36
KB081121-1-80	911	369	1.44E+05	72.1	1.43	1119	4.02	0.0078	19.8	0.071	0.75

Table 5e: Zircon trace element geochemical data for 79 zircon from the upper grey lithic tuff in Agnew Meadows.

Sample	Sm (ppm)	Eu (ppm)	Gd (ppm)	Tb (ppm)	Dy (ppm)	Ho (ppm)	Er (ppm)	Tm (ppm)	Yb (ppm)	Lu (ppm)	Hf (ppm)	Ta (ppm)
KB081121-1-62	3.07	1.91	21.9	7.85	99.5	37.4	176.8	46.6	458	95.9	10880	4.79
KB081121-1-63	1.79	0.488	21	10	166	75.5	412	113.1	1072	232.9	11790	13.42
KB081121-1-64	1.97	0.555	13.6	4.93	69	26.9	138	36.4	340	74	9960	1.73
KB081121-1-65	0.99	0.397	6.38	2.76	42	18.2	105	30.4	311	76.6	10640	2.22
KB081121-1-66	1.59	0.444	10.91	4.41	71.9	30.6	159.3	44.1	437	101.9	10150	2.19
KB081121-1-67	0.92	0.324	7.13	3.35	48.5	20.88	114.2	31.9	314	69.9	10550	2.22
KB081121-1-68	0.64	0.215	5.44	2.6	40.7	16.3	92	25	250	53.8	11160	2.47
KB081121-1-69	1.3	0.51	9.2	3.47	51.8	23.5	127.6	36.8	381	87.9	10260	3.06
KB081121-1-70	1.48	0.477	12.13	5.07	78	32.8	170.7	49.1	477	101.9	10650	4.99
KB081121-1-71	4	1.38	16	5.44	76.1	29.4	153.4	42.3	437	94	10390	1.87
KB081121-1-72	0.83	0.383	7.37	2.56	39	15.92	88.4	25.1	252.9	57.9	11120	2.65
KB081121-1-73	1.64	0.58	14	5.86	97	42.1	232	62	640	141	10150	4.98
KB081121-1-74	4.77	1.47	19.9	7.77	104.6	41.6	220.7	58	585	122.3	10400	2.73
KB081121-1-76	5.3	2.18	32.5	11.88	159.3	61.8	307	77.9	736	157.1	9870	2.46
KB081121-1-77	3.6	0.96	13.8	5.33	80.6	32.8	176	48.7	504	110.3	9150	2.04
KB081121-1-78	1.47	0.59	10.7	4.42	68.2	29	161	43.7	445	105.5	9190	1.57
KB081121-1-79	1.14	0.346	8.67	3.93	62.1	26.8	146.8	40.5	411	91.8	9910	2.22
KB081121-1-80	1.98	0.584	14.8	6.26	94	39.7	209	59.1	573	128.2	10330	4.36

Table 5f: Zircon trace element geochemical data for 79 zircon from the upper grey lithic tuff in Agnew Meadows.

Sample	U (ppm)	Th (ppm)	Si (ppm)	P (ppm)	Ti (ppm)	Y (ppm)	Nb (ppm)	La (ppm)	Ce (ppm)	Pr (ppm)	Nd (ppm)
KB081221-1-1	504	144	1.55E+05	210	1.62	768	1.63	2.1	15.6	1.4	4.5
KB081221-1-2	368	123	1.45E+05	105.6	1.76	696	1.18	0.032	6.21	0.055	0.65
KB081221-1-3	1694	575	1.53E+05	213	1.93	2022	11.39	1.93	32.7	1.44	5.4
KB081221-1-5	508	169.8	1.48E+05	114	1.64	882	1.47	0.0047	8.52	0.067	0.63
KB081221-1-6	259	91.2	1.47E+05	67.3	2.84	548	1.16	0.058	5.91	0.057	0.74
KB081221-1-7	615	244	1.55E+05	174	1.24	1064	1.92	20	59	7.1	18
KB081221-1-9	875	271	1.54E+05	129.7	1.2	1101	2.98	0.011	12.3	0.027	0.44
KB081221-1-10	569	286	1.51E+05	910	11.3	1112	1.61	5.4	25.7	3.5	11.6
KB081221-1-11	1240	473	1.54E+05	128	2.4	1450	7.25	2.2	30.9	0.61	2.7
KB081221-1-12	980	292	1.56E+05	142	1.69	1060	3.22	0.0059	11.6	0.053	0.51
KB081221-1-13	643	173.1	1.47E+05	259	1.15	837	1.88	2.17	15.4	1.27	5.2
KB081221-1-14	359	110.3	1.46E+05	102.2	1.65	739	1.24	0.0064	6.21	0.051	0.41
KB081221-1-15	553	117.3	1.57E+05	115.2	0.87	741	1.91	0.014	6.17	0.012	0.24
KB081221-1-16	656	183.5	1.51E+05	112.7	2.01	878	2.56	0.048	7.69	0.078	0.53
KB081221-1-17	1274	403	1.50E+05	91.9	1.1	1464	7.82	0.0043	19.8	0.047	0.57
KB081221-1-18	460	167.5	1.53E+05	70.8	1.76	804	1.43	0.01	9.11	0.058	1.09
KB081221-1-19	613	156.2	1.51E+05	81.8	7.1	790	2.76	0.0089	8.41	0.022	0.38
KB081221-1-20	895	245	1.52E+05	138	1.24	1080	2.57	0.0062	9.72	0.054	0.54
KB081221-1-21	880	417	1.50E+05	99.8	1.87	1350	2.47	0.048	17.5	0.158	2.07
KB081221-1-22	690	152	1.53E+05	112.7	1.53	829	2.36	0.0089	7.58	0.021	0.3
KB081221-1-23	839	258	1.52E+05	118.2	0.69	1061	2.99	0.0124	12.4	0.065	0.52
KB081221-1-24	460	154.9	1.49E+05	89.3	1.73	809	1.46	0.0079	7.76	0.056	0.88
KB081221-1-25	643	164.6	1.55E+05	62	1.52	993	3.98	0.0031	12.95	0.035	0.341
KB081221-1-26	559	186	1.51E+05	103.2	1.55	876	1.56	0.006	9.7	0.04	0.59
KB081221-1-28	973	363	1.43E+05	124.3	2.4	1320	3.95	0.019	16.7	0.077	0.89
KB081221-1-29	774	199.7	1.50E+05	66.3	1.24	1099	4.52	0.0062	12.93	0.071	0.6
KB081221-1-30	392	116.6	1.47E+05	300	1.51	711	1.2	16	43	5.1	12
KB081221-1-31	747	201.6	1.51E+05	126.1	0.99	928	2.28	0.0103	8.85	0.011	0.259
KB081221-1-32	1043	433	1.47E+05	66.2	1.92	950	3.07	0.0043	16.27	0.029	0.7
KB081221-1-34	987	422	1.45E+05	138	3.31	1468	2.28	0.54	16.3	0.91	5.2

Table 6a: Zircon trace element geochemical data for 53 zircon from the lower grey lithic tuff in Agnew Meadows.

Sample	Sm (ppm)	Eu (ppm)	Gd (ppm)	Tb (ppm)	Dy (ppm)	Ho (ppm)	Er (ppm)	Tm (ppm)	Yb (ppm)	Lu (ppm)	Hf (ppm)	Ta (ppm)
KB081221-1-1	1.47	0.44	9.32	3.38	53.8	22.9	127.4	34.5	373	87	9950	1.72
KB081221-1-2	1.16	0.477	8.21	3.29	50.3	20.9	113	32.3	318	75	8680	1.07
KB081221-1-3	3.52	0.92	24.5	11.56	170.7	74.7	387	102.3	992	208	10510	10.71
KB081221-1-5	1.46	0.541	10.67	4.21	65	26.3	141.5	39.1	403	88.8	8840	1.35
KB081221-1-6	1.02	0.411	7.9	2.72	44	17.21	91.3	25.2	243	57.2	9080	1.08
KB081221-1-7	3.7	0.79	17.1	6.27	90.3	36.4	183	49.2	462	105.1	11120	2.5
KB081221-1-9	1.11	0.5	12.1	5.31	81.7	35.8	187	53.5	526	117.6	10540	3.24
KB081221-1-10	6.04	1.6	24	8.18	103.3	39.7	189	49.1	466	100.5	9910	1.85
KB081221-1-11	2.17	0.67	17.7	7.7	122	55.2	281	76.9	767	167	10390	6.57
KB081221-1-12	1.26	0.389	12.5	5.58	86	38.6	200	54.1	537	122	10380	3.57
KB081221-1-13	1.75	0.407	9.16	4.03	62.2	27.1	136.3	39.6	387	88.6	10050	1.95
KB081221-1-14	1.35	0.48	8.51	3.85	51.2	23.1	120.3	34.5	349	80.3	8560	1.3
KB081221-1-15	0.65	0.237	6.99	3.26	54	24	125.8	36	356	80.1	10590	2.08
KB081221-1-16	0.93	0.33	10.16	4.34	64.5	27.1	145.4	40.1	402	94.2	10670	3.54
KB081221-1-17	1.72	0.489	16.4	7.87	123.8	54.1	283	77.5	753	167.7	10510	7.64
KB081221-1-18	1.61	0.567	11.4	4.18	61.5	25.4	131.9	36.4	353	79.4	10380	1.78
KB081221-1-19	1.01	0.221	7.68	3.56	56	23.61	132.1	37.3	374	82.7	11030	3.56
KB081221-1-20	1.85	0.81	14.3	6.1	86	34.7	187	49.8	499	110.3	10590	2.81
KB081221-1-21	3.39	1.21	22.1	8.74	120	49.1	261	66.3	640	142	8890	2.34
KB081221-1-22	0.89	0.299	8.48	3.72	59.6	26.4	140.9	40.7	395	89.5	10990	2.55
KB081221-1-23	1.44	0.447	12	5	79.5	34.1	187	50.1	510	112.4	10740	3.59
KB081221-1-24	1.53	0.549	10.31	4.35	62.2	24.7	133.5	37.2	365	83.9	9070	1.67
KB081221-1-25	1.1	0.412	9.87	4.13	69.9	29.9	170.9	49.4	508	117.4	10740	4.5
KB081221-1-26	1.2	0.49	9.8	3.98	62.6	27.6	146	40.9	410	93	9450	1.94
KB081221-1-28	2.19	0.79	16	7.36	115	48.6	257	69.7	667	145	9010	3.7
KB081221-1-29	1.16	0.448	11.01	4.98	77.7	32.2	185.5	54	532	118.5	10210	5.44
KB081221-1-30	2.1	0.61	9.8	3.42	48.7	22.2	119.9	33.3	333	79.2	8900	1.32
KB081221-1-31	1.23	0.317	10.08	4.22	69.5	29.2	157.4	44.8	448	100.5	10470	2.38
KB081221-1-32	1.38	0.476	13.1	4.88	74.6	30.9	153.7	41.7	402	88	10510	4.18
KB081221-1-34	5.5	2.51	30.3	11.18	149	55	273	69.7	660	143.2	8510	2.69

Table 6b: Zircon trace element geochemical data for 53 zircon from the lower grey lithic tuff in Agnew Meadows.

Sample	U (ppm)	Th (ppm)	Si (ppm)	P (ppm)	Ti (ppm)	Y (ppm)	Nb (ppm)	La (ppm)	Ce (ppm)	Pr (ppm)	Nd (ppm)
KB081221-1-35	611	287	1.51E+05	114.2	2.46	1164	2.05	0.011	13.1	0.182	1.95
KB081221-1-36	649	184	1.43E+05	302	1.22	859	2.08	1.8	15.3	1.26	4.3
KB081221-1-37	886	317	1.54E+05	380	1.71	1133	2.92	52	136	18	45
KB081221-1-39	689	191.2	1.49E+05	120.7	1.09	939	2.07	0.0042	8.3	0.035	0.39
KB081221-1-40	855	258	1.52E+05	121.9	0.73	1093	2.72	0.021	11.32	0.045	0.5
KB081221-1-41	972	234.4	1.50E+05	77.2	1.4	1153	6.16	0.021	14.14	0.053	0.58
KB081221-1-42	627	172	1.49E+05	400	1.09	860	2.05	12	27	3.5	10.1
KB081221-1-43	709	252	1.49E+05	74.7	2.22	1115	3.59	0.019	15.6	0.069	0.93
KB081221-1-44	388	100	1.51E+05	69.4	2.07	641	1.84	0.021	6.18	0.044	0.52
KB081221-1-45	506	199	1.48E+05	120.5	1.89	938	1.73	0.015	9.26	0.057	0.87
KB081221-1-46	460	180	1.51E+05	123.8	7.3	938	1.55	0.119	9.59	0.152	1.16
KB081221-1-48	1590	700	1.51E+05	150	2.52	1950	4.76	0.197	22	0.286	2.35
KB081221-1-49	662	201	1.46E+05	118.2	1.53	965	2.16	0.0071	10.89	0.034	0.5
KB081221-1-50	547	137	1.53E+05	110	1.72	760	2.51	0.049	7.06	0.043	0.57
KB081221-1-51	549	190.1	1.49E+05	125.1	1.57	1023	1.73	0.01	10.67	0.047	0.68
KB081221-1-52	457	157	1.49E+05	117.6	2.03	887	1.3	0.0074	7.69	0.045	0.65
KB081221-1-53	764	213	1.58E+05	260	0.84	1024	2.03	1.9	15.5	1.4	6
KB081221-1-54	1140	338	1.52E+05	81.1	1.63	1366	6.71	0.039	17.5	0.085	0.61
KB081221-1-55	645	190	1.49E+05	2270	4.4	970	2.21	14.7	69	12.7	43
KB081221-1-57	982	308	1.50E+05	81.1	1.95	1079	4.7	0.091	15.88	0.081	0.8
KB081221-1-58	878	246	1.53E+05	222	1.69	1137	5.57	0.7	19.6	0.9	3.53
KB081221-1-59	560	120.8	1.50E+05	103.3	0.92	705	1.91	0.0065	6.18	0.011	0.21
KB081221-1-60	1141	496	1.47E+05	94	2.91	1435	6.64	0.59	26.1	0.97	3.55

Table 6c: Zircon trace element geochemical data for 53 zircon from the lower grey lithic tuff in Agnew Meadows.

Sample	Sm (ppm)	Eu (ppm)	Gd (ppm)	Tb (ppm)	Dy (ppm)	Ho (ppm)	Er (ppm)	Tm (ppm)	Yb (ppm)	Lu (ppm)	Hf (ppm)	Ta (ppm)
KB081221-1-35	2.76	1.25	19.3	7.41	105	42.7	213	56.2	564	123	8720	1.67
KB081221-1-36	1.64	0.4	9.5	4.03	65.3	28	145	40.6	405	88.3	10120	2.52
KB081221-1-37	6.5	1.03	20.6	7.21	100.6	40.9	214	56.9	555	123.4	10280	3.12
KB081221-1-39	1.15	0.339	9.62	4.19	68.1	28.8	152.2	43.2	431	95.9	10200	2.3
KB081221-1-40	1.2	0.353	11.46	4.92	77.9	33.6	176.2	48.6	493	110.5	10260	3.16
KB081221-1-41	1.54	0.45	13.3	6.05	96.2	41.5	228.5	64.1	643	145.2	10320	6.53
KB081221-1-42	2.9	0.55	10	4.08	65.4	27.7	147	41.6	421	96	10490	2.37
KB081221-1-43	1.94	0.63	14.1	5.6	86.7	38.2	200	55.7	550	123.3	10030	3.3
KB081221-1-44	0.83	0.252	7.23	2.98	46.4	19.3	103.1	28	287	62.4	11180	2.6
KB081221-1-45	1.71	0.74	12.9	4.93	73.5	30.1	162	44.8	452	104.2	8570	2.29
KB081221-1-46	1.61	0.701	12.8	4.81	72.1	30.1	159	42.1	438	99.5	8570	1.33
KB081221-1-48	3.67	0.91	29.7	11.8	176	72	358	91	860	183	10320	4.82
KB081221-1-49	1.18	0.35	10.6	4.63	69	29.3	159.2	44.8	449	98.8	9620	2.27
KB081221-1-50	0.76	0.268	7.19	3.32	56.2	24.5	132	37.1	382	83.6	10450	3.38
KB081221-1-51	1.38	0.562	12.83	4.98	75.9	32.6	176.7	46.7	479	110.6	8930	1.73
KB081221-1-52	1.47	0.516	11.4	4.49	65.9	28	145	40.6	401	92.3	8770	1.34
KB081221-1-53	2.31	0.509	13.2	5.41	82.6	33.8	169.5	46.5	462	98.8	11050	2.77
KB081221-1-54	1.62	0.49	15.1	7.07	112	48.9	258	73	699	151.9	10390	7.33
KB081221-1-55	10	1.51	20.2	5.87	76.9	30.8	154	42.2	419	94.3	10030	2.46
KB081221-1-57	1.48	0.431	11.73	5.4	84.1	37.1	197.2	56.9	574	126.8	10310	5.51
KB081221-1-58	1.98	0.529	13.3	5.56	88.1	39.9	215	60.5	617	139.1	10770	5.73
KB081221-1-59	0.61	0.21	6.55	3.15	49.8	22.3	119.5	32.1	337	75.7	10690	2.26
KB081221-1-60	2.91	1.06	19.1	7.87	123.3	53.8	277	74	733	158	9770	6.09

Table 6d: Zircon trace element geochemical data for 53 zircon from the lower grey lithic tuff in Agnew Meadows.

Sample	U (ppm)	Th (ppm)	Si (ppm)	P (ppm)	Ti (ppm)	Y (ppm)	Nb (ppm)	La (ppm)	Ce (ppm)	Pr (ppm)	Nd (ppm)
KB081521-1-1	295	106.6	1.85E+05	70.9	83	518	1.06	0.015	5.28	0.068	0.8
KB081521-1-2	589	156.9	1.55E+05	2410	44	828	3.61	16.3	73	13	45
KB081521-1-3	816	359	1.49E+05	191	5.34	1134	4.45	2.34	28.9	1.84	6.8
KB081521-1-4	552	142.6	1.57E+05	860	13.6	802	4.21	6.9	34.9	5	16.1
KB081521-1-5	542	142.5	1.50E+05	4020	3.2	838	1.88	56	205	34.1	107
KB081521-1-6	2440	1210	1.50E+05	146	9	1400	9.2	1.13	32.3	1.14	3.9
KB081521-1-7	403	145.8	1.51E+05	64.3	5.4	722	1.54	0.011	7.45	0.089	0.84
KB081521-1-8	332	134.5	1.47E+05	74.5	2.45	791	0.934	0.0075	5.26	0.121	1.54
KB081521-1-9	1700	611	1.48E+05	262	1.6	1720	8.56	1.32	25.6	0.78	3.1
KB081521-1-10	851	206.5	1.52E+05	133.7	7.2	955	3.66	0.018	9.08	0.036	0.39
KB081521-1-11	190.5	52.8	1.52E+05	132	4.1	341	0.86	1.55	8.7	0.7	2.3
KB081521-1-12	262	75.9	1.49E+05	78.3	2.09	503	0.686	0.0047	3.93	0.049	0.57
KB081521-1-13	999	239.9	1.54E+05	130.9	1.44	1122	4.89	0.0015	10.9	0.005	0.302
KB081521-1-14	887	285	1.47E+05	613	1.43	1154	3.24	5.06	28.6	3.54	11.5
KB081521-1-15	1149	301.6	1.47E+05	73.5	1.92	1286	10.7	0.0044	18.65	0.03	0.4
KB081521-1-16	569	185	1.50E+05	115.5	1.45	925	1.9	0.0063	9.14	0.039	0.66
KB081521-1-17	958	270.5	1.47E+05	98.5	1.73	1118	6.01	0.048	13.93	0.051	0.64
KB081521-1-18	1272	411	1.48E+05	284	1.18	1245	4.98	2.03	21	1.21	4.5
KB081521-1-19	689	250	1.51E+05	74.5	1.82	1027	4.02	0.281	17.85	0.293	1.61
KB081521-1-20	1409	571	1.50E+05	620	5.04	1455	8.21	2.15	32.3	1.69	6.82
KB081521-1-21	1290	486.2	1.47E+05	840	1.86	1116	6.1	8.66	50.6	6.03	21
KB081521-1-22	721	189.5	1.49E+05	106.4	1.66	937	3.63	0.021	9.72	0.044	0.51
KB081521-1-23	722	318	1.50E+05	265	3.32	1254	4.3	4.5	34.5	2.5	8.4
KB081521-1-24	1033	302.5	1.50E+05	145.9	1.69	1120	4.95	0.063	12.31	0.081	0.52
KB081521-1-25	509	180	1.47E+05	98.5	3.33	781	2.46	0.0091	12.5	0.04	0.45
KB081521-1-26	1049	409	1.50E+05	67.9	1.42	1074	4.07	0.014	16.78	0.05	0.5
KB081521-1-27	1139	423	1.44E+05	162	2.38	1329	4.15	0.26	17.4	0.457	3.7
KB081521-1-28	1295	477	1.52E+05	82.1	1.58	1662	7.75	0.0029	20.04	0.061	0.99
KB081521-1-29	1301	400.1	1.51E+05	80.5	1.92	1578	11.71	0.0047	24.38	0.046	0.63
KB081521-1-31	775	259	1.48E+05	72	2.04	1088	6.3	0.015	18	0.022	0.46

Table 7a: Zircon trace element geochemical data for 53 zircon from the coarse-grained tuff in Red and White Spur.

Sample	Sm (ppm)	Eu (ppm)	Gd (ppm)	Tb (ppm)	Dy (ppm)	Ho (ppm)	Er (ppm)	Tm (ppm)	Yb (ppm)	Lu (ppm)	Hf (ppm)	Ta (ppm)
KB081521-1-1	1.21	0.54	8.6	2.73	39.2	16.6	82.1	22.7	226	51.6	9630	1.03
KB081521-1-2	8.7	1.12	16.9	4.82	66.4	26.6	137.1	38	364	78.9	11470	4.24
KB081521-1-3	3.36	0.76	17.8	6.74	100.4	41.1	209	56.3	551	120.8	10580	4.5
KB081521-1-4	4.2	0.59	11.2	3.82	56.7	23	131.1	36.5	367	84.1	11430	4.28
KB081521-1-5	17.6	1.75	26.6	5.7	66.3	26.6	133.1	36.1	354	79.6	10360	1.77
KB081521-1-6	2.75	0.72	22.4	8.8	129	53.1	265	69.9	667	143	11380	10.8
KB081521-1-7	1.28	0.52	9.29	3.76	55.5	23.1	122.5	32.7	326	74.8	9370	2
KB081521-1-8	2.2	0.7	13.1	4.94	68.5	26	128.8	33.3	306	69.9	9070	0.93
KB081521-1-9	2.52	0.5	20.3	9.18	148	62.5	333	91.1	858	190	10450	7.58
KB081521-1-10	0.91	0.229	9.75	3.96	67.8	30.3	157.8	46	456	102	11210	3.85
KB081521-1-11	0.88	0.262	3.91	1.57	24	10.35	56	15.76	162.7	37	10310	1.08
KB081521-1-12	1.04	0.334	6.96	2.63	38.5	16.1	83.4	23.6	238	57.1	8570	0.9
KB081521-1-13	1.05	0.329	9.6	4.78	76	34.4	184.8	52.3	536	119.8	11510	4.89
KB081521-1-14	3.58	0.61	16.7	6.41	94.1	39.3	203	54.2	509	111.6	10820	3.4
KB081521-1-15	1.37	0.368	13.83	6.28	101.7	47.5	263.3	71.6	746	169.7	11120	9.17
KB081521-1-16	1.07	0.397	10.5	4.2	67.5	29.3	152.3	42.7	439	98.3	9580	2.06
KB081521-1-17	1.49	0.325	14.1	5.88	94.3	41.5	214.8	59.6	604	134.2	10950	6.36
KB081521-1-18	2.9	0.36	14.6	6.72	102.9	44.9	237	66.2	644	145.4	10900	5
KB081521-1-19	1.3	0.51	12.04	4.92	75.3	32.2	169.8	49.5	479	107	10300	3.92
KB081521-1-20	3.09	0.72	19.7	8.75	134.9	55.7	288	75.6	730	156.3	10830	7.52
KB081521-1-21	5.17	0.624	17.26	6.46	91.4	37.3	198.3	51.6	487	105.8	11100	7.46
KB081521-1-22	1.16	0.31	9.4	4.18	68.6	29.7	153	44.5	429	95.9	10880	4.01
KB081521-1-23	3.36	0.92	18.1	7.2	113.1	47.3	238.7	63.3	620	132.9	9540	3.36
KB081521-1-24	1.41	0.271	11.18	5.25	88.8	38.6	208.4	56.8	582	130.9	10990	5.16
KB081521-1-25	1.08	0.317	8.8	3.73	56.7	24.5	131	37.4	377	83	9290	2.62
KB081521-1-26	1.13	0.433	12.6	4.85	82.3	34.23	182.7	48.6	487	107.8	10850	4.97
KB081521-1-27	5.68	3.1	34.5	11.39	142.2	47.6	229	56.2	557	118.6	10630	3.98
KB081521-1-28	2.73	0.68	21.4	9.99	148.3	63	315	85.3	821	173.4	11450	7.1
KB081521-1-29	1.69	0.401	16.11	7.61	126.7	55.4	297.3	85.8	825	179.3	11140	9.89
KB081521-1-31	1.26	0.412	12	5.36	84.7	36.3	196	55.9	546	120.3	10030	5.78

Table 7b: Zircon trace element geochemical data for 53 zircon from the coarse-grained tuff in Red and White Spur.

Sample	U (ppm)	Th (ppm)	Si (ppm)	P (ppm)	Ti (ppm)	Y (ppm)	Nb (ppm)	La (ppm)	Ce (ppm)	Pr (ppm)	Nd (ppm)
KB081521-1-32	574	124.1	1.48E+05	276	1.72	656	3.89	0.134	9.64	0.179	1.27
KB081521-1-33	1108	317	1.53E+05	341	53.3	1304	9.78	4.44	33.63	2.67	8.07
KB081521-1-34	658	301	1.44E+05	76.3	3.98	1161	1.82	0.027	9.06	0.219	2.23
KB081521-1-35	840	219	1.46E+05	147	1.27	984	3.69	0.3	10.5	0.2	1.02
KB081521-1-36	1147	305.9	1.49E+05	94.4	1.58	1244	9.47	0.022	17.36	0.048	0.55
KB081521-1-37	1025	353	1.49E+05	400	1.96	1311	8.39	5.6	40.5	3.6	13.7
KB081521-1-38	909	261	1.45E+05	300	1.88	1126	6.54	2.59	25.6	1.72	6.3
KB081521-1-39	569	241	1.47E+05	72.6	3.13	831	2	0.015	11.75	0.066	0.49
KB081521-1-40	1520	506	1.50E+05	91.9	1.85	1701	9.21	0.0061	24.1	0.05	0.68
KB081521-1-41	490	130.1	1.50E+05	580	2.44	531	1.42	3.6	26.1	3.1	10.8
KB081521-1-42	1710	660	1.48E+05	203	1.68	1640	6.7	0.056	20.2	0.11	0.95
KB081521-1-43	1104	501	1.45E+05	115.4	1.55	1265	5.17	0.0074	25.5	0.052	0.76
KB081521-1-44	1380	488	1.45E+05	233	1.91	1500	5.3	0.7	19.6	0.47	2
KB081521-1-45	577	189	1.54E+05	79.8	1.07	939	2.92	0.017	12.71	0.046	0.5
KB081521-1-46	623	297	1.52E+05	57.7	1.62	826	2.71	0.0045	18.5	0.061	0.5
KB081521-1-47	215.8	62.6	1.47E+05	71.1	2.97	439	0.62	0.0044	3.32	0.024	0.54
KB081521-1-48	1055	292.6	1.48E+05	91.1	2.16	1335	11.84	0.079	20.15	0.065	0.54
KB081521-1-49	1391	560	1.47E+05	103.9	2.39	1822	12.77	0.0028	36.1	0.052	1.03
KB081521-1-50	817	324	1.50E+05	115	1.2	1230	2	0.39	13.88	0.35	2.44
KB081521-1-51	1210	390	1.46E+05	155	1.03	1310	5	0.0014	13.9	0.045	0.32
KB081521-1-52	821	326	1.46E+05	110	1.67	1350	1.54	0.015	10.24	0.184	2.61
KB081521-1-53	420	113	1.47E+05	99.8	2.12	680	1.68	0.0096	5.6	0.018	0.48
KB081521-1-54	227	71.9	1.44E+05	85	3.06	503	0.748	0.0014	3.98	0.035	0.52

Table 7c: Zircon trace element geochemical data for 53 zircon from the coarse-grained tuff in Red and White Spur.

Sample	Sm (ppm)	Eu (ppm)	Gd (ppm)	Tb (ppm)	Dy (ppm)	Ho (ppm)	Er (ppm)	Tm (ppm)	Yb (ppm)	Lu (ppm)	Hf (ppm)	Ta (ppm)
KB081521-1-32	0.87	0.279	7.22	3.06	48.1	21.5	112.1	32.1	334	75.2	11310	4.46
KB081521-1-33	2.72	0.512	14.74	6.77	106.1	47.4	256	73.7	738	166.1	11080	8.99
KB081521-1-34	2.88	1.27	19.8	8.01	112.2	43.7	217.4	58.4	548	118	8320	1.71
KB081521-1-35	0.91	0.219	9.2	4.5	70.1	30.7	165	45.7	463	99.9	10940	4
KB081521-1-36	1.26	0.323	12.49	6.1	99.1	45	246.1	70.9	697	152	10820	8.63
KB081521-1-37	3.84	0.68	16.7	6.73	104.7	47.1	239	66.6	671	140.3	10960	7.36
KB081521-1-38	2.33	0.47	13.78	5.48	87.5	38.7	206.4	57.2	597	130.9	10770	6.44
KB081521-1-39	1.33	0.61	9.12	3.65	60.5	26.3	140	38.6	383	88.7	9350	2.16
KB081521-1-40	2.19	0.558	19.8	9.38	147.9	63.3	321	86.2	846	183.1	11040	9.75
KB081521-1-41	2.12	0.54	7.14	2.44	36	15.74	89.3	26.1	279	66.9	10880	2.02
KB081521-1-42	1.88	0.63	19.5	9.1	143	63.1	320	87	860	183	10430	6.5
KB081521-1-43	1.96	0.71	17.5	7.3	107	46.7	235.2	64.9	614	135	9510	4.53
KB081521-1-44	2.11	0.58	15.1	7.3	120	50.7	272	75.7	753	161	10080	5.32
KB081521-1-45	0.91	0.357	10.8	4.36	69.1	28.2	145.5	41	407	88.7	10670	3.4
KB081521-1-46	1.36	0.477	10.6	4.23	62.9	26	138.7	37.7	375	85	10450	3.42
KB081521-1-47	0.9	0.401	5.67	2.39	32.4	13.71	69.7	19.25	198	47.7	8700	0.75
KB081521-1-48	1.33	0.376	13.5	6.86	112.4	49	270	74	777	170.4	10730	11.02
KB081521-1-49	2.71	0.6	24.1	10.58	161.1	69.8	351	92.8	889	191.4	10500	10.88
KB081521-1-50	3.43	1.05	22.4	8.36	118.8	46.2	234	60.9	577	125.4	10110	2.15
KB081521-1-51	1.41	0.383	14.4	6.5	104	45	234	66	640	138	10630	5.2
KB081521-1-52	4.8	0.98	28.8	10.4	138	53	250	63.5	593	125	10710	1.86
KB081521-1-53	0.94	0.348	7.14	3.1	48.1	21.4	113.4	31.7	324	75	9840	1.79
KB081521-1-54	0.88	0.401	6.56	2.69	38.6	16.7	85.9	24.3	243	56.5	8470	0.81

Table 7d: Zircon trace element geochemical data for 53 zircon from the coarse-grained tuff in Red and White Spur.

APPENDIX C

Sample	Unit	SiO2	TiO2	Al2O3	Fe2O3	MnO	MgO	CaO	Na2O	K2O	P2O5
KB080321-1	upper grey lithic tuff	73.56	0.35	13.75	3.86	0.07	1.01	1.10	2.20	4.05	0.04
KB080521-1	lower grey lithic tuff	74.03	0.18	14.14	1.74	0.08	0.58	2.64	0.22	6.34	0.05
KB080521-2A	pumice conglomerate matrix	70.18	0.19	15.75	2.63	0.13	1.57	2.76	1.30	5.43	0.05
KB080621-1	tuff of Skelton Lake	75.35	0.18	13.75	1.75	0.05	0.29	1.10	2.75	4.73	0.04
KB080621-2	Clast in tuff of Skelton Lake	63.41	0.22	19.10	4.38	0.14	0.73	2.60	3.83	5.53	0.06
KB080721-1B	clast in lower grey lithic tuff	64.34	0.20	17.92	4.33	0.30	2.74	6.98	0.55	2.58	0.05
KB080821-2	tuff SE of pumice conglomerate	72.04	0.17	14.85	2.31	0.13	1.17	2.49	3.21	3.57	0.05
KB080921-2	pumice conglomerate clast	78.22	0.16	13.30	0.76	0.02	0.18	0.30	1.46	5.54	0.06
KB080921-3	upper grey lithic tuff	74.04	0.23	15.71	1.55	0.03	0.54	0.44	3.09	4.32	0.05
KB081021-1	tuff of San Joaquin Mountain	72.08	0.22	14.93	2.30	0.15	0.66	1.73	3.61	4.23	0.07
KB081021-2	"lithic tuff"	72.94	0.26	15.10	2.40	0.09	0.86	0.89	3.94	3.45	0.07
KB081221-2	lithic tuff NW of pumice conglomerate	73.45	0.29	13.90	2.83	0.13	1.59	2.37	0.66	4.70	0.08
KB081521-1	Red and White coarse tuff	73.33	0.29	13.92	2.70	0.08	0.58	2.73	1.96	4.34	0.08
KB081521-2	Red and White fine tuff	74.77	0.20	13.13	2.22	0.09	0.63	3.49	2.36	3.05	0.06
KB081521-3	Red and White fine tuff	77.00	0.20	12.79	1.40	0.05	0.54	4.04	0.33	3.58	0.06

Table 8: Whole-rock geochemical data for rocks from Agnew Meadows area, Skelton Lake area, and the Red and White Spur area.